

Modulation spectroscopy of semiconductors: bulk/thin film, microstructures, surfaces/interfaces and devices

Fred H. Pollak

Department of Physics, Brooklyn College of the City University of New York, Brooklyn, NY 11210 (USA)

H. Shen

US Army Research Laboratory, Electronic and Power Sources Directorate, AMSRL-EP-EF, Fort Monmouth, NJ 07703-5601 (USA)

(Received February 15, 1993; accepted April 12, 1993)

Contents

1. Introduction	275
2. Modulation techniques	278
2.1. External modulation	279
2.2. Internal modulation	282
2.2.1. Differential reflectivity	282
2.2.2. Reflection difference spectroscopy	282
3. Lineshape considerations	283
3.1. Electromodulation	283
3.1.1. Third derivative spectroscopy (low-field regime)	284
3.1.2. Franz-Keldysh oscillations (intermediate field regime)	285
3.1.3. First-derivative spectroscopy	288
3.2. Thermo- and piezomodulation	290
3.3. Differential reflectivity	290
3.4. Interference effects	290
4. Bulk properties	291
4.1. Space charge region	291
4.2. Carrier concentration	295
4.3. Nature of band bending (carrier type)	296
4.4. Impurity effects	297
4.5. Deep levels	299
4.6. Alloy composition	300
4.7. External perturbations	301
4.7.1. Temperature	301
4.7.1.1. Temperature dependence of band gaps	302
4.7.1.2. Temperature dependence of the linewidth	304
4.7.2. Uniaxial stress	305
4.8. Process/growth-induced effects and annealing	305
4.9. Amorphous and microcrystalline semiconductors	310

Modulation spectroscopy of semiconductors: bulk/thin film, microstructures, surfaces/interfaces and devices

Fred H. Pollak

Department of Physics, Brooklyn College of the City University of New York, Brooklyn, NY 11210 (USA)

H. Shen*

US Army Research Laboratory, Electronic and Power Sources Directorate, AMSRL-EP-EF, Fort Monmouth, NJ 07703-5601 (USA)

(Received February 15, 1993; accepted April 12, 1993)

Abstract

Modulation spectroscopy is a powerful method for the study and characterization of a large number of semiconductor configurations, including bulk/thin film, microstructures (heterojunctions, quantum wells, superlattices, quantum dots), surfaces/interfaces and actual device structures in addition to semiconductor growth/processing. Furthermore, the influence of external perturbations such as temperature, electric fields, hydrostatic pressure, uniaxial stress, etc. can be investigated. This optical technique utilizes a very general principle of experimental physics, in which a periodically applied perturbation (either to the sample or probe) leads to sharp, derivative-like spectral features in the optical response of the system. Because of the richness of the derivative-like spectra, the information in the lineshape fits, room temperature performance and relative simplicity of operation this method is becoming increasingly more important as a tool to study these materials and structures. This article will review developments in the field during the last decade.

1. Introduction

Since its inception in 1964, modulation spectroscopy has proven to be a powerful experimental technique for studying and characterizing the properties of bulk semiconductors, reduced dimensional systems (surfaces, interfaces, heterostructures, etc.), actual device structures and growth/processing. Modulation spectroscopy deals with the measurement and interpretation of changes in the optical response of a sample which are caused by modifying in some way the measurement conditions. This can easily be accomplished by periodically modulating (a) some parameter applied to the sample ("external" modulation) or (b) the measurement conditions themselves ("internal" modulation). The observed normalized changes are usually small so that the difference signals are closely related to a derivative of the absolute spectrum with respect to the modifying parameter. The derivative nature of modulation spectroscopy emphasizes structure localized in the photon energy region of interband (intersubband) transitions of semiconductors (semiconductor microstructures) and suppresses uninteresting background effects. Also, weak features that may not have been detected in the absolute spectra are often enhanced. Because of this derivative-like nature a large number of sharp spectral features can be observed, even at room temperature.

As an example of the power of modulation spectroscopy, Fig. 1 shows a comparison of the reflectivity (R) and electric-field modulated (electroreflectance: ER) spectra of bulk

*Also at GEO Center, Inc., Lake Hopatcong, NJ 07849, USA.

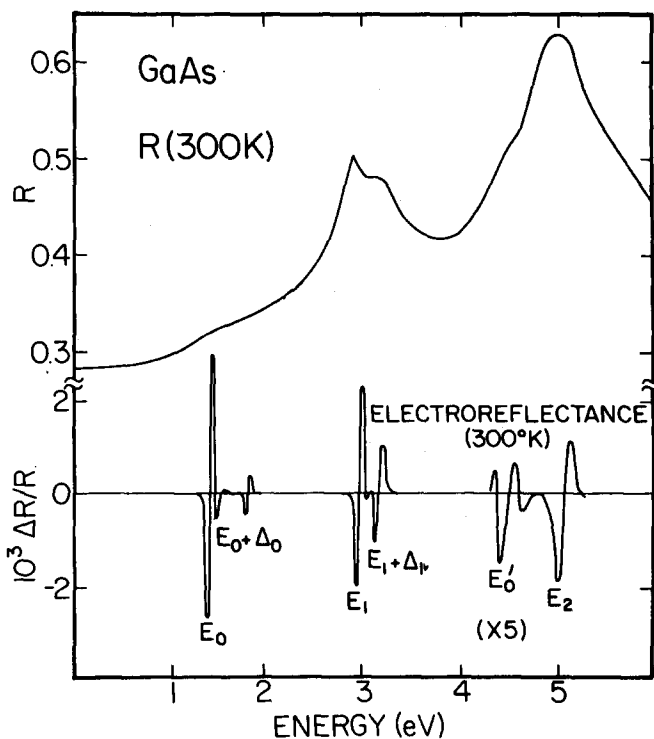


Fig. 1. Comparison of room temperature reflectivity and electric field-modulated reflectivity (electroreflectance) of GaAs [1].

GaAs at 300 K [1]. While the reflectivity is characterized by broad features, the ER trace has zero as a base and is dominated by a series of very sharp, derivative-like features, corresponding to specific transitions in the Brillouin zone (BZ).

The ability to perform a lineshape fit is one of the great advantages of modulation spectroscopy. Since, for the modulated signal, the features are localized in photon energy it is possible to account for the lineshapes to yield accurate values of energies and broadening parameters of interband transitions. For example, it is possible to determine the energies of the E_0 , $E_0 + \Delta_0$, E_1 and $E_1 + \Delta_1$ peaks in Fig. 1 to within a few meV, even at room temperature. Thus, the effects of static external perturbations such as electric and magnetic fields, temperature, hydrostatic pressure, uniaxial stress, composition etc. can be conveniently studied.

In addition to the utility of the sharp, derivative-like peaks of Fig. 1 there is also important information in other modulation variables, such as phase, modulation frequency, modulation amplitude etc. Certain types of modulation spectroscopy can be spatially (depth) selective and thus act as probes of specific regions of the sample being studied. Also, the ability to change the perturbation in a specific manner can be used to investigate the effects of that perturbation on the sample.

The results of work in this first decade have been reviewed by Cardona [2,3], Hamakawa and Nishino [4], Aspnes [5] and Pollak [1]. The interested reader is also referred to Vol. 9 of *Semiconductors and Semimetals*, eds. R.L. Willardson and A.C. Beer (Academic, New York, 1972) and to the Proceedings of the First International Conference on Modulation Spectroscopy, published as Vol. 37 of *Surface Science* (1973).

In the 1980s, modulation spectroscopy enjoyed a renaissance. It was shown that the same advantages long exploited for bulk studies were also evident in the artificial semiconductor microstructures fabricated by modern thin film methods, such as molecular beam epitaxy (MBE) or organometallic chemical vapour deposition (OMCVD) [6–10]. The work of Glembotck *et al.* [9,10] is particularly significant since it demonstrated that a large number of intersubband transitions in a multiple quantum well could be observed at room temperature using the contactless electromodulation (EM) method of photoreflectance (PR).

Figure 2 shows the PR spectra at 300 K from a thick GaAlAs epitaxial layer on GaAs and a series of GaAs/GaAlAs multiple quantum wells (MQWs) with different well widths (L_z) in the vicinity of the E_0 transition [9,10]. Even at 300 K the spectra are extremely rich. The notation h_n and l_n represents “symmetry”-allowed transitions of index n between the quantized conduction and valence subbands of heavy (h) or light (l) hole character. In fact all the “symmetry”-allowed transitions were observed. The solid arrows are the energies of the various transitions deduced from a theoretical model. Thus, the rich modulated spectra from microstructures could be used to probe the “band structure”

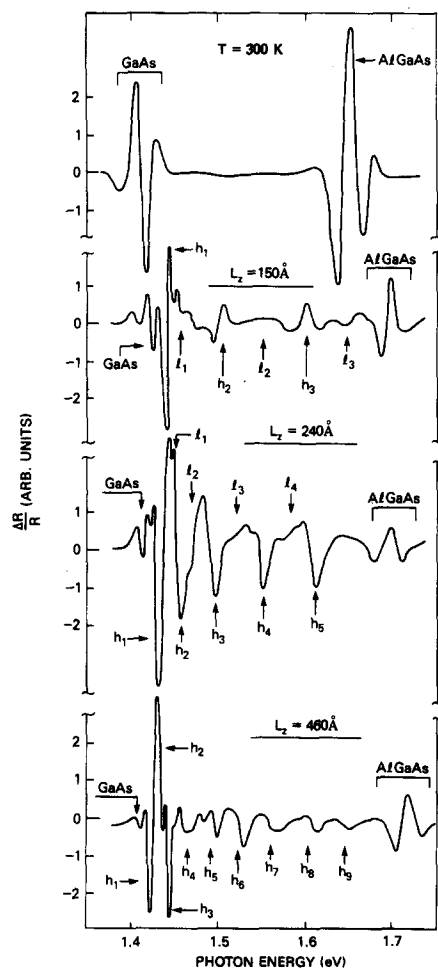


Fig. 2. Room temperature photoreflectance spectra for an undoped GaAs/Ga_{1-x}Al_xAs heterojunction (top trace) and three multiple quantum well samples with $x \approx 0.2$. The arrows labelled h_1, h_2, \dots, h_n (l_1, l_2, \dots, l_n) correspond to the calculated values of “symmetry-allowed” interband transitions between heavy (light) hole valence and conduction subbands [9,10].

of reduced dimensional systems, just as this optical method was employed for bulk material.

These advances have stimulated a considerable amount of activity in experimental and theoretical areas as well as the development of new instrumentation, particularly contactless modes. Not only is work being carried out on the fundamental aspects of a large variety of reduced dimensional systems, such as single quantum wells (SQWs), multiple quantum wells (MQWs), superlattices (SLs), heterojunctions (HJs) and surfaces/interfaces, but the properties of bulk material are being revisited. The effects of various external perturbations are also being explored. The advent of the diamond anvil cell makes it possible to generate extremely high pressures.

Certain contactless methods allow measurements to be made *in situ*, including elevated temperatures (≈ 600 °C). Thus these techniques are extremely useful for the *in situ* monitoring of growth/processing. Another significant development is the use of EM methods to characterize actual device structures, such as GaAs/GaAlAs and InP/InGaAs heterojunction bipolar transistors and pseudomorphic GaAlAs/InGaAs/GaAs high electron mobility transistors.

The optical properties related to the electronic states of semiconductors and semiconductor microstructures can also be studied and characterized by other spectroscopic methods, such as photoluminescence (PL), photoluminescence excitation spectroscopy (PLE), absorption spectroscopy, photocurrent spectroscopy, spectral ellipsometry, resonant Raman scattering etc. Modulation spectroscopy, particularly contactless EM modes, is becoming increasingly more important as an experimental method. This is because of the richness of the spectra (even at 300 K and above), the information in the lineshape fits (including phase), the sensitivity of EM to surface/interface electric fields, the relative simplicity, compactness and ease of operation of the instrumentation, etc. Other aspects of modulation spectroscopy will be discussed in the following section.

This article will review developments in modulation spectroscopy during the past decade. With some exceptions we shall not repeat the material covered in the previously mentioned articles concerning the pre-1980s phase of this field. Section 2 discusses a number of modulation techniques with an emphasis on contactless approaches. Lineshape considerations for various modulation methods, particularly EM, is the subject of Section 3. New applications to the study of bulk properties, including the influence of external perturbations, are the topic of Section 4. Sections 5, 6 and 7 deal with surfaces/interfaces, electrochemistry and epitaxial layers, respectively. The application of modulation spectroscopy to the study of semiconductor microstructures including compositional QWs and SLs (III-V, II-VI and GeSi materials), doping SLs, two-dimensional electron gas (2DEG) and external perturbations is discussed in Section 8. In Section 9, work on the characterization of actual device structures is reviewed. Section 10 is devoted to the development of modulation spectroscopy for *in situ* monitoring/control of growth/processing. Some speculations about future trends are mentioned in Section 11.

2. Modulation techniques

The spectral response of a material can be modified directly by applying a repetitive perturbation, such as electric field (electromodulation), heat pulse (thermomodulation), or stress (piezomodulation). This procedure is termed "external" modulation [5]. In addition, "external" modulation is an a.c. method which represents the optical response of the system

to the modulating parameter. Thus, there is also important information in other modulating variables, such as phase, modulation frequency, modulation amplitude, pump wavelength etc. For example, EM can be employed as an optical impedance spectroscopy technique to gain information about trap studies or the equivalent circuit of the structure.

The change may also occur in the measuring system itself, e.g. the wavelength or polarization conditions can be modulated or the sample reflectance (transmittance) can be compared to a reference sample. This mode has been labelled "internal" modulation [5].

2.1. External modulation

Figure 3 is a schematic drawing of the experimental arrangement for a general "external" modulated reflectance experiment (with the exception of photoreflectance or electron beam electroreflectance) [5,11]. Light from an appropriate light source (xenon arc, halogen or tungsten lamp) passes through a monochromator (probe monochromator). The exit intensity at wavelength λ , $I_0(\lambda)$, is focused on the sample by means of a lens (or mirror). The modulation (electric field, stress, temperature) is applied to the sample at frequency Ω_m . The reflected light is collected by a second lens (mirror) and is focused on an appropriate detector (photomultiplier, photodiode etc.). For the sake of simplicity, the two lenses (mirrors) are not shown. For modulated transmission the detector is placed behind the sample. In general, however, reflectance is more useful.

The light striking the detector contains two signals: the d.c. (or average value) is given by $I_0(\lambda)R(\lambda)$, where $R(\lambda)$ is the d.c. reflectance of the material, while the modulated value (at frequency Ω_m) is $I_0(\lambda)\Delta R(\lambda)$, where $\Delta R(\lambda)$ is the change in reflectance produced by the modulation source. The a.c. signal from the detector, proportional to $I_0\Delta R$, is measured by a lock-in amplifier (or other signal averaging procedure). Typically $I_0\Delta R$ is 10^{-4} – 10^{-6} of I_0R .

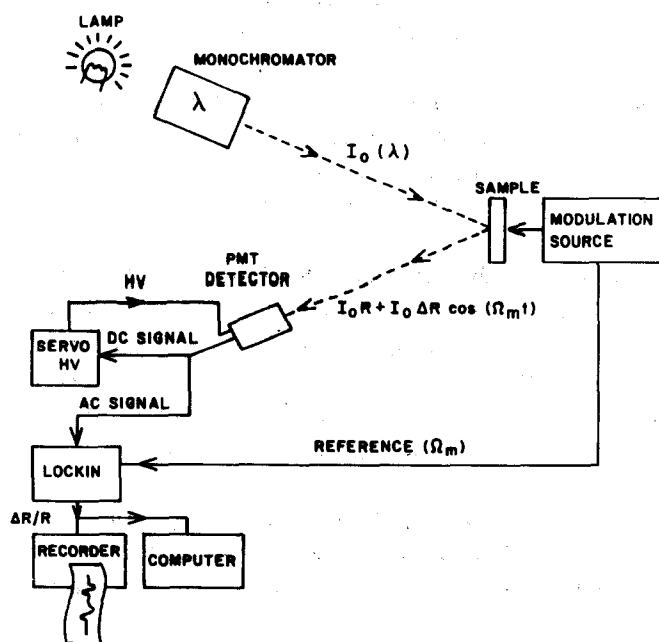


Fig. 3. Schematic representation of an "external modulation" experimental apparatus (except photoreflectance and electron beam electroreflectance) [5,11].

In order to evaluate the quantity of interest, i.e. the relative change in reflectance $\Delta R/R$, a normalization procedure must be used to eliminate the uninteresting common feature $I_0(\lambda)$. This can be done in several ways, one of which is shown in Fig. 3 for the case of a photomultiplier (PMT) detector. The d.c. output from the PMT is applied to a servo power supply which adjusts the high voltage on the PMT in order to keep $I_0 \Delta R$ as a constant. Under these conditions the output of the lock-in amplifier, which goes to a recorder or computer, is directly proportional to the quantity of interest, $\Delta R/R$. Normalization also can be performed by dividing ΔR by R in an analog manner.

It should be pointed out that since modulation spectroscopy is a normalized optical method not every photon need be collected. For example, if there is some obstruction on a viewport or the morphology of the surface is not good, so that a fraction of the light is lost, then the light striking the sample is only αI_0 , where $\alpha < 1$. Thus the d.c. reflected component will be $\alpha I_0 R$ and the a.c. signal is $\alpha I_0 \Delta R$. However, the normalized signal is still proportional to $\Delta R/R$. Thus as long as there are enough photons to give a good signal-to-noise ratio, the lineshape of the modulated optical spectrum is not affected by the loss of some light.

Electromodulation can be accomplished in several ways, including contact and contactless modes. Four common contact configurations, designated as electroreflectance (ER), can be divided into "longitudinal" and "transverse" categories [5]. The "longitudinal" method can be applied in the semiconductor-electrolyte, metal-insulator-semiconductor (MIS), Schottky barrier or p-i-n configurations. In the latter, the sample of interest is placed in the insulating region of a p-i-n diode [12]. The former has in the past been the most widely used form of ER because of the ease of implementation, since the sample surface requires no special preparation. However, it can be used only over a limited temperature range (300 K to 150 K) and often offers less control over the space charge field, owing to chemical passivation or dissolution effects. Electrolyte electroreflectance (EER) can be employed for depth profiling measurements with the proper choice of electrolyte and electrochemical conditions. This method has also been employed for electrochemical studies. Schottky barrier, MIS and p-i-n methods can be used at low temperatures to reduce lifetime broadening. The p-i-n configuration produces a constant electric field as opposed to the position-dependent field of the other "longitudinal" modes. In the "transverse" mode, two metal electrodes are evaporated on the surface of the sample and EM is produced by applying a modulated high voltage across the gap (≈ 1 mm). However, this technique can only be used on materials with resistivities greater than 10^8 ohm cm [5].

In temperature modulation (thermoreflectance: TR), the sample may be mounted on a small heater attached to a heat sink and the temperature varied cyclically by passing current pulses through the heater. If the sample is properly conducting, the current can be passed through the sample directly. Alternatively, a secondary beam of light may be used to heat the sample. Generally, the modulation frequency (Ω_m) for this method must be kept below 10–20 Hz and hence there are often problems with the 1/f noise of the detector.

In piezoreflectance (PZR), modulation is achieved by mounting the sample on a piezoelectric transducer which varies the lattice constant of the material, producing a band gap modulation. Although PZR is contactless it requires special mounting of the sample, as does thermomodulation.

Contactless electromodulation can be performed using (a) PR [12–15], (b) a new approach which uses a capacitor-like arrangement [16–19] or (c) electron beam electro-

reflectance (EBER) [20]. The method of PR is not only contactless but requires no special mounting of the sample. It can be used in any transparent medium under a variety of conditions. It has been demonstrated that PR can be used at temperatures as high as 650 °C.

Figure 4 is the schematic representation of a PR apparatus [13,21]. Modulation of the electric field in the sample is caused by photo-excited electron-hole pairs created by the pump source (laser or other light source), which is chopped at frequency Ω_m . Most PR experiments have utilized a mechanical chopper with maximum $\Omega_m \approx 5$ kHz. To achieve higher modulation frequencies up to about 1 MHz, an acousto-optic modulator can be used [22]. The photon energy of the pump source should be above the band gap of the semiconductor being investigated. The pump creates photo-injected electron-hole pairs which modulate the built-in electric field of the semiconductor or semiconductor microstructure under investigation. A typical pump is a 5 mW He-Ne laser (except at high temperatures, where a more powerful beam must be used).

In Fig. 4 the normalization is performed by a variable neutral density filter (VNDF) connected to a servo mechanism. The d.c. signal from the detector, which is proportional to $I_0(\lambda)R(\lambda)$, is introduced into the servo, which moves the VNDF in such a manner as to keep $I_0(\lambda)R(\lambda)$ constant, i.e. $I_0(\lambda)R(\lambda) = C$. Under these conditions the a.c. signal $I_0(\lambda) \Delta R(\lambda) = C \Delta R(\lambda)/R(\lambda)$. Thus, the signal to the lock-in amplifier is proportional to the quantity of interest, i.e. $\Delta R(\lambda)/R(\lambda)$.

By changing the wavelength of the pump beam in PR it is possible to perform non-destructive depth profiling [22,23].

Photoreflectance also can be performed in an excitation mode (PRE). The probe monochromator is set to correspond to some relevant PR feature, and then the amplitude of the signal reaching the detector (i.e. $\Delta R/R$) is measured as a function of the wavelength of the normalized pump beam [24]. In PRE, the PR feature to be employed need not correspond to the ground state transition, in contrast to PLE.

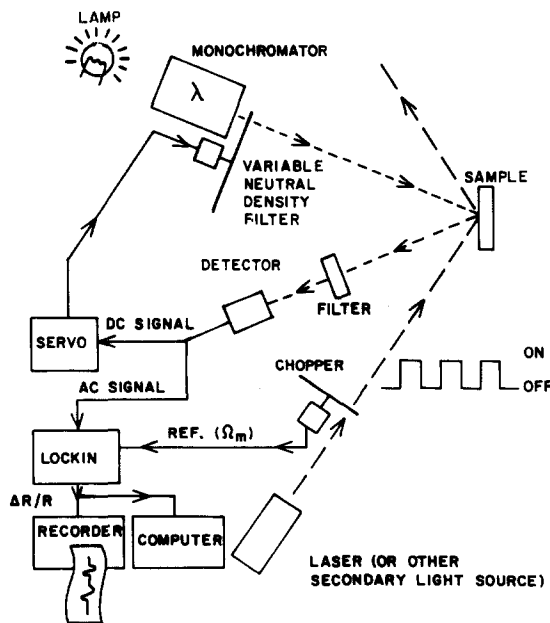


Fig. 4. Schematic representation of a photoreflectance apparatus [21].

The vast majority of PR experiments measure features due to interband (intersubband) transitions between valence and conduction bands (subbands) in semiconductors and semiconductor microstructures, i.e. probe monochromator wavelength in the near infrared to visible region. However, it is also possible to study the photo-induced transitions between quantized electron subbands in quantum wells by using an infrared probe beam and visible laser [25,26].

A drawback of PR is the spurious modulated background signal reaching the detector because of (a) luminescence from the sample and/or (b) scattered light from the pump source. Luminescence can sometimes be a problem for measurements near the fundamental gap, particularly at low temperatures. Scattered pump light can be reduced by means of an appropriate long pass filter in front of the detector. If the overall spurious background signal is not too large in relation to $\Delta R/R$, it can be subtracted by the normalization method of Fig. 2. The spurious background signal also can be reduced or eliminated by approaches such as the use of a double monochromator [27], tuneable dye laser probe beam [28], sweeping PR [29] or differential PR [23].

A contactless electroreflectance (CER) method has been reported which utilizes a condenser-like system consisting of a thin, transparent, conductive coating (indium-tin-oxide or 50–60 Å of a metal such as Au or Ni) on a transparent substrate (glass, quartz etc.) which serves as one electrode [16–19]. A second electrode, consisting of a metal strip, is separated from the first electrode by insulating spacers. The sample (≈ 0.5 mm thick) is placed between these two capacitor plates. The dimensions of the spacer are such that there is a very thin layer (≈ 0.1 mm) of air (or vacuum) between the front surface of the sample and the conducting part of the first electrode. Thus, there is nothing in direct contact with the front surface of the sample. The a.c. modulating (≈ 1 kV peak-to-peak) and d.c. bias voltages are applied between the metal strip and the transparent conductor. The probe beam is incident through the first transparent electrode. This approach can also be employed in the transmission mode by replacing the metal electrode with a second transparent electrode/substrate.

In EBER the pump beam is replaced by a modulated low-energy electron beam (≈ 200 eV) chopped at about 1 kHz [20]. However, the sample and electron gun must be placed in an ultra-high vacuum chamber.

Tober *et al.* [30] have reported the use of differential photoconductivity to characterize p-i-n and Schottky diode structures. The spectra were obtained in such a way as to produce a first derivative with respect to either photon energy or an electric field.

2.2. Internal modulation

2.2.1. Differential reflectivity

A commonly used form of "internal" modulation is differential reflectometry, in which the reflectance of the sample (or portion of the sample) under investigation is compared to a standard material. This can be accomplished either by holding the sample stationary and scanning the probe beam between the two regions [31–33] or by holding the light spot fixed and moving the sample [34–37]. The former will be designated DR₁ while the latter will be referred to as DR₂.

2.2.2. Reflection difference spectroscopy

An extremely useful form of "internal" modulation is reflectance difference spectroscopy (RDS or RD) or, as it sometimes is called, reflectance anisotropy (RA) [38–40]. The

technique of RDS (RA) is a normal incidence optical probe that uses symmetry to enhance the typically low sensitivity of reflectance measurements to surface phenomena. In RDS (RA) the difference between the normal incidence reflectance R of light polarized parallel and perpendicular to a principal crystallographic axis in the plane of the crystal is measured. Because of the cubic symmetry of zincblende-type semiconductors, the bulk is nearly isotropic, while regions of lower symmetry, such as those creased by electric fields, can be anisotropic.

This method also has been employed extensively for the *in situ* characterization of epitaxial growth by MBE or OMVCD on (001) zincblende surfaces. Important chemical and structural information has been obtained, including real-time monitoring. However, such investigations are beyond the scope of this article and the interested reader is referred to refs. 41–45.

3. Lineshape considerations

Differential changes in the reflectivity can be related to the perturbation of the complex dielectric function $\epsilon (= \epsilon_1 + i\epsilon_2)$ expressed as [2,3,5]:

$$\Delta R/R = a(\epsilon_1, \epsilon_2) \Delta\epsilon_1 + b[(\epsilon_1, \epsilon_2) \Delta\epsilon_2] \quad (1)$$

where a and b are the Seraphin coefficients, related to the unperturbed dielectric function, and $\Delta\epsilon_1$ and $\Delta\epsilon_2$ are the changes in the complex dielectric function due to the perturbation. The quantities $\Delta\epsilon_1$ and $\Delta\epsilon_2$ are related by a Kramers-Kronig inversion. Near the fundamental gap of bulk materials $b \approx 0$ [5] so that $\Delta R/R \approx a \Delta\epsilon_1$, is the only term that is important. However, in multilayer structures interference effects are important so that both $\Delta\epsilon_1$ and $\Delta\epsilon_2$ may have to be considered. The functional form of $\Delta\epsilon_1$ and $\Delta\epsilon_2$ can be calculated for a given perturbation provided that the dielectric function and critical point are known.

3.1. Electromodulation

Electromodulation is the most complex form of modulation spectroscopy. This perturbation can destroy the translational symmetry of the material and hence can accelerate unbound electrons and/or holes [4,5,11,13–15]. As will be discussed below, this is exactly the aspect of EM that produces a sharp, third derivative lineshape under certain electric field conditions.

However, for bound states such as excitons, impurities, quantum wells or the uncoupled states of multiple quantum wells, the perturbing field does not accelerate electrons and/or holes. These types of particle do not have translational symmetry and are confined in space. Their energy spectrum is discrete and not continuous as in the case of the unbound particles. In this situation the modulating field can alter the binding energy of the particle (Stark effect). In addition, the field can vary the intensity of the transition through a physical separation of the electrons and holes or it can change the lifetime of the state in the case of a finite binding potential. In the case of bound states the lineshape is first-derivative [13,14].

Electromodulation can be classified into three categories, i.e. low-, intermediate- and high-field regimes depending on the relative strengths of certain characteristic energies [4,5]. In the first range $|\hbar\theta| \leq \Gamma$, where Γ is the broadening parameter and $\hbar\theta$ is the electro-

optic energy, given by:

$$(\hbar\theta)^3 = q^2\hbar^2 F^2 / 2\mu_{\parallel} \quad (2)$$

In eqn. (2), F is the field and μ_{\parallel} is the reduced interband mass in the direction of the field. In the intermediate-field case $|\hbar\theta| \gtrsim \Gamma$, but $qFa_0 \ll E_g$, where a_0 is the lattice constant (or an appropriate periodic length in microstructures) and E_g is the band gap. In this situation the band structure is unchanged. In the high-field regime the electro-optic energy is again much greater than the broadening, but $eFa_0 \approx E_g$ so that Stark shifts are produced.

3.1.1. Third derivative spectroscopy (low-field regime)

For the unbound situation, the case of low field modulation ($|\hbar\theta| \ll \Gamma$) from flatband will be considered, i.e. no built-in d.c. field [5,13,14]. It can be shown that in this case:

$$\Delta\epsilon = [(\hbar\theta)^3/E^2][\partial^3/\partial E^3]E^2\epsilon(E - E_g, \Gamma) \quad (3)$$

If the form of ϵ is a Lorentzian, eqns. (1) and (3) take a particularly simple form [5]:

$$\Delta R/R = (\hbar\theta)^3 \operatorname{Re}[A e^{i\phi}(E - E_g + i\Gamma)^{-m}] \quad (4a)$$

$$\Delta R/R = (\hbar\theta)^3 L(E - E_g, \Gamma) \quad (4b)$$

where

$$L(E - E_g, \Gamma) = [\operatorname{Re}[A e^{i\phi}(E - E_g + i\Gamma)^{-m}]] \quad (4c)$$

In eqns. (4a) and (4c), A is the amplitude and ϕ is a phase angle which accounts for eqn. (1) and the influence of non-uniform electric fields as well as interference and electron-hole interaction effects [4,5]. The lineshape factor $L(E - E_g, \Gamma)$ is independent of the modulating field in the low-field regime.

The parameter m in the lineshape factor of eqn. (4c) depends on critical point type. For a three-dimensional critical point, M_0 , such as the direct gap of GaAs, ϵ can be expressed as

$$\epsilon \propto (E - E_g + i\Gamma)^{1/2} \quad (5)$$

In this case, $m = 2.5$. For a two-dimensional critical point $m = 3$ [5].

In a fully depleted space charge region (SCR), if modulation from flatband is considered, the applied modulating voltage ($V_{a.c.}$) and modulated field ($F_{a.c.}$) are related by [5]

$$F_{a.c.}^2 = (2qN/\kappa\epsilon_0)V_{a.c.} \quad (6)$$

where N is the net carrier concentration, κ is the static dielectric constant and ϵ_0 is the permittivity of free space. Equation (6) also assumes that all of the modulating voltage appears across the SCR. Under the above conditions, eqn. (4b) can be rewritten as

$$\Delta R/R \propto qNV_{a.c.}L(E - E_g, \Gamma) \quad (7)$$

Raccah *et al.* [46,47] and Garland and Raccah [48] have proposed that in certain cases, particularly for material that contains a high defect density, second and first derivative terms should be added to eqn. (3), i.e.

$$\Delta E = (1/E^2)[(1/12)(\hbar\theta)^3(\partial^3/\partial E^3) + 2\Delta\sigma^2(\partial^2/\partial E^2) - \Delta E_g(\partial/\partial E)](E^2\epsilon) \quad (8)$$

Equation (8) has been designated as the generalized functional form (GFF) of EM. The term $\Delta\sigma^2$ results from the polarization of defects by the modulating field. The factor

ΔE_g is a consequence of either the piezoelectric strain that can occur along certain crystallographic directions in polar materials, in which case it is linear in $F_{\text{a.c.}}$ [49], or from the electrostriction of defects, in which case both linear and quadratic terms in $F_{\text{a.c.}}$ may be important.

It should be noted that, in contrast to eqns. (4) and (6), the EM lineshape of eqn. (8) is not independent of the modulating field, since the electric field cannot be factored out, i.e. $(\hbar\theta)^3 \propto F_{\text{a.c.}}^2$, while the term $\Delta E_g \propto F_{\text{a.c.}}$ (and possibly $F_{\text{a.c.}}^2$).

Garland *et al.* [50] have reported a systematic study of the optical dielectric function in the region of the E_1 , $E_1 + \Delta_1$ features for several semiconductors using ER and spectral ellipsometry. Their results indicate that the proper functional form for $\epsilon(E - E_g, \Gamma)$ in eqn. (3) for GaAs and CdTe is primarily Gaussian, although for $\text{Hg}_{1-x}\text{Cd}_x\text{Te}$ the Lorentzian form is dominant. A Gaussian representation is approximately valid when the broadening is associated with a large number of weak scattering centres and/or statistical inhomogeneous broadening. Thus for GaAs and CdTe the lineshape function of eqn. (4b) for E_1 , $E_1 + \Delta_1$ would be the third derivative of a Gaussian.

3.1.2. Franz-Keldysh oscillations (intermediate field regime)

In the event that the low-field criterion is not satisfied but that $eFa_0 \ll E_g$, the dielectric function can exhibit Franz-Keldysh oscillations (FKOs). We shall again give a simple physical picture of this phenomenon and then present the results of more rigorous theories. In the discussion below it will first be assumed that $\Gamma=0$.

Under the influence of an electric field F in the z -direction, the energy bands are tilted by an amount qFz . An electron attempting to tunnel from the valence band into the conduction band sees a triangular barrier. If during the tunnelling process the electron interacts with a photon of energy E the effective width of the barrier to be traversed has been made smaller. The classical WKB approximation gives the same result as a more detailed treatment, so the former will be used. The probability of transmission T through the barrier is given by [11]

$$T = \exp\left(-\int k dz\right) \quad (9)$$

where

$$\hbar k^2/2\mu_{||} = E_g - E - qFz \quad (10)$$

The integral of eqn. (9) taken between the classical turning points yields

$$T = \exp[-(4/3)\eta^{3/2}] \quad (11a)$$

with

$$\eta = (E_g - E)/\hbar\theta \quad (11b)$$

Equation (11a) contains most of the essential features of FKO. For $\eta > 0$ ($E < E_g$) the transmission probability is exponential as a consequence of the photon-assisted tunnelling. However, for $\eta < 0$ ($E > E_g$) the transmission probability becomes an oscillatory function. A more rigorous treatment can be found in Aspnes [5].

The exact form of $\Delta R/R$ for the intermediate-field case with broadening is quite complicated and involves the evaluation of the Airy function in the upper complex plane. Asymptotic series are given in ref. 51 and are used to fit the experimental data. Aspnes

and Studna [52] and Aspnes [53] have written a relatively simple expression:

$$\Delta R/R \propto \exp[-2(E - E_g)^{1/2}\Gamma/(\hbar\theta)^{3/2}] \times \cos[(4/3)(E - E_g)^{3/2}/(\hbar\theta)^{3/2} + \chi][E^2(E - E_g)]^{-1} \quad (12)$$

where Γ is the broadening parameter and χ is an arbitrary phase factor. From eqn. (12), the position of the n th extremum in the FKO is given by

$$n\pi = (4/3)[(E_n + E_g)/\hbar\theta]^{3/2} + \chi \quad (13)$$

where E_n is the photon energy of the n th extremum. A plot of $(4\pi/3)(E_n - E_g)^{3/2}$ vs. the index number n will yield a straight line with slope $(\hbar\theta)^{-3/2}$. Therefore the electric field (F) can be obtained directly from the period of the FKOs if $\mu_{||}$ is known.

To illustrate the effects of broadening, eqn. (12) is plotted in Fig. 5 for values of $\Gamma/\hbar\theta = 0.5$, 1.0 and 2.0, with $\hbar\theta = 25$ meV. For clarity, the abscissa is taken as $\eta = [(E_g - E)/\hbar\theta]$. For the smallest Γ it is possible to observe about 9–10 FKOs. For $\Gamma = 1.0 \times \hbar\theta$, 4–5 FKOs are still observable, while for the largest broadening parameter the FKOs are completely damped out. In this case the lineshape is in the low field third derivative regime of eqn. (3).

Aspnes [53] has stated that, based on eqn. (12), a plot of $\ln[E_n^2(E_n - E_g)]|\Delta R/R|_n$ vs. $2(E_n - E_g)^{1/2}/(\hbar\theta)^{3/2}$ should yield a straight line with slope $-\Gamma$. However, care must be taken in utilizing this relationship to evaluate Γ , since the densities of states of real materials may not remain parabolic sufficiently far from the critical point. Also, for inhomogeneous fields the oscillations may not retain enough coherence to the degree needed. This may be the reason why Aspnes and Studna [52] were not able to obtain accurate values of Γ by using eqn. (12).

The period of the FKOs is determined by the dominant field in the structure. There are two limiting cases to be considered. If modulation is from flatband, i.e. no d.c. field, then the field is clearly the modulating field, $F_{a.c.}$. However, a more interesting situation occurs when there exists a large d.c. electric field, $F_{d.c.}$, in the material and a small modulating field is applied, i.e. $F_{a.c.} \ll F_{d.c.}$. In this case the periods of the FKOs are given by $F_{d.c.}$ and not $F_{a.c.}$ [54].

The treatment of FKOs discussed above has assumed a uniform electric field. However, in many situations this is not the case. For example, in the space charge region (SCR) of

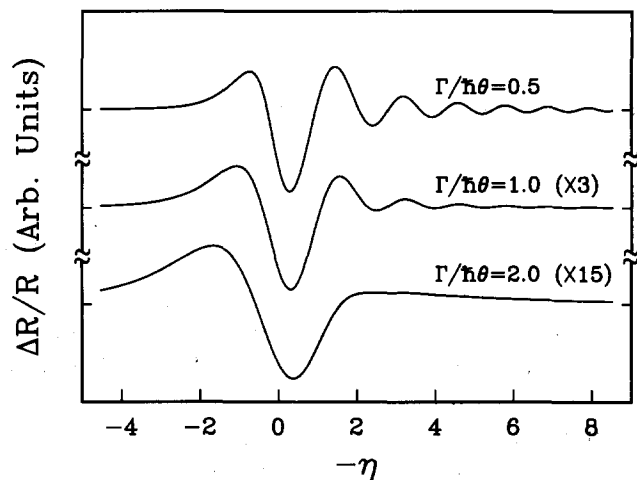


Fig. 5. Plots of $\Delta R/R$ from eqn. (12) for different values of $\Gamma/\hbar\theta$, with $\hbar\theta = 25$ meV.

a doped semiconductor the field is non-uniform and varies linearly with distance (z) from the surface. For non-uniform fields the effective change in the dielectric function $\langle \Delta\epsilon \rangle$ can be expressed as [5,54]

$$\langle \Delta\epsilon \rangle = -2iK(E) \int \exp[-2iK(E)z'] \Delta\epsilon[E - E_g, F(z')] dz' \quad (14)$$

where $K(E)$ is the complex propagation vector of the light in the solid.

Several authors have considered the effect of non-uniform fields on $\Delta\epsilon$ in the FKO regime [54–62]. It has been clearly demonstrated that for small modulation the FKOs are a measure of the maximum field in the structure, not the average field [58,59]. For EM in the small modulation situation not only is ϵ modulated but also the width ($W(F_{d.c.})$) of the SCR. The resultant signal of eqn. (13) comes only from a small near-surface region $\Delta W (\ll W)$, where ΔW is the change in the SCR induced by $F_{a.c.} (\ll F_{d.c.})$. In this small portion of the SCR, the field is almost uniform and equal to the surface (maximum) field.

Shen and Pollak [54] have considered the general case of a linear non-uniform field in which $F_{a.c.}$ is not small compared with $F_{d.c.}$. They have shown that even for $F_{a.c.}/F_{d.c.}$ as large as 0.15 the first few FKOs are still determined by $F_{d.c.}$. These authors also have shown that in the presence of both $F_{a.c.}$ and $F_{d.c.} (F_{a.c.} \ll F_{d.c.})$, $\Delta\epsilon$ can be written as

$$\Delta\epsilon \propto (F_{d.c.}^s)^{1/3} (F_{a.c.}^s) \times \text{lineshape factor} \quad (15)$$

where $F_{d.c.}^s$ and $F_{a.c.}^s$ are the surface d.c. and modulating a.c. fields, respectively, and the lineshape factor is given by eqn. (12).

The EM spectra of highly doped semiconductors have been modeled in terms of the Franz-Keldysh and band-filling effects, including the spatial variation of the modulation [63].

The above treatment of FKOs is for bulk material. Tober *et al.* [64] have discussed FKOs from heterojunction samples. Barriers in heterojunctions modify the phase and amplitude of matrix elements and resulting irregularities in the FKOs.

Although FKOs, in principle, could be a powerful method of studying surface/interface electric fields, in practice this has proved to be more difficult. Generally only about 4–5 FKOs can be detected. The reason for this can be understood as follows. In a fully depleted SCR, the quantities $F_{d.c.}^s$, the potential and the net carrier concentration (N) are related by

$$(F_{d.c.}^s)^2 = (2qN/\kappa\epsilon_0)[V_B + V_{bias} - (kT/q)] \quad (16a)$$

where V_B is given by

$$V_B = V_F - V_P \quad (16b)$$

In the above equations, κ is the static dielectric constant, ϵ_0 is the permittivity of free space, V_F is due to Fermi level pinning, V_P is caused by any photo-voltaic effects and V_{bias} is any applied external bias voltage. The term kT/q represents the Debye length correction.

At low doping concentrations, where Γ is small, the electric field may not be sufficiently large to observe FKOs. Increasing the impurity concentration, N , to increase $F_{a.c.}^s$ (see eqn. (16)) also makes Γ larger, probably due to ionized impurity scattering. As a consequence, the FKOs get damped out (see eqn. (12)) and the lineshape becomes third derivative, as illustrated in Fig. 5. Thus, FKOs are generally seen only in the doping range of about 10^{15} – 10^{16} cm $^{-3}$.

Van Hoof *et al.* [65] have devised a structure which makes it possible to observe a large number of FKOs and hence to use EM as an effective probe of surface/interface

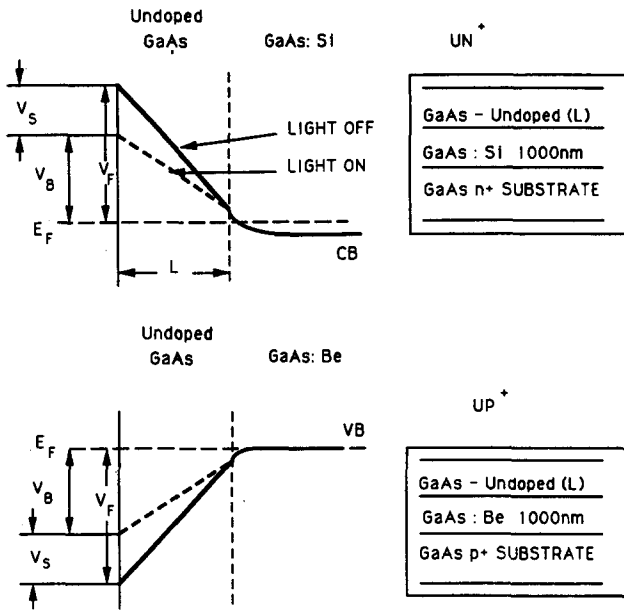


Fig. 6. Schematic representation of the band structures of (a) UN⁺ and (b) UP⁺ configurations for buffer doping levels of $2 \times 10^{18} \text{ cm}^{-3}$ (UN⁺) and $1 \times 10^{18} \text{ cm}^{-3}$ (UP⁺). The influence of light on the barrier height is shown [68].

states. These structures are made by fabricating an undoped layer of thickness L ($\approx 1000 \text{ \AA}$) on a buried doped n⁺(p⁺) buffer on a doped n⁺(p⁺) substrate. Such configurations, which are shown in Fig. 6, have been designated UN⁺(UP⁺) [66–68], respectively (or SIN⁺ and SIP⁺ in ref. 69). In the n⁺(p⁺) buffer/substrate the Fermi level occurs near the conduction (valence) band edge. At the surface the Fermi level is pinned at some value. Therefore there exists in the undoped region (which has a small Γ) a large, almost constant electric field, F . The PR spectrum at 300 K from a (001) GaAs UN⁺ structure ($L = 1100 \text{ \AA}$) is shown in Fig. 7 [66].

Note the large number of FKO's. Plotted in the inset is $(4/3\pi)(E_n - E_0)^{3/2}$ as a function of index n . The solid line is a least-squares fit to a linear function which makes it possible to evaluate the electric field accurately (see eqn. (13)), and hence the built-in potential barrier (V_B).

3.1.3. First derivative spectroscopy

As discussed above, the third derivative nature of EM in the low-field regime is a consequence of the fact that the electric field can destroy the translational symmetry of the material and accelerate the electrons and/or holes. This is not true for bound states. Confined systems, such as the isolated states of quantum wells and multiple quantum wells, excitons, impurities etc., differ significantly from the unbound states of bulk material because the particle (electron or hole) and its wavefunction are localized in space. Because of this confinement, the energies (in the confinement direction for microstructures) are discrete and dispersionless, resulting in an infinite effective mass (in the confinement direction). An applied electric field (along the confinement direction) adds a linear potential, which tilts the confining potential, changing its shape. The electrons and holes become spatially polarized, but still remain confined. This alters both the electronic energies and the wavefunction overlap (intensity, I). Also, the tilting of the potential can result in a change in lifetime Γ as a result of tunnelling.

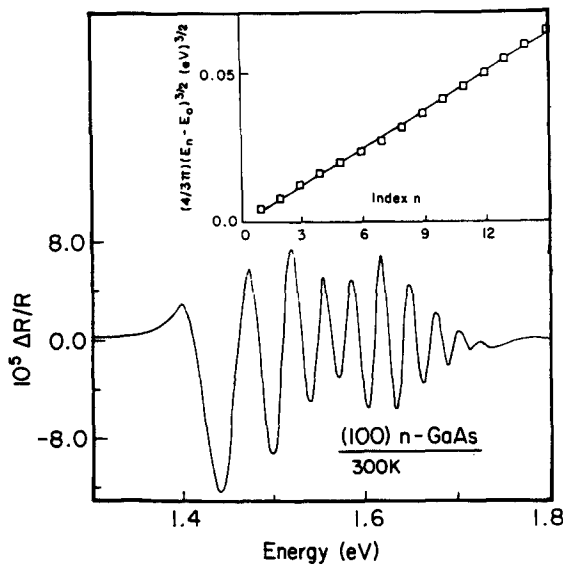


Fig. 7. Photoreflectance spectrum of the UN^+ sample of Fig. 6 at room temperature. The inset shows a plot of $(4/3\pi)(E_n - E_0)^{3/2}$ as a function of FKO index n [68].

In terms of EM, the infinite mass means that eqn. (3) is no longer applicable, since $\hbar\theta=0$. Several authors have treated this problem in detail. They have shown that under these conditions the change in the dielectric function induced by the modulating field, $F_{\text{a.c.}}$, is first derivative [11–15, 70–75] and can be expressed as

$$\Delta\epsilon = [(\partial\epsilon/\partial E_g)(\partial E_g/\partial F_{\text{a.c.}}) + (\partial\epsilon/\partial\Gamma)(\partial\Gamma/\partial F_{\text{a.c.}}) + (\partial\epsilon/\partial I)(\partial I/\partial F_{\text{a.c.}})]F_{\text{a.c.}} \quad (17)$$

This equation can be rewritten as [76]

$$\Delta\epsilon_i = [A_E f_E^{(i)} + A_I f_I^{(i)} + A_\Gamma f_\Gamma^{(i)}](I/\Gamma)F_{\text{a.c.}} \quad (i = 1, 2) \quad (18a)$$

with

$$A_E = (1/\Gamma)(\partial E_g/\partial F_{\text{a.c.}}) \quad (18b)$$

$$A_I = (1/\Gamma)(\partial I/\partial F_{\text{a.c.}}) \quad (18c)$$

$$A_\Gamma = (1/I)(\partial I/\partial F_{\text{a.c.}}) \quad (18d)$$

and

$$f_E^{(i)} = (\partial\epsilon_i/\partial E_g) \quad (18e)$$

$$f_\Gamma^{(i)} = (\partial\epsilon_i/\partial\Gamma) \quad (18f)$$

$$f_I^{(i)} = (\partial\epsilon_i/\partial I) \quad (18g)$$

In the situations discussed above (excitons, impurities, isolated quantum states) the unperturbed dielectric function of eqns. (17) or (18) will be either Lorentzian or Gaussian, depending on the broadening mechanism and/or temperature [11–15, 50, 77]. For isolated quantum wells, the dielectric function is excitonic, even to elevated temperatures, because of the enhanced exciton binding energy caused by the reduced dimensionality. Thus the Lorentzian or Gaussian profile will be appropriate for these quantum microstructures.

Expressions for the Lorentzian and Gaussian dielectric functions and the relevant derivatives (eqns. (17) or (18)) are given in refs. 5, 12 and 13 for the Lorentzian and refs. 11 and 76 for the Gaussian.

It should be noted that in high-quality bulk material grown by techniques such as MBE or vapor phase epitaxy, direct gap excitons may be present even at 300 K [78]. In such cases, the first derivative lineshape form of eqns. (17) or (18) will be appropriate rather than the third derivative profile for band-to-band transitions.

3.2. Thermo- and piezomodulation

Since these modulation methods do not destroy the translation symmetry of the material, the lineshape will be the first derivative expression of eqns. (16) or (17). However, the band gap modulation term is due not to the Stark effect, as in EM, but is created by the temperature (or stress) dependence of the energy gaps. Thus for PZR or TR, eqns. (16) or (17) are appropriate, with $F_{\text{a.c.}}$ replaced by modulated stress ($S_{\text{a.c.}}$) or temperature ($T_{\text{a.c.}}$), respectively.

The appropriate dielectric profile will depend on whether the transition is band-to-band (e.g. eqn. (5)) or excitonic. Camassel *et al.* [79] have demonstrated that even at 300 K the PZR signal from the direct gap of undoped GaSb is excitonic, as mentioned above.

Although FKO's can easily be observed in EM experiments (even in the case of non-uniform fields) with one exception [80] these field-dependent features have not been observed in other modulation experiments such as PZR [81,82] or TR. In principle, either thermo- or piezomodulation (which vary E_g), should produce a derivative-like spectrum similar to EM, which varies $\hbar\theta$. While PZR, TR and EM should produce similar spectra for the uniform field case, this is not true for the non-uniform field situation. For non-EM techniques, eqn. (14) represents a weighted average over all possible field values, since these perturbations vary the dielectric function but not the width of the SCR. Since the magnitude of the field determines the period of the FKO's, this is a weighted superposition of oscillatory features of various periods. Such a superposition tends to diminish the oscillations. However, for the case of EM for a non-uniform field, the resultant signal comes only from a small near-surface region, where the field is almost uniform and equal to the surface (maximum) field. For a structure with a large, almost uniform field, Yin *et al.* [80] have demonstrated that PZR also produces FKO's.

For stress modulation along certain crystallographic directions (e.g. (111) oriented samples) an off-diagonal component of the strain (ϵ_{ij} with $i \neq j$) may be created [83]. In such a situation a piezoelectric polarization field will be produced in polar materials. Thus, in principle, stress modulation can also produce EM. However, such effects will generally be small, since $\epsilon_{ij} \sim 10^{-5}$ for most piezomodulation experiments.

3.3. Differential reflectivity

In this case the lineshape is just the first derivative of the reflectivity with respect to photon energy if the sample or reference have no electric field inhomogeneities. If they do possess spatial electric field variations, the lineshape can contain a third derivative component [84].

3.4. Interference effects

In multilayer systems, optical interference effects may be important. These interference phenomenon can manifest themselves in two ways, for example by changing the relative

contributions of $\Delta\epsilon_1$ and $\Delta\epsilon_2$ in eqn. (1) [77,85–93] and/or the observation of interference fringes [94–96]. For example, as stated above, for uniform bulk materials the Seraphin coefficient, b , is nearly zero at the fundamental gap. Therefore, the modulated lineshape should be determined by the real part of the dielectric function, $\Delta\epsilon_1$. However, the influence of interference effects sometimes produce a non-zero value of b . This effect can be significant in microstructures, which are often clad with protective layers. If the region of interest is not the topmost layer and is located such that the path length difference between it and the surface is an odd multiple of one half the wavelength of the light, then destructive interference can occur. This will manifest itself through a non-zero value for b in eqn. (1) in the vicinity of the direct gap.

4. Bulk properties

This section discusses the use of modulation spectroscopy to study the bulk properties of semiconductors, such as the SCR, carrier concentration, the nature of the band bending (carrier type), impurity effects, deep levels, alloy composition, the influence of static external perturbations such as temperature and uniaxial stress, the effects of crystal growth/processing procedures and annealing procedures and amorphous and microcrystalline material. While a number of these studies have actually been performed on epitaxial (or thin) layers they do not explicitly depend on the nature of the film but are a consequence of their bulk properties. In Section 7 we shall discuss the use of modulation spectroscopy to study epitaxial layers explicitly.

4.1. Space charge region

The SCR (or depletion) region that can exist in semiconductors has played an extremely important role in the study of modulation spectroscopy, particularly EM [2–5]. These SCR are created (a) in the near surface region of doped bulk material due to Fermi level pinning or (b) in the depletion portion of a p–n junction. Trapped charge at a homo- (or hetero-)junction interface also can create an SCR. However, interface properties will be left to a subsequent section. The electric fields that exist in the SCR can be altered by applying an external voltage via a contact (Schottky barrier, MIS, electrolyte–semiconductor), by means of a secondary light beam (photovoltaic effect) or by changing the doping concentration. The well-controlled fields in these configurations have provided a means for studying the lineshapes and basic mechanisms of EM in different field regimes, including the non-uniform field situation.

As discussed above, for sufficiently large fields EM spectra exhibit FKO's whose properties can be used to determine the electric field (if the mass is known), or the mass (if the field is known). However, in almost all of the studies of the SCR in the intermediate field regime the relevant field was $F_{a.c.}$, not $F_{d.c.}$, i.e. modulation to flatband. The exceptions are the early works of Frova and Handler [97] and Handler [98] on electroabsorption from p–n junctions. In fact, in addition to exploring the nature of FKO's, several of these works actually determined interband masses based on a knowledge of the well-controlled field in the SCR [52,99].

In this section we shall describe some recent experiments on the SCR in which the dominant field is $F_{d.c.}$, not $F_{a.c.}$. This former field is determined by two very important parameters of the material, i.e. the built-in potential and net carrier concentration. Thus, an understanding of the nature of EM from the SCR for $F_{d.c.} \gg F_{a.c.}$ can then be used to

obtain information about these quantities. In addition to the FKO's produced by $F_{d.c.}$, many materials also display a small, interference-related structure below E_g , which is the subject of considerable controversy.

Bhattacharya *et al.* [55–57] and Glosser and Bottka [58] have reported ER and PR measurements from the SCR in the Schottky barrier systems ITO/p-InP and Ni/GaAs, respectively. Shi and Anderson [100] have performed an ER study of a metal/n-InP Schottky barrier system. Figure 8 shows the ER spectra in the vicinity of E_0 of the ITO/p-InP Schottky barrier [55–57] at 300 K at bias voltages (V_{bias}) of 1.0 V (dotted line) and 10.0 V (solid line) for a modulating voltage ($V_{a.c.}$) of 0.1 V (peak-to-peak). Since the sample is p-type it is under reverse bias for this sign of V_{bias} . Because of the complexity of this figure the features of the latter spectra are denoted by primes. The extrema above D (D') are FKO's originating in the SCR. As the d.c. field in the SCR is increased by V_{bias} , the extrema in the FKO's spread out, in general agreement with eqn. (19). Similar results were obtained for PR as a function of V_{bias} .

Figure 9 shows the ER spectra for $V_{bias} = 6.0$ V with $V_{a.c.} = 0.1$ V (solid line) and $V_{a.c.} = 1.0$ V (dashed line). The periods of the first seven or eight FKO's (D–K) are identical, while for the features L–O a small difference appears because of competition between the built-in and modulating fields, in accordance with the results of Shen and Pollak [54] discussed above.

From the period of the FKO's the d.c. surface electric field $F_{d.c.}^s$ can be evaluated using eqn. (13) if the reduced mass in the direction of the field is known. It has been shown that the FKO's in the vicinity of E_0 are determined by the transitions from the heavy hole valence band. This is because of the larger density of states in relation to the light hole band. This surface electric field can be related to several important parameters of the system. In a fully depleted SCR the quantities $F_{d.c.}^s$, the potential and the net carrier concentration, N , are related by eqn. (16).

In the work of Bhattacharya *et al.* [55–57] it was found that V_P was not a factor in their sample ($p = 1.5 \times 10^{16} \text{ cm}^{-3}$) while Bottka and Glosser [58] and Bottka *et al.* [59] report $V_P \sim 0.1$ V for n-GaAs ($n \sim 1 \times 10^{16} \text{ cm}^{-3}$).

$(F_{d.c.}^s)^2$ is plotted in Fig. 10 as a function of V_{bias} . As can be seen, the relation is linear, thus making it possible to evaluate N from the slope and V_F from the intercept

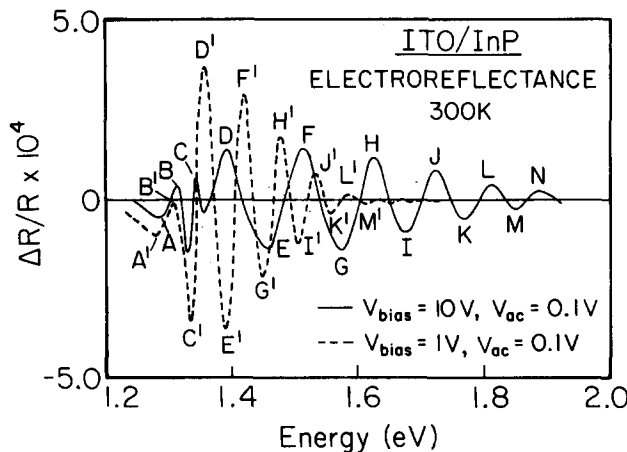


Fig. 8. Experimental electroreflectance spectra for ITO/p-InP for $V_{a.c.} = 0.1$ V with $V_{bias} = 10.0$ V (solid line) and $V_{bias} = 1.0$ V (dashed line) [57].

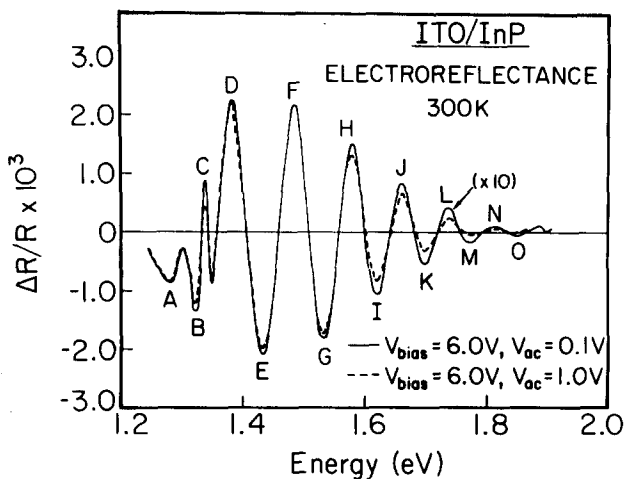


Fig. 9. Experimental electroreflectance spectra for ITO/p-InP for $V_{bias} = 6.0$ V with $V_{ac} = 0.1$ V (solid line) and $V_{ac} = 1.0$ V (dashed line). The former curve has been magnified by a factor of 10 [57].

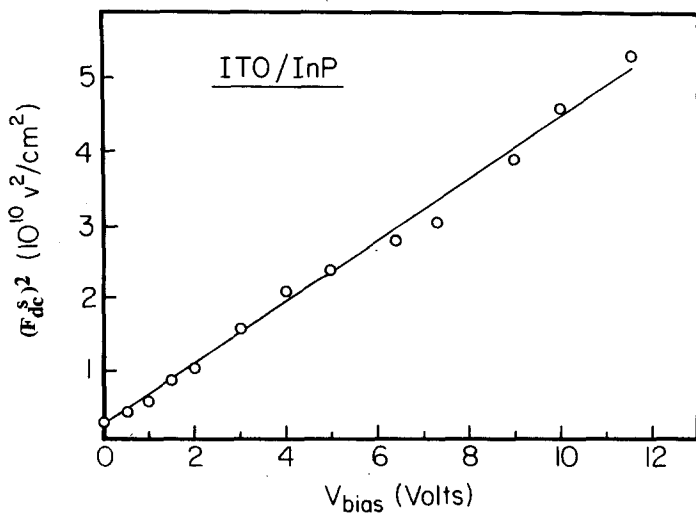


Fig. 10. A plot of the square of the d.c. surface electric field $(F_{dc})^2$ as a function of V_{bias} [57].

(see eqn. (18)). Thus Fig. 10 is a form of a Mott-Schottky plot. It was found that $V_F = -0.45 \pm 0.1$ V and $N = (1.55 \pm 0.1) \times 10^{16} \text{ cm}^{-3}$, in good agreement with the net carrier concentration obtained from Hall effect measurements. The value of V_F measured in this experiment was somewhat smaller than the values deduced from prior studies on InP, which has Fermi level pinning states at 1.2 and 0.9 eV above the valence band. Thus, the surface preparation and ITO treatment of this sample has served to lower the built-in (e.g. Fermi level) potential of the InP.

Glosser and Bottka [58] and Bottka *et al.* [59] have mistakenly concluded, based on an incomplete evaluation of eqn. (14), that the period of the FKO's is a measure of the average d.c. electric field in the SCR layer rather than the surface (maximum) field. This may be the reason why their evaluation of the carrier concentration as deduced from the EM measurements sometimes does not agree with other determinations of the net doping level.

In Fig. 8 the amplitude of the ER signal scales linearly with $V_{\text{a.c.}}$ ($\ll V_{\text{bias}}$) for fixed V_{bias} . This can be explained by eqn. (15), i.e. $\Delta\epsilon \propto F_{\text{a.c.}}^{\text{s}}$. In a fully depleted SCR, for $F_{\text{a.c.}} \ll F_{\text{d.c.}}$, it can be shown from eqn. (16) that [57]

$$F_{\text{a.c.}}^{\text{s}} \approx (qN/\kappa\epsilon_0 F_{\text{d.c.}}^{\text{s}})V_{\text{a.c.}} \quad (19\text{a})$$

and hence

$$\Delta\epsilon \propto qNV_{\text{a.c.}} \quad (19\text{b})$$

It is interesting to note that for small modulations in either the third derivative (see eqn. (6)) or intermediate-field regimes that $\Delta R/R$ is linear in $qNV_{\text{a.c.}}$.

The features labelled A(A')–C(C') below the band gap in Figs. 8 and 9, which are not FKOs, are the subject of some controversy. In contrast to the FKOs, the positions of these peaks are not affected very much by changes in V_{bias} , although there is a change in phase of C' in relation to C. In Aspnes and Studna [52], Bhattacharya *et al.* [55–57] and Bottka *et al.* [59] the A(A')–C(C') features are attributed to exciton interference effects in a portion of the SCR where the electric fields are low enough not to quench the excitons. Application of V_{bias} changes the position of this region in relation to the front of the sample, thus altering the phase. This change of phase with d.c. bias has been termed “spectral rotation” or “lineshape rotation”. Another interpretation will be discussed below.

Batchelor and Hamnett [60] and Batchelor *et al.* [101] have conducted extensive EER studies of p-GaAs in the vicinity of E_0 where there is structure whose phase is dependent on the bias voltage. These spectra are similar to those of Fig. 8. Above the band gap, FKOs are observed whose period varies with V_{bias} , while below E_0 there is structure whose phase is dependent on the bias voltage. These authors have used intermediate-field ER theory to calculate their observed lineshapes. The effect of the inhomogeneous field in the SCR is included by modelling it as a reflection from a series of thin films (slab configuration). From their analysis they conclude that the structure below E_0 is due to multilayer reflection rather than the exciton interpretation given above.

Behn and Roppischer [62] also have conducted experimental and theoretical studies of ER near E_0 in GaAs. Their work also appears to support the field inhomogeneity mechanism, not the effect of excitons, for the “lineshape rotation”. However, they remark that owing to the same bias dependence of both mechanisms (field inhomogeneity and excitons) there is no simple way of distinguishing between them.

Shen and Pollak [54] have solved the problem of the inhomogeneous field using an analytical integral approach rather than the numerical slab analysis of Batchelor and Hamnett [60], Batchelor *et al.* [101] and Behn and Roppischer [62]. They find no evidence for structure below the band gap due to the field inhomogeneity. Jackson and Seebauer [61] have used several methods to solve the inhomogeneous field situation, including the “slab approach”. They demonstrate that in the case of a wide SCR, solving the resulting set of reflectance equations in the slab configuration can give misleading results under some conditions because of subtle numerical problems. Their simulations lend support to an excitonic mechanism for the “spectral rotation”.

The phenomenon of the bias-dependent “spectral rotation” is an example of the interference effects discussed in Section 3.4., i.e. whether the mechanism is excitonic or is due a field inhomogeneity. The bias potential changes the width of the SCR and hence the nature of the interference. The “spectral rotation” thus acts as a kind of Fabry–Perot interferometer, from which it is possible to obtain information about the change in width of the SCR [52,59,102,103].

The “lineshape rotation” discussed above has been used to characterize semi-insulating InP:Fe substrate material using PR at 82 K [104]. It was found that the phase angle of the excitonic transition correlated with the resistivity. The authors contend that since samples with higher resistivities have ionizing electric fields of larger extent this increases the phase angle of the exciton line shape.

The ER lineshape at the fundamental edge for step-like doped semiconductors, i.e. structures consisting of a homogeneously doped layer on a lower-doped substrate of the same material, has been studied theoretically and experimentally [105]. With the electric field penetrating the substrate, a characteristic superposition of the two partial spectra arising from the differently doped semiconductors is found. The change of lineshape with modulation conditions and layer thickness simulated for a GaAs structure has been confirmed by ER measurements using successive layer removal.

Caution should be used when applying eqn. (18) to a step-like doped semiconductor. Poras *et al.* [106] have shown that saturation of the electric field appears when the width of the depletion layer approaches the width of the doped layer itself.

Zass *et al.* [107] have published an interesting ER study (MIS configuration) of the SCR in HgCdTe in the region of E_0 (≈ 116 meV) at 4 K using a Fourier transform spectrometer. Because of the quantized nature of the electron subbands in the SCR, the signal that they observe is a quantum version of Franz-Keldysh oscillations, as discussed in Section 3.1.2.

4.2. Carrier concentration

As has been shown above, the net carrier concentration of a semiconductor can be evaluated by plotting $F_{d.c.}^s$ (from the FKO)s as a function of V_{bias} using contact ER techniques, such as the Schottky barrier method. However, a much more interesting situation would be to use contactless EM methods, such as PR, EBER or CER, to observe the FKO.s. Obviously, in this case $V_{bias}=0$ and a knowledge of V_F and V_P are necessary to obtain N from $F_{d.c.}^s$ (see eqn. (16)). Several workers have indeed used the FKO.s observed in PR to evaluate N in undoped GaAs [107] and in n-GaAs [59,108,109]. In these investigations it was assumed that $V_F=0.73$ V and $V_P\sim 0.1$ V. Sydor *et al.* [110,111] have reported determination of N in undoped and doped $\text{Ga}_{0.85}\text{Al}_{0.15}\text{As}$ using FKO.s.

Several investigators have found that the broadening parameter (Γ_1) of the E_1 , $E_1+\Delta_1$ feature in GaAs varies systematically with carrier concentration, and thus could be used to estimate N [112–116]. These authors believe that the broadening is a result of the doping-produced electric field within the depletion region. However, Badakhshan *et al.* [114–116] find a nearly linear relation between Γ_1 and $\log N$ while Dittrich [112] and Kallegrí *et al.* [113] report that Γ_1 increases linearly with carrier concentration.

Using low-field PR it has been observed that there is a small blue shift of the E_0 gap of n-GaAs as a function of increasing carrier concentration in the range $1\times 10^{16}\text{ cm}^{-3} < n < 8\times 10^{17}\text{ cm}^{-3}$ [117]. These authors thus claim that N can be deduced from the position of E_0 .

The carrier concentration in (001) and (110) polar semiconductors can also be evaluated in a contactless manner using RDS at the E_1 , $E_1+\Delta_1$ transitions [38–40, 118]. Figure 11 shows the optical anisotropy spectra $\Delta R/R$ ($= (R_{110}-R_{\bar{1}\bar{1}0})/(R_{110}+R_{\bar{1}\bar{1}0})$) for reflection from (001) n- and p-type GaAs for different doping levels [40]. In the region of the E_1 , $E_1+\Delta_1$ transitions the spectra show well-defined oscillations. The peak-to-peak magnitude of these oscillations is dependent on sample doping concentration, being larger for high

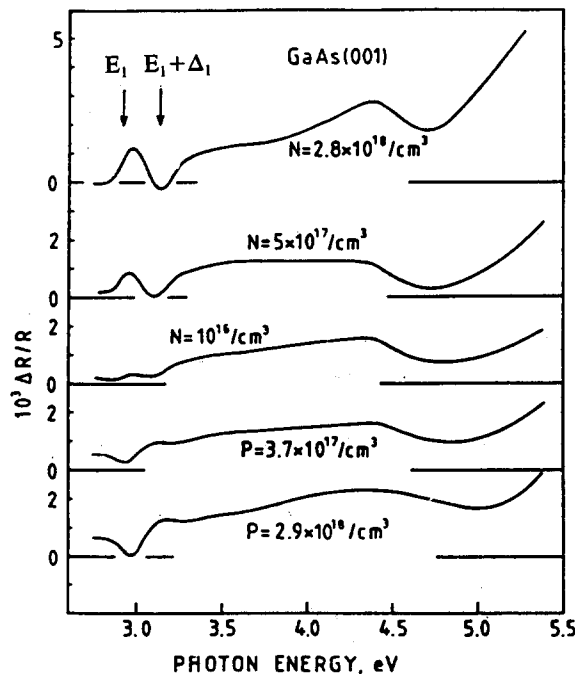


Fig. 11. Optical anisotropy spectra in the (001) GaAs reflectivity as a function of doping level and concentration type [40].

concentrations. Note also that there is a phase change of 180° in going from n- to p-type conductivity. We shall return to this point in Section 4.3 on the nature of band bending.

The impurity-dependent component of the spectra of Fig. 11 is due to an electro-optic effect induced by the SCR field discussed above. There is a shift in oscillator strength from one transition to the other which is linear with $F_{\text{d.c.}}$. Thus, for a given value of V_F (i.e. Fermi level pinning) the field, and hence the electro-optic effect, will depend on N (see eqn. (16)). It should be pointed out that for a given carrier concentration this method could also be used to investigate changes in the Fermi level in a contactless manner (see Section 5.1.).

4.3. The nature of band bending (carrier type)

The nature of the band bending at the surface of a semiconductor with a built-in electric field can be evaluated from the phase of the signal (E_0 or E_1 transitions) of EM methods such as ER [5], EBER [20] and CER [17,18], as well as from RDS (E_1 only), as mentioned above. Farrell *et al.* [119] have used RDS from (001) ZnSe to verify the p-type character of the material. However, the phase of the minority carrier PR method cannot be used for this purpose.

The reason for the phase change in ER associated with the nature of the band bending can be understood as follows. Consider n-GaAs, in which the bands are bent upward. If a modulating voltage is applied such that in the first (second) half-cycle $V_{\text{a.c.}}$ increases (decreases) the surface field an ER signal of certain phase will be produced. However, in p-type material the first (second) half-cycle will decrease (increase) the field, thus leading to an opposite phase. Thus, flatband could be determined by observing the change in phase of ER signals. This will be discussed in more detail in the section on electrochemistry. In

PR, the modulating light beam drives both n- and p-type material towards flatband, and hence there is no phase change.

4.4. Impurity effects

Impurity effects can be manifested in several ways in modulation spectroscopy. As discussed above, the net ionized impurity concentration influences the surface electric field as well as the energy of band gaps and line broadening parameters. However, impurities can also have more explicit effects. In some experiments, structure below the band gap is observed (not the "lineshape rotation" discussed above), which has been attributed to impurities. In addition, impurity scattering may serve to broaden the lineshape of certain transitions. Some of these impurity related peaks also are discussed in the section on process/growth-induced and annealing effects.

Glembocki *et al.* [120] have reported a detailed EER, Schottky "frame" ER and photoluminescence study of impurity-related, below-band-gap electroabsorption features (EA) in bulk Sn- and Si-doped GaAs as well as in thin epitaxial layers of GaAs and $\text{Ga}_{1-x}\text{Al}_x\text{As}/\text{GaAs}$, with and without a known carbon impurity. A correlation was observed between the below-gap ER structure and impurity-related emission from the conduction band and/or donor levels (when present) to acceptor states. These authors suggest that impact ionization is the mechanism which allows observation of impurity transitions in ER.

Figure 12 shows a series of ER spectra at 300 K of Sn-doped ($n \sim 1 \times 10^{17} \text{ cm}^{-3}$) GaAs in the region of the E_0 and $E_0 + \Delta_0$ transitions. The topmost trace was taken in the Schottky "frame" geometry and shows only a peak labelled I_1 at 1.383 eV. Note that there are no E_0 and $E_0 + \Delta_0$ features. The two bottom spectra were obtained in the EER configuration at different bias voltages. Both data exhibit the GaAs structure as well as I_1 . At more positive biases (bottom trace) there is an additional structure labelled I_2 . Since the features

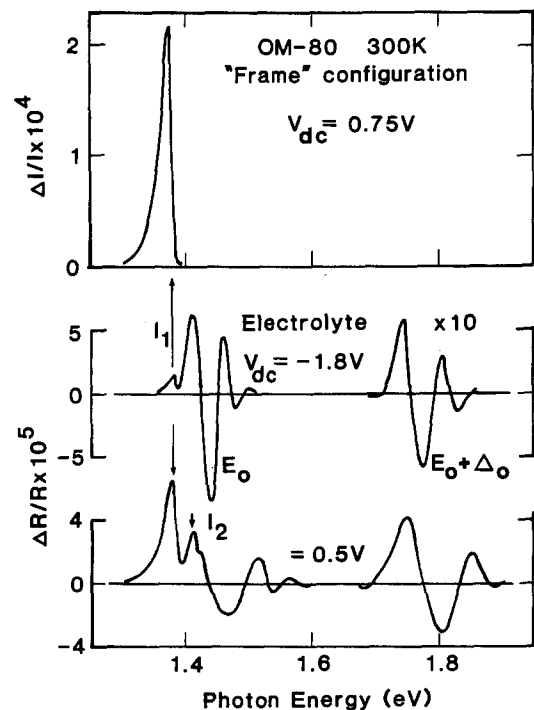


Fig. 12. Electroreflectance spectra of a Sn-doped GaAs substrate material [121].

I_1 and I_2 are observed at below-gap photon energies, where the material is transparent, they are produced by EA rather than electroreflectance, as in the case of the E_0 and $E_0 + \Delta_0$ structures; that is, the impurity-related features are due to back surface reflection (BSR) effects. By correlating the below-gap EA structure with PL data Glembocki *et al.* were able to identify I_1 as being due to a combination of acceptor-donor and acceptor-conduction band transitions, while I_2 is related to valence band-donor excitations.

Tober and Bruno [121] have performed PR, PZR and transverse ER measurements on SI GaAs as well as doped GaAs:Si ($\approx 3 \times 10^{18} \text{ cm}^{-3}$) and GaAs:Zn ($\approx 1 \times 10^{18} \text{ cm}^{-3}$). They also conclude that the observed large below-gap features are linked not only explicitly to impurities but also to BSR effects. At 5 K the extrema of the impurity-related features roughly correspond to energies associated with donor and acceptor states, although this is not true at 300 K. Shen *et al.* [122] have reported PR and TR experiments on SI GaAs. For the latter spectrum they observed a peak about 50 meV below E_0 which was tentatively ascribed to an impurity. Pikhtin *et al.* [123] have reported below-band-gap structure in a PR study of thick, doped GaAs/GaAlAs epitaxial layers and high-quality undoped bulk GaAs. Brierly and Lehr [124] find that the strength of the first derivative peak observed below E_0 in SI GaAs can be correlated with the bulk residual acceptor concentration. The presence of below-band-gap features related to various impurity levels has been reported in a PZR experiment on GaAs/GaAlAs HEMT structures [82] as well as a PR study of GaAs/GaAlAs HBT structures [125].

A comparative study of Cu, Mn and C impurities ($\geq 1 \times 10^{16} \text{ cm}^{-3}$) in bulk LEC grown GaAs has been performed using EBER (300 K) and PL (4 K) by Herman *et al.* [126]. For undoped samples no structure below the band-gap is found in the EBER. For doped materials, characteristic below-gap impurity transitions are observed in both spectroscopies. However, in general the estimated impurity binding energies by EBER are not equivalent to established PL or deep level transient spectroscopy (DLTS) values.

Behn and Roppischer [127] have conducted a detailed experimental and theoretical study of BSR effects on ER spectra. They conclude that the below-band-gap peak at about 1.38 eV frequently seen in the 300 K ER spectra of GaAs is due to BSR electro-absorption effects related to the Urbach tail rather than explicitly to an impurity transition.

The PR response of thin film (MBE or OMCD) n- and p-type GaAs in the range 1.5×10^{15} to $2 \times 10^{19} \text{ cm}^{-3}$ has been studied in the region of the E_1 transition [113–117]. Both the position and broadening parameters (Γ_1) of this feature were found to vary with doping level. A nearly linear relation between Γ_1 and the logarithm of the carrier concentration was observed. Kallergi *et al.* [95,112] have also investigated the energy and broadening parameter of the E_1 feature of n-GaAs as a function of doping concentration using EER. However, they find that Γ_1 increases linearly with carrier concentration. In an EER study of doped HgCdTe grown by MBE it was also found that Γ_1 becomes broader as the doping level is increased [128].

Raccah *et al.* [129] have reported an EER and photocapacitance study of In-doped GaAs. The EER measurements were made in the region of the E_1 , $E_1 + \Delta_1$ resonances. The authors conclude that the In-doping generates large inhomogeneous strains which locally lower the stability of the zincblende structure in relation to the chalcopyrite structure. This strain also lowers the density of dislocations and antisite defects.

Lee *et al.* [130] have performed PZR and PR measurements on a number of Mn-based II-VI diluted magnetic semiconductors. A signature associated with the Mn^{2+} is

observed in PZR, due to BSR effects, when the energy gap is sufficiently large. The position of this peak is relatively insensitive to the composition of the group II component.

4.5. Deep levels

It has been demonstrated that the frequency dependence of the PR signal can be used to evaluate deep trap states [20,131–135]. Thus, PR can be used as a contactless DLTS method. As mentioned previously, important information can be gained not only from the sharp, derivative-like features of modulation spectroscopy, but also from the studies of other variables, such as the modulation frequency dependence of PR and ER [1].

It has been observed by several workers that the magnitude, $\Delta R/R$, of the PR signal decreases with increasing Ω_m . This dependence of $\Delta R/R$ on Ω_m in PR can be accounted for on the basis of the following considerations [22]. The chopped pump radiation can be considered as a square wave source. When light impinges on the sample, electron-hole pairs are created. These charges are then free to fill traps and modify the electric field strength. These excess carriers change the built-in field in a response time much faster than the shortest characteristic time of the modulation. When the light is switched off, the trap population, and hence electric field strength, are restored with a characteristic time τ . For chopping frequency Ω_m it can be shown that the Fourier transform of the in-phase component of the PR intensity, $[\Delta R(\Omega_m)/R]_{\text{in-phase}}$, is given by [22]

$$[\Delta R(\Omega_m)/R]_{\text{in-phase}} = \sum_{i=1}^n [\Delta R(0)/R]_i f(\Omega_m \tau_i) \quad (20a)$$

with

$$f(\Omega_m \tau_i) = \{1 + 2\pi^2(\Omega_m \tau_i)^2[1 - \exp(1 - 2/\Omega_m \tau_i)]\}/[1 + 4\pi^2(\Omega_m \tau_i)^2] \quad (20b)$$

where τ_i is the characteristic time constant of the i th trap state and $[\Delta R(0)/R]_i$ is the PR signal produced by the modulation of the i th trap state in the limit of $\Omega_m \tau_i \ll 1$. It can be shown that in order to employ the principle of superposition of the contribution of states with different trap times it is necessary to consider the in-phase component of $\Delta R(\Omega_m)/R$, not the amplitude [22].

Using an acousto-optic modulator to chop the pump beam, Shen *et al.* [22] have reported PR measurements up to 100 kHz. It was thus possible to evaluate trap times down to about 40 μ s. The limitation was the response of the lock-in amplifier that they employed.

The modulation dependence of the PR signal (in-phase) in the vicinity of E_0 of a GaAs:Si ($3.3 \times 10^{15} \text{ cm}^{-3}$) MBE epitaxial film at various temperatures is displayed in Fig. 13 [135]. Note that these measurements only go to about 5 kHz. The solid lines are a least-squares fit to eqn. (20), assuming only one trap state. The arrow indicates the obtained τ at each temperature. By plotting $\ln(\tau T^2)$ as a function of $1/T$ it was possible to evaluate a trap activation energy of 0.34 ± 0.04 eV.

The frequency dependence of EM signals also will be discussed in the sections below on electrochemistry (Section 6) and doping superlattices (Section 8.6).

An anomalous splitting in the PR spectra of semi-insulating GaAs in the vicinity of the exciton at 78 K has been reported by Durbin *et al.* [136]. This splitting is affected by several factors, including surface conditions, pump beam intensity and modulation frequency. The authors have correlated this behaviour with the EL2 content of the samples.

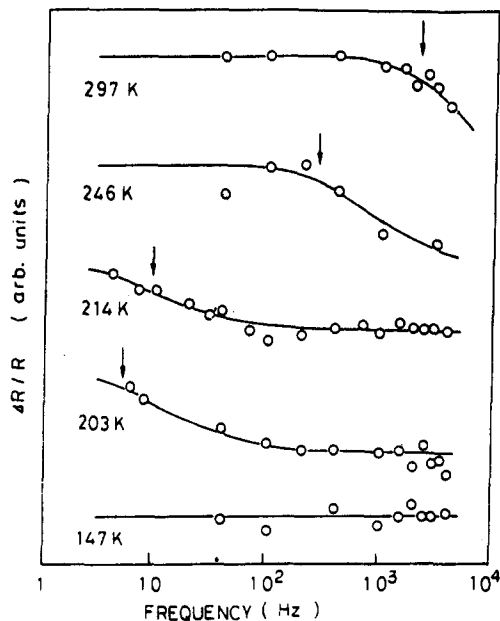


Fig. 13. Modulation frequency dependence of the in-phase component of $\Delta R/R$ for n-GaAs for different temperatures. The solid lines are fits to eqn. (34) yielding τ designated by the arrow [135].

4.6. Alloy composition

An extremely important parameter for the characterization of a semiconductor is the composition of binary $A_{1-x}B_x$ (e.g. $Ge_{1-x}Si_x$), ternary $A_{1-x}B_xC$ (e.g. $Ga_{1-x}Al_xAs$) or quaternary (e.g. $In_{1-x}Ga_xAs_yP_{1-y}$) alloys. The compositional variation of the fundamental gap (E_0) and/or higher lying features (E_1) has been reported for a larger number of alloys including $GeSi$ [137], $GaAlAs$ [94,138,139], $GaAlSb$ [140], $GaAsP$ [141], $GaAlP$ [142], $GaInP$ [143,144], $GaInSb$ [145], $InGaAs$ [146–149], $InAsP$ [147,150], $InAsSb$ [147], $HgCdTe$ [151–153], $HgMnTe$ [154,155], $CdMnTe$ [131,156,157], $CdZnTe$ [130,131], $CdMnSe$ [130], $ZnMnSe$ [158], $GeSi/Si$ [159], $InGaAsP/InP$ [160–162], $GaAlInAs/InP$ [163], $AlGaAsSb/InAs$ [164] and $AlGaInP/GaAs$ [165].

Huang *et al.* [94] have studied the PR and absorption spectra from a series of bulk $Ga_{1-x}Al_xAs$ samples. The Al mode fraction was determined by the use of nuclear resonance analysis, which is a direct and non-destructive method. Figure 14 shows the PR spectra at 300 K for a sample with $x=0.30$. These data exhibit a number of interesting features. The structure at wavelengths shorter than the direct band gap, designated $E_g (=E_0)$ are FKO's which originate in the space charge region of the material. The peak at longer wavelengths is attributed to an impurity. The authors did not attempt a lineshape fit to this complex structure, but based on theory took the band gap energy to be near the first (low-energy side) dominant peak.

The $Ga_{1-x}Al_xAs$ direct band gap as a function of Al composition for $x \leq 0.45$ is plotted in Fig. 15 [94]. The solid line is a least-squares fit to the data yielding the relation

$$E_0(x) = 1.424 + 1.427x + 0.041x^2 \text{ (eV)} \quad (21)$$

valid for $x \leq 0.45$.

The Al composition dependence of eqn. (21) is somewhat different from that originally reported by Berolo and Woolley [138].

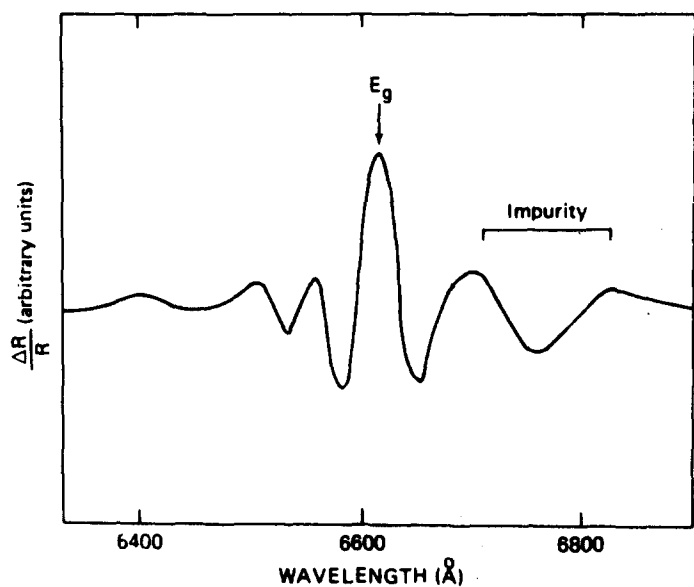


Fig. 14. The photoreflectance spectrum at 300 K from a $\text{Ga}_{0.7}\text{Al}_{0.3}\text{As}$ sample [94].

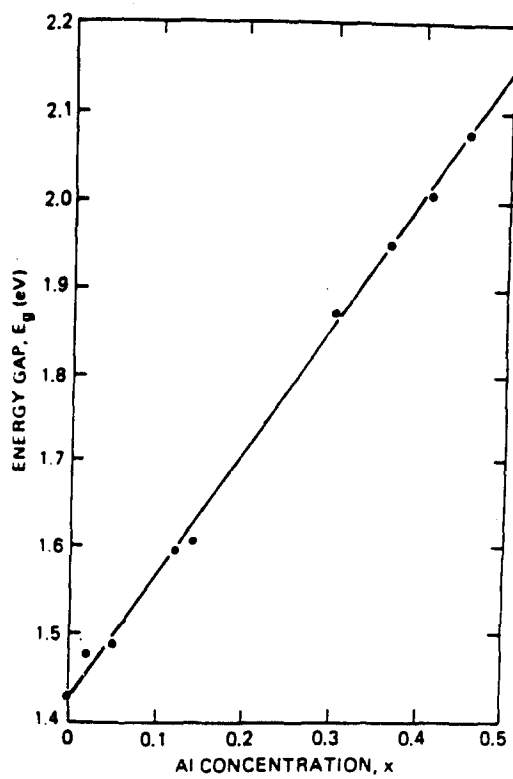


Fig. 15. The direct gap of $\text{Ga}_{1-x}\text{Al}_x\text{As}$ as a function of Al composition [94].

4.7. External perturbations

4.7.1. Temperature

The ability to perform modulated optical experiments over a wide temperature range, particularly by contactless methods, has many fundamental as well as applied ramifications.

The temperature dependence of energy gaps ($E_g(T)$) and broadening parameters ($\Gamma(T)$) can provide important information about the electron–phonon interaction, exciton effects etc. The temperature variation of $E_g(T)$ is due to both lattice dilation and electron–phonon terms. It can be described by equations involving three parameters such as the semi-empirical Varshni expression [166] or the one proposed more recently containing the Bose–Einstein occupation factor for the phonons [167]. Experimental values of two of these parameters can be used to test theoretical models [168–172]. Also, $E_g(T)$ for the fundamental band gap of bulk material is important for comparison with the temperature variation of the quantum transitions in microstructures, as discussed in Section 8.8.2.

The temperature dependence of $\Gamma(T)$ is due only to the electron–phonon interaction and can also be described by a Bose–Einstein type equation [167,170]. For the lowest-lying direct gap, only the longitudinal optic (LO) phonon is involved. Owing to the dimensionality dependence of the electron–LO phonon interaction, $\Gamma(T)$ for the direct gap of bulk material will be quite different in relation to quantum transitions in microstructures. This will be discussed further in Section 8.8.2.

From an applied perspective, the ability to measure band gaps at elevated temperatures (≈ 600 °C) corresponding to growth conditions of MBE, OMVCD or gas phase MBE opens up many new possibilities. For example, the temperature of a substrate material (GaAs, InP) and the quality and composition of epilayers such as $\text{Ga}_{1-x}\text{Al}_x\text{As}$ and $\text{In}_x\text{Ga}_{1-x}\text{As}$ could be monitored *in situ* during the actual growth process [173–178].

4.7.1.1. Temperature dependence of band gaps The contactless EM method of PR has been used to measure the temperature variation of the direct gap (E_0) of GaAs [133,174,175,177,178], InP [177–179], $\text{Ga}_{0.82}\text{Al}_{0.18}\text{As}$ [133,177,178], $\text{In}_x\text{Ga}_{1-x}\text{As}$ ($x=0.06$ and 0.15) [178,180] and Ge [181].

Plotted in Fig. 16 are the experimental temperature dependencies of the direct gap ($E_0(T)$) of $\text{In}_x\text{Ga}_{1-x}\text{As}$ for $x=0.06$ (●) and $x=0.15$ (○) in the temperature range $18 < T < 873$ K [178,180]. Accurate values of $E_0(T)$ (and $\Gamma(T)$) were obtained from a lineshape fit. Representative error bars are shown. The solid lines are a least-squares fit to the Varshni [166] semi-empirical relationship

$$E_0(T) = E_0(0) - \alpha T^2 / (\beta + T) \quad (22)$$

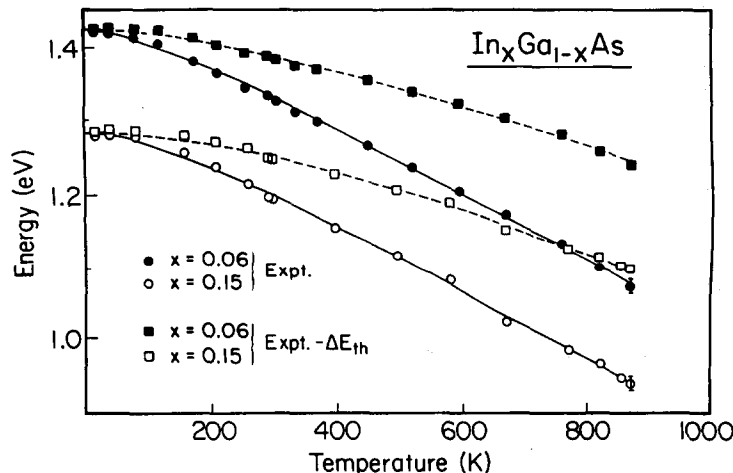


Fig. 16. Temperature dependence of the direct gap of $\text{In}_x\text{Ga}_{1-x}\text{As}$ for $x=0.06$ (solid circles) and $x=0.15$ (open circles). The solid and dashed lines are least-squares fits to eqns. (22) and (25a), respectively [180].

The obtained values of $E_0(0)$, α and β for both samples are listed in refs. 178 and 180. The values α and β for the $In_xGa_{1-x}As$ samples are found to be similar to those of GaAs [133,166,167] because of the low In concentration of the layers. The data have also been fitted to the Bose-Einstein expression proposed by Lautenschlager *et al.* [167]:

$$E_0(T) = E_0(0) - 2a_B/[\exp(E_{ap}kT) - 1] \quad (23)$$

where a_B represents the strength of the electron-average phonon interaction and E_{ap} corresponds to an average phonon energy. The numbers obtained for a_B and E_{ap} [178,180] are again quite similar to the corresponding values for GaAs [167].

The temperature shift of E_0 contains contributions from both thermal expansion and electron-phonon coupling effects. Therefore, in order to obtain parameters directly related to the latter influence, it is necessary to eliminate the contribution of the former. For example, the quantities α and β of eqn. (22) and a_B and $E_{ap}\theta_B$ of eqn. (23) include the influence of the lattice dilation. The energy shift ΔE_{th} due to the thermal expansion can be written as

$$\Delta E_{th} = -3a\alpha_{th}T \quad (24)$$

where a is the hydrostatic deformation potential and α_{th} is the linear expansion coefficient. Equations (22) and (23) can be rewritten as

$$E_0(T) - \Delta E_{th} = E_0(0) - \alpha'T^2/(\beta' + T) \quad (25a)$$

$$E_0(T) - \Delta E_{th} = E_0(0) - 2a'_B/[\exp(E'_{ap}/kT) - 1] \quad (25b)$$

The solid ($x=0.06$) and open ($x=0.15$) squares in Fig. 16 represent data that results from subtracting ΔE_{th} (eqn. (24)) from the experimental values of $E_0(T)$. The dashed lines are least-squares fits to eqn. (25a). These data have also been fitted to eqn. (25b). The obtained values of α' , β' , a'_B and E'_{ap} are listed in refs. 178 and 180.

Manoogian and Woolley [182] have suggested that after the thermal expansion term is removed, the parameter β' of eqn. (25a) is directly proportional to the Debye temperature θ_D by the relation $\beta' = (3/8)\theta_D$. It was found that the agreement between β' and $(3/8)\theta_D$ is quite good for the InGaAs samples.

The parameter α' of eqn. (25a) can be related to a'_B and E'_{ap} of eqn. (25b) by taking the high-temperature limit of both expressions, yielding $\alpha' = 2a'_B/E'_{ap}$. This relation is indeed satisfied for these parameters.

The temperature dependence (80 K $< T <$ 400 K) of the direct gaps of $In_xGa_{1-x}As$ and $In_xAl_{1-x}As$ lattice matched to InP ($x \sim 0.5$) have been measured using PR [183]. From a fit to the Varshni expression (see eqn. (22)) it was possible to deduce values of $E_0(0)$, α and β . Hwang *et al.* [184] have measured the temperature dependence of $E_0 + \Delta_0$, E_1 and $E_1 + \Delta_1$ of InGaAs/InP in the range 83 K $< T <$ 300 K using PR.

The E_1 feature in CdTe [185] and $Hg_{1-x}Cd_xTe$ ($x \sim 0.35$) [186-188] has been studied as a function of temperature using various modulation methods. Values of $E_1(0)$, α and β have been obtained.

Lee *et al.* [189] have measured the temperature variation of the direct gap of $Cd_{1-x}Mn_xTe$ and $Zn_{1-x}Mn_xTe$ and have deduced a coefficient for the linear behaviour of the gap with temperature.

An anomalous temperature dependence for the E_0 and $E_0 + \Delta_0$ transitions in $CuInS_2$ (10 K $< T <$ 300 K) has been observed using Schottky barrier ER [190,191]. Instead of decreasing monotonically with increasing temperature (see Fig. 19), these energy gaps in

CuInS_2 are found first to blue shift (to about 100 K) and then to red shift. This behaviour has been interpreted in terms of the reduction of the d levels in the upper valence band due to thermal expansion and the competition with the electron-phonon interaction.

4.7.1.2. Temperature dependence of the linewidth The temperature variation of the linewidth, $\Gamma(T)$, has been measured for the direct gap of GaAs [192,193], InP [179] and $\text{In}_x\text{Ga}_{1-x}\text{As}$ for $x=0.06$ and 0.15 [178,180] as well as for the E_1 feature in CdTe [185] and $\text{Hg}_{0.65}\text{Cd}_{0.35}\text{Te}$ [188].

The variation of the linewidth with temperature also can be expressed by a Bose-Einstein type expression [167,168]:

$$\Gamma(T) = \Gamma(0) + \Gamma_{ep}/[\exp(E_p/kT) - 1] \quad (26)$$

The first term of eqn. (26) corresponds to broadening mechanisms due to intrinsic lifetime, electron-electron interaction, impurity, dislocation and alloy scattering effects. The parameter Γ_{ep} is an electron- (exciton-) phonon coupling coefficient and E_p is the relevant phonon energy. For the direct gap of semiconductors the appropriate phonon energy is the zone-centre LO phonon, i.e. $E_p=E_{LO}$ and Γ_{ep} is the electron- (exciton-) LO phonon coupling constant [167,168].

The temperature dependence of $\Gamma_0(T)$ is displayed in Fig. 17 for the direct gap of $\text{In}_x\text{Ga}_{1-x}\text{As}$ for $x=0.06$ (\bullet) and $x=0.15$ (\circ) as obtained from a PR measurement [178, 180]. Representative error bars are shown. The solid lines are least-squares fits to eqn. (26). The obtained values of $\Gamma_0(0)$, Γ_{ep} and E_p are given in refs. 178 and 180. It was found that $E_p=E_{LO}$, where E_{LO} for the InGaAs samples was evaluated from Raman scattering. Owing to the low In composition of the material, E_{LO} for the InGaAs was close to the GaAs value (36 meV). Also, it was found that Γ_{ep} (23 ± 6 meV) for both samples was similar to that for the direct gap of GaAs [192,193]. The difference in $\Gamma_0(0)$ seen in Fig. 17 was explained in terms of material quality.

It is interesting to note that the phonon energy (E_p) entering into the temperature dependence of $\Gamma_0(T)$ is generally found to be greater than E'_{ap} , which is appropriate for $E_0(T)$. For the InGaAs materials these quantities are $E_p \sim 33$ meV and $E'_{ap} \sim 25$ meV. The

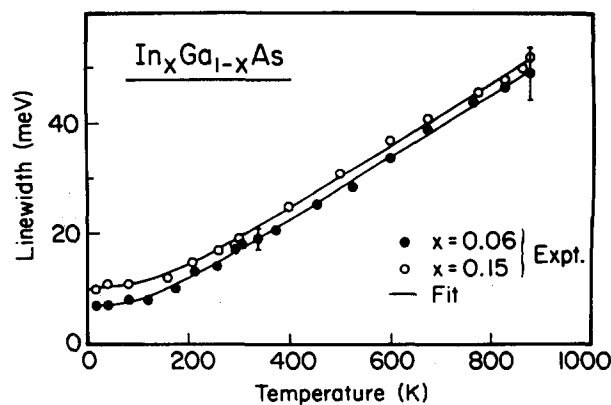


Fig. 17. Temperature dependence of the broadening parameter of the direct gap of $\text{In}_{1-x}\text{Ga}_x\text{As}$ for $x=0.06$ (\bullet) and $x=0.15$ (\circ). The solid lines are least-squares fits to eqn. (26) [180].

reason for this difference is that E'_{ap} represents an average energy for both optic and acoustic phonons, while E_p is the LO phonon energy [165,166].

Ksendzov *et al.* have evaluated $I(T)$ for E_1 of CdTe [185] and $\text{Hg}_{1-x}\text{Cd}_x\text{Te}$ ($x \sim 0.35$) [188].

4.7.2. Uniaxial stress

In the first decade of modulation spectroscopy the combination of this optical technique and static uniaxial stress was developed into a powerful tool for investigating the electronic band structure of bulk semiconductors [194]. While there has recently been little activity in this area, uniaxial stress is being used to explore quantum structures, as discussed in Section 8.8.4.

Photoreflectance at 300 K has been used to investigate the effects of compressive stress along [001] and [110] on the E_0 and $E_0 + \Delta_0$ transition in GaAs [195], $\text{Ga}_{0.78}\text{Al}_{0.28}\text{As}$ [195] and $\text{Ga}_{0.73}\text{Al}_{0.27}\text{As}$ [196]. From the stress-induced shifts and splittings they have evaluated the hydrostatic and shear deformation potentials of these energy gaps. In the latter study the effects of the piezoelectric field generated for stress along [110] were observed. This phenomenon will be discussed further in Section 8.8.4.

The effects of large compressive stress along [100] on the optical features associated with biaxially strained bulk GaAs grown on (001) Si has been observed using PR at 300 K [197,198]. This stress configuration makes it possible to alter the light (LH) and heavy (HH) hole splitting externally. In the bulk material a stress-induced anticrossing of the LH and HH features of the fundamental gap was observed with an interesting polarization effect.

4.8. Process/growth-induced effects and annealing

Modulation spectroscopies, particularly contactless methods such as PR, CER, DR and EBER, are becoming effective tools for studying various process- and growth-induced effects, as well as the influence of annealing. Experiments have been performed in the vicinity of either the E_0 or E_1 features. In some cases, the latter is particularly useful, since the penetration depth of the light in this region is only about 100–200 Å.

Ion implantation damage in silicon has been studied using DR_1 [31–33]. This method can be used to identify whether an implanted layer is crystalline, damaged crystalline or amorphous. The intensity of interband transitions can be used to determine the thickness of a damaged crystalline layer over a submerged amorphous layer. Interference effects were utilized to determine the thickness of the amorphous layer.

A series of differential reflectograms obtained by scanning light of different wavelengths between unimplanted and Si^+ ion-implanted silicon wafers are shown in Fig. 18 [33]. The parameters on the curves are the implantation energies. For all chosen implantation energies, three characteristic silicon interband transition peaks near 3.4, 4.2 and 5.6 eV can be resolved, although the latter feature is very weak. Analysis of the relative peak heights of these structures suggests that the amorphous layer is on the surfaces of implantation energy of 100 keV and lower, but is submerged more than 100 Å for the 120 keV sample.

The features α , β , γ and δ in Fig. 18 originate from interference effects caused by the path difference between beams reflected from the top and bottom interfaces of the amorphous layer. By comparison with a model calculation the thickness of the amorphous layers was evaluated.

Irene and co-workers are making extensive use of the DR_1 approach for the study of silicon surfaces and interfaces, including *in situ* measurements [199–202]. For example, this

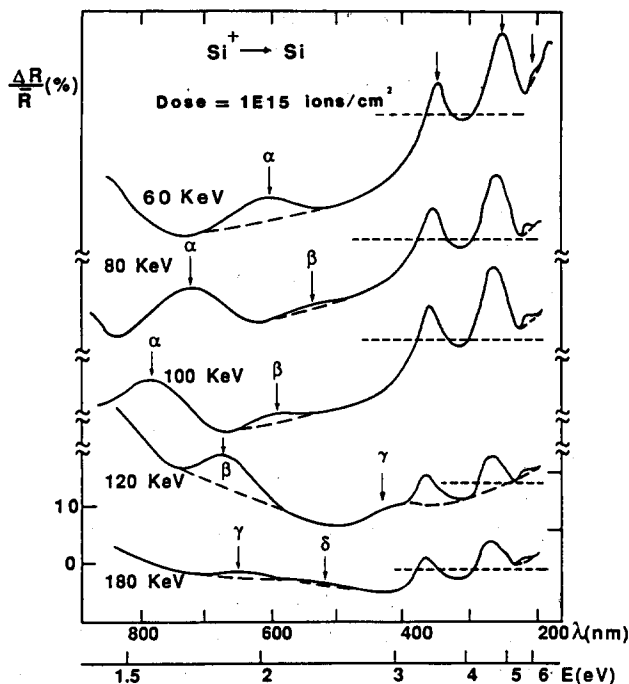


Fig. 18. Experimental differential reflectograms of Si^+ ion-implanted silicon wafers. The implantation energies are shown on each curve. The ordinate is constant for all spectra. The individual curves have been shifted for clarity. The zero points for each curve are shown by dashed lines [31].

method has been applied to study the etching of SiO_2 films on Si substrates *in situ* in the liquid ($\text{HF}/\text{H}_2\text{O}$) environment as well as *ex situ* [199]. These investigators were able to follow the etching experiment *in situ* and in conjunction with simulated spectra and *ex situ* results a new spectral feature is seen which could be evidence for an electric double layer at the Si surface in the etch solution. The DR₁ technique combined with spectral ellipsometry have been employed to characterize the effects of high (60–180 keV) and low (0.1–1.5 keV) energy ion implantation on Si [201].

Both PR and EER have been used to study the effects of reactive ion etching (RIE) damage in Si [203]. The most pronounced effect of the RIE treatments on the spectra was the apparent shift in the E_1 band edge. This shift can be seen at both 77 K and 300 K. This work and previous studies have established that the most pronounced RIE surface modifications are either thin insulator deposition or lattice damage. Therefore, the most self-consistent interpretation of the spectral shift is that it originates from RIE-induced strain in the Si. From the shifts and splittings of the E_1 peak it has been possible to evaluate the near surface damage-induced strain produced by the RIE.

Pollak *et al.* [204] have studied the effects of ion-implantation of 100 keV Si and laser annealing on (001) Si using EER on the 3.4 eV (E_1) structure. These results were compared with TEM, channelling and Raman measurements. It was found that EER was the most sensitive probe of residual strains and that crystal grains smaller than the Rutherford backscattering (RBS) spatial resolution can still give rise to a measurable signal. We shall say more on this subject in Section 4.9 on amorphous and microcrystalline semiconductors.

Gavrilenko and co-workers [205,206] have reported detailed EER investigations of Si with different surface treatments, including ion implantation.

Photoreflectance in the region of the E_1 resonance has been used to study the intrinsic strain at the SiO_2/Si interface in samples prepared by thermal oxidation of (001) Si and subjected to rapid thermal annealing (RTA) [207,208]. The position of the E_1 optical feature has been tracked relative to its position in a reference Si wafer (not intentionally oxidized). From the observed red shifts of the peak the authors deduced both the magnitude and sign (tensile) of the near surface strain in the Si. Changes in linewidth were also detected. Under appropriate RTA conditions it was observed that the strain is completely relieved. These observations are consistent with the compressive strains in the SiO_2 layer as evaluated from infrared transmission, ellipsometry and a laser deflection technique. Strain at the SiO_2/Si interface also has been evaluated using ER in the Schottky barrier configuration [209].

Studies of the influence of Si-, B- or He-implanted GaAs and subsequent annealing has been reported by several authors [210–212] using PR as well as other optical, structural and electrical methods to characterize the damage. Figure 19(a) shows the PR spectra at 300 K around E_0 from an undamaged SI GaAs substrate wafer [212]. Figures 19(b)–(d) are the spectra for Si-implants (120 keV) of different doses ((b) $1 \times 10^{12} \text{ cm}^{-2}$, (c) $1 \times 10^{13} \text{ cm}^{-2}$ and (d) $1 \times 10^{14} \text{ cm}^{-2}$) and subsequent RTA at 800 °C for 10 s. The large feature around 1.4 eV is the E_0 transition. The below band gap features T_1 and T_2 are ascribed to impurity or defect transitions caused by the 120 keV Si implant. The samples in Figs. 19(b) and 19(c) exhibited a few FKOs, in agreement with the discussion above about these oscillations from a bulk SCR. It was thus possible to determine $F_{\text{d.c.}}^s$ for these materials. Using a value of V_F from electrical measurements the authors evaluated the carrier concentration using eqn. (16). The sample with the highest implant level exhibited the

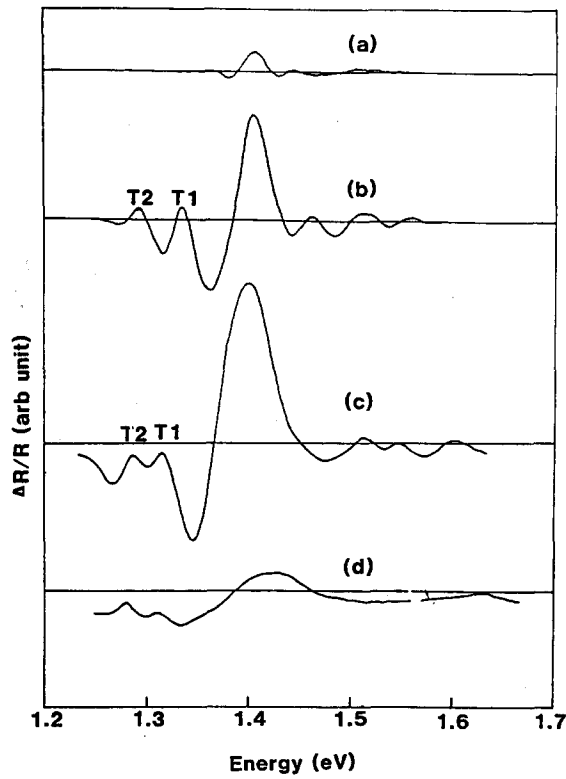


Fig. 19. Photoreflectance spectra from (a) a SI GaAs substrate wafer and, after 120 keV Si implantation and RTA at 800 °C for 10 s, for doses of (b) $1 \times 10^{12} \text{ cm}^{-2}$, (c) $1 \times 10^{13} \text{ cm}^{-2}$ and (d) $1 \times 10^{14} \text{ cm}^{-2}$ [212].

poorest PR signal of the three implanted samples and the FKO_s were absent. The authors conclude that this indicates that the high dose implant caused strong crystal structure disorder, while the chosen annealing condition was not sufficient to remove the damage.

Duncan and Schreiner [213] have studied ion-implanted GaAs:Se with PR. From the observed changes in the period of the FKO_s they have deduced the concentration of electrically active dopants caused by the ion implantation.

The characteristics of the energy band structure (E_0 , $E_0 + \Delta_0$, E_1 , $E_1 + \Delta_1$, E'_0 and E_2) of ion-implanted GaAs and GaP has been probed by EER [214].

The effects of 1 keV Ar-ion bombardment on n-Ga_{1-x}Al_xAs have been studied by EER and PL [205].

The influence of plasma etching on GaAs [215–217] and InP [218] using PR on bulk samples has been reported.

A study of surface damage on GaAs caused by direct exposure to a hydrogen plasma has been reported using DR₂ [35]. The spectra reveal features at photon energies corresponding to the critical points of the GaAs band structure. The observed signal appearing below the GaAs band gap is attributed to defect states created by the hydrogen plasma. Comparison with the DR₂ spectra of samples exposed to an argon plasma suggests that the defect states are caused by ion impact and are independent of the chemical nature of the impinging ions. The density of defect states shows a linear dependence on maximum ion energy. The DR₂ method has also been used as a measurement of the damage profile in GaAs [219]. Damage was created by one of several ion-assisted processes, including sputter etching, reactive ion etching, hydrogenation and ion implantation. A chemical etch was employed to remove various surface layers to evaluate the depth profile of the damage.

A combined technique of EER and Hall measurements for the characterization of thermally converted GaAs surface layers has been reported [220]. Measurements were done in the region of the E_1 , $E_1 + \Delta_1$ features. The high sensitivity of the ER spectra to carrier type conversion was demonstrated by ER depth profiling. Successive anodic oxidation in connection with *in situ* determination of the removed layer thickness provided the position of the p–n junction with high resolution. The p–n junction was identified by observing the change of phase of the EER signal, as discussed in Section 4.3.

A number of groups are making effective use of PR from special UN⁺/UP⁺(SIN/SIP) structures discussed above to study process-induced damage in GaAs using contactless PR or CER [221–223], including *in situ* investigations [221]. From the large number of observed FKO_s (see Fig. 7) it is possible to accurately determine the built-in field accurately and hence the built-in potential (barrier height). Because of the photovoltaic effect in these structures the measured barrier height (V_B) is the Fermi level pinning position (V_F) minus the photovoltage (V_P), i.e. $V_B = V_F - V_P$. A detailed discussion of V_P in UN⁺/UP⁺ structures will be given in Section 5.1. Figure 20 shows the effects of Ar-ion sputtering, thermal annealing and air exposure on V_B at 300 K for both UN⁺[V_B(n)] and UP⁺[V_B(p)] (001) GaAs configurations [221]. The sputtering/thermal annealing portions were carried out *in situ* in a UHV chamber. Also displayed is the sum $V_B(n) + V_B(p)$ and E_g , the band gap of GaAs (1.42 eV). Initially, on the undamaged surfaces the barrier heights $V_B(n) \sim V_B(p)$ are at about midgap. The quantity $V_B(n) + V_B(p)$ is only about 0.15 eV below E_g . This small difference is probably due to the photovoltaic effect, V_P . With increasing sputtering time, $V_B(n)$ decreases while $V_B(p)$ increases, although the sum $V_B(n) + V_B(p)$ remains approximately constant. After 40 min of sputtering, no PR signal could be obtained from the UN⁺ sample, which indicates that the built-in field, and hence V_B (<0.1 V), was too small to observe.

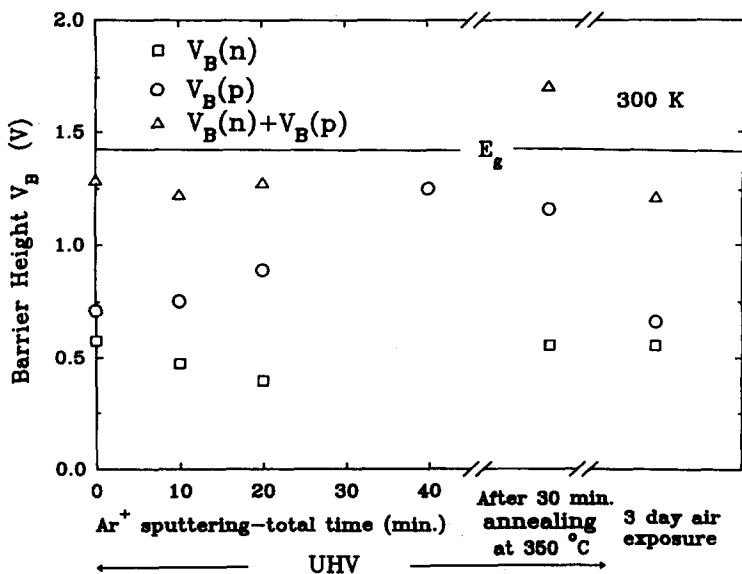


Fig. 20. The measured barrier height, V_B , of UN^+ (□) and UP^+ (○) samples as a function of Ar^+ sputtering times, thermal annealing and air exposure. The triangles are the sum of $V_B(n) + V_B(p)$. The band gap of GaAs, $E_g = 1.42$ eV, is also denoted [221].

Therefore, $V_B(p)$ has a value approximately that of $V_B(n) + V_B(p)$ for the previous conditions. These observations indicate that the major movement in V_B is due to changes in V_F , not to differences in V_p . After 40 min of sputtering, V_F had been moved from midgap to near the conduction band edge for both materials.

Thermal annealing at 350 °C for 30 min in UHV reversed the movement of V_B and hence V_F . The parameter $V_B(n)$ went back to its original midgap value while $V_B(p)$ decreased but did not return to its original value. About three days after the samples were removed from the UHV environment, $V_B(p)$ went back to approximately its original midgap value, while $V_B(n)$ remained unchanged.

It is important to note that if only n-type material had been investigated the interpretation of the changes in $V_B(n)$ would have been ambiguous, e.g. was the decrease due to the unpinning of the surface or pinning at a position closer to the conduction band?

He and Anderson [224] have also investigated the influence of oxygen ion-implanted InP using PR, C-V and DLTS.

Shi and Anderson have used both ER and deep level transient spectroscopy (DLTS) to study the effect of surface treatment and substrate temperature on the characteristics of metal/n-InP interfaces [100]. From the changes in the observed FKOs they were able to deduce information about the effects of these procedures on the Schottky barrier height. A similar study on metal/GaAs Schottky barriers has also been reported [225].

The "lineshape rotation" discussed in Section 4.1 has been employed to evaluate surface polishing damage on semi-insulating InP:Fe substrates [226,227]. Studies of interband transitions (E_0 , $E_0 + \Delta_0$, E_1 and $E_1 + \Delta_1$) and thermal annealing effects on ion-implanted (100) GaSb by PR and Raman spectroscopy have been performed [184].

Photoreflectance has been used to study the effects of B-implanted (001) CdTe before and after annealing [228]. The samples studied were implanted using 100 and 400 keV boron ions to a dosage of $1 \times 10^{16} \text{ cm}^{-2}$ and some were annealed in vacuum at 500 °C for 1 h. The spectral measurements made at 77 K in the vicinity of E_0 indicate three dominant

phases with distinctly different linewidths that may originate in nearly crystalline, partially crystalline and heavily damaged regions in the sample. Some insights into the depth distribution and volume fraction of the three phases were obtained by the following procedures. A study was also made of the spectra in the vicinity of the E_1 optical feature, where the probe penetration depth of the light is only several hundred Å. In addition, lineshape changes in the vicinity of E_0 were investigated by varying the pump beam penetration depth (i.e. pump wavelength) from 2500 Å to less than 400 Å.

Several investigators have reported extensive studies of various processing procedures on the E_1 , $E_1 + \Delta_1$ region of HgCdTe using EER [47,229–233] and CER [222]. In an investigation of the effects of anodization and chemomechanical polishing, the results indicate that Br₂/methanol may damage Hg annealed materials to a depth of ≈ 600 Å, depleting them in Cd and leaving their surfaces with a Te-rich layer [229]. Yin *et al.* [222] have measured the CER spectra at both 300 K and 80 K from bulk Hg_{0.8}Cd_{0.2}Te sputtered with Xe ions. The linewidth Γ_1 yielded information about the damage caused by the process-induced procedure. The influence of thermal broadening on Γ was determined by also performing the experiment at 80 K.

Evidence for stress-mediated Hg migration in Hg_{1-x}Cd_xTe ($x \approx 0.2$) has been found using EER [230]. Measurements were made of the E_1 feature of a cleaved (110) surface before and after removal of cleavage damage. From the position and phase of the signal after cleavage it was deduced that $x = 0.22$ and the surface was n-type. After the damage was removed by etching, the composition (bulk value) had decreased to $x = 0.185$ and the phase had changed sign, indicating that the surface was now p-type. The authors interpret the high x value associated with the n-type surface as an indication that, under stress, the Hg migrates.

Electron beam electroreflectance has been reported on the effects of sputtering with 2 keV O₂⁺ ions on the surfaces of (100) SI GaAs and CdTe [234]. Analysis of the results indicates the existence of distinct surface and bulk signals and gives information about the surfaces before and after sputtering.

The influence of various growth procedures on the quality of Hg_{1-x}Cd_xTe ($x \approx 0.2$) has been studied by EER in the E_1 region [152,235,236]. One investigation dealt with the influence of layer thickness on the quality of Hg_{1-x}Cd_xTe epilayers grown by the interdiffused multilayer process. The results indicate that epilayers grown by this method have reasonable lateral and depth homogeneity and are comparable to liquid phase epitaxy (LPE) materials [236].

Hsu *et al.* [237] have reported a PR study of the temperature dependence of the energy gaps for sulphur-annealed CuInS₂ in the range 10–300 K. The sulphur-annealed sample was found to have larger transition energies, smaller positive temperature coefficients of energy gaps and larger spin-orbit splitting energy than the as-grown sample. The authors explain this in terms of the reduction of d-level contributions in the upper valence band, probably caused by the variation of lattice distance due to native defects.

An EER study of CuInS₂ grown by the travelling heater method has been reported by Hsu [238]. It was found that the energy gap and broadening parameter were functions of stoichiometry.

4.9. Amorphous and microcrystalline semiconductors

In comparison to crystalline materials, relatively little work has been done on the modulation spectroscopy of amorphous (a) or microcrystalline (μ c) semiconductors. Because

there is an internal localized electric field due to disorder inherent in the amorphous structure, no sharp band edge in the density of electronic states, comparable to crystalline materials, has been observed. Moreover, another difficulty in obtaining a well-defined modulation signal is due to interference effects in these thin amorphous samples. Results on a- and μ c-materials have been reviewed by Hamakawa [239] and also are discussed in Hamakawa and Nishino [4]. In this section we shall present some recent results in this area.

The optical properties of μ c-Si have been investigated by EER and spectral ellipsometry [240]. Figure 21 shows the EER spectra of various samples produced under different chemical vapour deposition (CVD) conditions, yielding different grain sizes ranging from 3600 Å (Fig. 21(a)) to 390 Å (Fig. 21(e)). The dashed lines are least-squares fits to eqn. (9c) for a two-dimensional critical point. The arrows indicate the obtained interband energies. The spectrum for the largest grain size is very similar to that of crystalline Si. The lowest energy feature is E'_0 , while the next is E_1 . Generally, at 300 K these peaks cannot be resolved, the dominant contribution coming from E_1 , which originates from the lowest transition along the Λ direction of the Brillouin zone. The next two features are designated E_2^Δ and E_2^Σ and arise from Δ and Σ transitions near the X point of the BZ. The highest-lying peak is assigned to E'_1 , which is due to higher-lying Λ transitions. The effect of decreasing grain size is to broaden the peaks and to cause some small red shifts. For the smallest grain

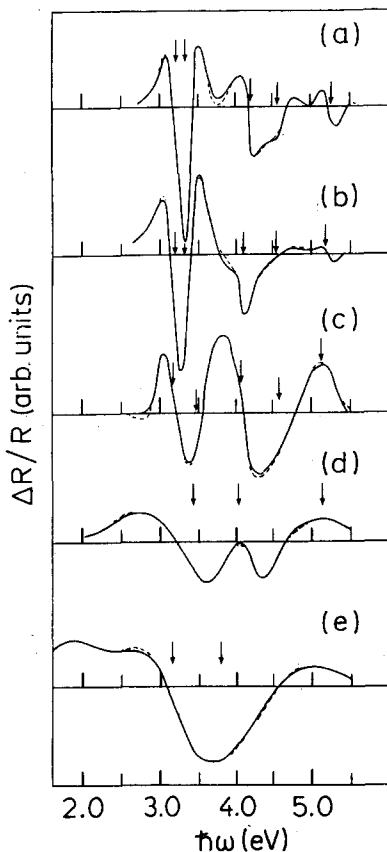


Fig. 21. Electroreflectance spectra (solid lines) of CVD μ c-Si produced under different conditions. The dashed lines are least-squares fits to eqn. (4a) for a two-dimensional critical point [240].

size, only the E'_0 , E_1 structure is still observed. These results are consistent with the spectroellipsometry measurements. The behaviour has been interpreted in the context of a calculation based on the mutual crystal approximation in tight binding theory [240].

Studies of the EER spectra of μ c-C films have made it possible to observe two energy gaps within the spectral range 1.0–5.6 eV. These results also have been compared with a theoretical model [241].

Gavrilenko *et al.* [242] also have reported an EER investigation of a-Si in relation to different polytypes (FC-2, 2H-4, BC-8 and ST-12).

Bhattacharya *et al.* [243] have determined the fundamental band gap of a-MoS₃ prepared under different conditions using both EER and transmission measurements. They find that the band gaps as evaluated by EER are about 100 meV higher than those transmission data. Such a difference has also been observed in similar comparisons of a-Si:H [239]. By comparing the EER spectrum of a-MoS₃ with those of c-MoS₂ and poorly crystallized (px) MoS₂, Bhattacharya *et al.* [243] were able to conclude that their a-MoS₃ can easily be converted to c-MoS₂ or px-MoS₂.

5. Surfaces and interfaces

Almost since its inception it has been recognized that EM could be used as an effective probe of surfaces and interfaces. This is not only because of the sharp, derivative-like features, but also because of its sensitivity to electric fields. In addition to spectral features, other variables, such as frequency dependence, phase and pump wavelength (in the case of PR) can provide important information. However, until recently little work has been done in this area. For example, as discussed above, the FKOs observed in EM are a direct measure of the built-in d.c. electric field that exists at surfaces/interfaces due to Fermi level pinning. The nature of the surface band bending, including flatband, can be determined by the phase of EM methods such as ER, CER and EBER. RDS at the E_1 , $E_1 + \Delta_1$ features from the (001) and (110) surfaces of polar materials can also be used for this purpose, as discussed above.

In this section a number of other experiments will be reviewed that have probed the surface/interface of semiconductors and semiconductor structures. Studies of the semiconductor/electrolyte interface will be discussed in Section 6 on electrochemistry. Also, work on the two-dimensional electron gas (2DEG) that can exist at modulation-doped heterojunction interfaces such as GaAlAs/GaAs will be left to Section 8.7.

Although FKOs, in principle, could be a powerful method of studying surface/interface electric fields, in practice this has proved to be more difficult. The spectrum of Fig. 11, in which about 10 FKOs are observed, is quite unusual for the SCR of a doped semiconductor. Generally only three or four FKOs can be detected. The spectrum of Fig. 19 is more typical of doped material. The reason for this effect has been pointed out in Section 3.1.2. The large number of FKOs from the UN⁺/UP⁺ structures discussed above makes it possible to use EM as an effective probe of surface/interface states.

5.1. Surfaces

Fermi level pinning at semiconductor surfaces and interfaces is a challenging subject of investigation from both fundamental and application-oriented points of view [66,68,69,221]. There exists at many semiconductor surfaces/interfaces an appreciable density of uncontrolled

electronic states, whose origin is still a topic of controversy. These states tend to "pin" the location of the Fermi level at these surfaces/interfaces at some characteristic energy (V_F). Hampering efforts to identify the physical mechanisms responsible for this Fermi level pinning have been the narrow ranges of reported Fermi stabilization energies themselves, which permit a number of quite dissimilar explanations. The Fermi level position at the surface cannot simply be derived from its bulk value, but must be measured separately for each surface, each of which may differ in crystallographic orientation and reconstruction, surface chemistry or environment.

In the past, the main experimental method of studying Fermi level pinning at the semiconductor surface/interface has been soft X-ray photoemission (SXPS). However, as recently pointed out by several investigators [244–247], surface photovoltaic (V_P) effects in SXPS are an important factor. The measured barrier height V_B is thus the difference between V_F and V_P , i.e. $V_B = V_F - V_P$. The effect of light on V_B is shown schematically in Fig. 6.

Electromodulation methods such as PR are of considerable interest and usefulness, since they are contactless, employ very low light levels, require no special mounting of the sample, and can be performed in any transparent ambient medium, including ultra-high vacuum (UHV). From the FKO observed in the PR spectra, the built-in electric field and hence V_B can be accurately determined. Information about charge transfer mechanisms at the surface/interface can also be obtained since EM is the optical response of the system to the modulating field and can be performed over a wide temperature range. In spite of the low light levels employed, the influence of V_P must also be considered in the EM determination of V_F .

Shen *et al.* [69] and Yin *et al.* [66–68,221,222] have effectively used these UN₊(UP₊) structures to study Fermi level pinning effects at (001) GaAs and (001) GaAlAs surfaces. Yin *et al.* [66–68,221,222] have performed measurements as a function of temperature (77 K < T < 450 K), pump beam wavelength ($\lambda_p = 633$ nm and 407 nm) and W-metal coverage (in situ in a UHV chamber). Results have also been reported on the changes in V_F due to Ar⁺ sputtering and thermal annealing [243].

The relation between the electric field F (as determined from the FKO) and V_B can be written as [68,221]:

$$V_B = FL + (kT/q) + SCC \quad (27)$$

where the second term is the Debye length correction and SCC is the space charge correction of the buffer layer. The expression for the SCC depends on whether the material is degenerate or non-degenerate [68].

The values of V_B are plotted in Fig. 22 as a function of temperature for (001) GaAs UN₊ and UP₊ structures using a pump beam intensity ($P_{a.c.}$) of 3 $\mu\text{W cm}^{-2}$ (633 nm) and a probe beam (P_{pr}) intensity of 2 $\mu\text{W cm}^{-2}$ [68]. This figure demonstrates that below room temperature, V_P (= $V_F - V_B$) is an appreciable factor and that V_B saturates at about 400 K for these low light levels.

The temperature dependence of V_B , based on current transport theory, can be expressed as [68]

$$V_B = V_F - (\eta kT/q) \ln\{[J_{pc}/rJ_0(T)] + 1\} \quad (28a)$$

where η is an ideality factor, J_{pc} is the photo-induced current density and $J_0(T)$ is the saturation (dark current). The parameter r is a geometry factor given by:

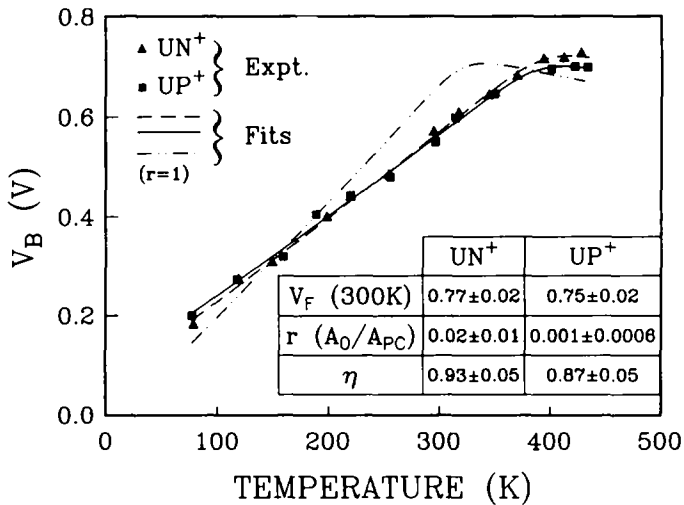


Fig. 22. The measured barrier height, V_B , of UN^+ (\blacktriangle) and UP^+ (\blacksquare) samples as a function of temperature. The solid (UN^+) and dashed (UP^+) lines are least-squares fits to eqn. (28). The obtained values of $V_F(300)$, r and η are shown in the inset. The dot-dashed line is a least-squares fit (UN^+) for $r=1$ [68].

$$r = A_0/A_{pc} \quad (28b)$$

where A_0 is an effective area which contributes to the dark current mechanism and A_{pc} is the illuminated area. Since all the photo-generated carriers in both the drift and diffusion regions are collected, J_{pc} can be expressed as [68]

$$J_{pc} = qR\gamma(1-R)/\hbar\omega \quad (29)$$

where P is the light intensity, γ is the quantum efficiency ($=1$), R is the reflectivity of the light at the semiconductor surface and $\hbar\omega$ is the photon energy. The saturation current density $J_0(T)$ is given by [68]

$$J_0(T) = [(A^{**}T^2)/(1+BT^{3/2})] \exp[-qV_F(T)/kT]. \quad (30)$$

where A^{**} is the modified Richardson constant and B is a constant related to the saturation velocity. The temperature dependence of the Fermi energy, $V_F(T)$, is assumed to follow the same dependence as the band gap (see eqn. (36)). A similar photovoltaic effect in PR has been observed in a p-i-n structure by Airaksinen *et al.* [248].

The solid lines in Fig. 22 are least-squares fits to eqn. (28a), yielding the values of $V_F(300)$, r and η indicated in the inset [68]. The values of $V_F(300)$ for the n- and p-type materials add up to the band gap and are in good agreement with other determinations. In order to demonstrate the necessity of including the geometry factor r , the authors have also fitted the UN^+ curve setting $r=1$ (dot-dashed curve). As can be seen, the fit is not very good.

The values of r have made it possible to determine the density of surface states (D_s) on the n ($D_n = (1 \pm 0.6) \times 10^{13} \text{ cm}^{-2}$) and p ($D_p = (6 \pm 4) \times 10^{11} \text{ cm}^{-2}$) surfaces based on the assumption that there is one state per atom on the (001) surface.

Several authors have reported the use of these UN^+ (UP^+) GaAs structures to study the effects of various processing procedures, such as dry etching, surface passivation and metallization [68,221–223]. The reader is also referred to Section 4.8.

Recently, modified UN^+ (UP^+) structures have been used to study the Fermi level pinning in low-temperature MBE-grown GaAs [249–253] and the piezoelectric effect in a

(111) grown InGaAs/GaAs system [254,255]. These results will be discussed in Section 7 and Section 8.5.2.

Information about surface states and V_F has also come from a study of the time constants involved in PR from several GaAs UN^+ structures [256]. The rise and fall times were determined from a digital oscilloscope trace. The dependence of the rise and fall times on intensity and wavelength of the pump and probe beams can be accounted for by a theory based on majority carrier flow, as discussed above. The characteristic time observed can be used to determine V_B . Figures 23(a) and (b) show the responses of the PR signals monitored at a probe wavelength (873 nm) with $P_{\text{pr}} = 28 \mu\text{W cm}^{-2}$ and $P_{\text{pr}} = 2800 \mu\text{W cm}^{-2}$, respectively. The pump power (633 nm) was $0.5 \mu\text{W cm}^{-2}$. Figure 23(c) shows the results for $P_{\text{pr}} = 28 \mu\text{W cm}^{-2}$ and $P_{\text{ac}} = 5000 \mu\text{W cm}^{-2}$. The rise and fall times were obtained by a least-squares fit to an experimental decay. These authors conclude that, since the rise and fall times are approximately equal, the dynamics of the PR in these structures are not related to a trap state but are due to majority carrier flow, as discussed in eqn. (30). The time constant for the system can be written as [256]

$$\tau = RC = (\kappa\epsilon_0/L)(kT/q)(1/A^{**}T^2) \exp(qV_B/kT) \quad (31)$$

The barrier heights V_B determined from their analysis of the time-dependent data are in good agreement with those deduced from the observed FKOs.

The effects of photowashing on the Fermi level and surface state density have been investigated on bulk (001) n-GaAs using the FKO observed in PR by Gaskill *et al.* [257] and Shen *et al.* [258]. Both groups have found that this procedure results in a decrease of

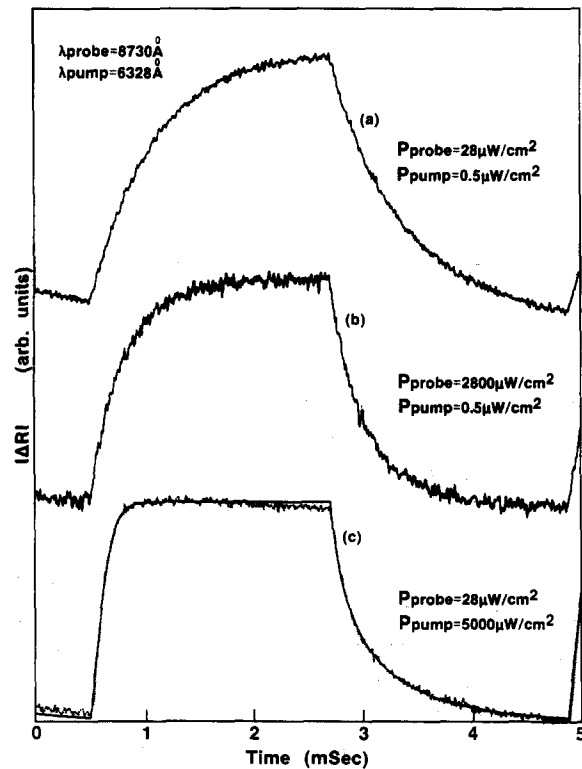


Fig. 23. Photoreflectance signal rise and decay curves from a GaAs UN^+ structure for a probe beam wavelength of 873 nm. The dotted line in curve (c) is non-exponential. The solid lines are least-squares fits to eqn. (31) [256].

about 25% in the built-in potential. The latter authors have also deduced a reduction in the surface state density by about a factor of 2. The effects of sodium sulphide passivation on (001) bulk GaAs have also been studied by RDS [259]. Hildebrandt *et al.* [260] have performed a PR investigation of the modification of surface/interface gap states due to Sb deposition, $(\text{NH}_4)_2\text{S}_x$ and Se vapour treatment on (110) bulk GaAs.

The oxidation and annealing of (001) GaAs has been studied by PR from both the E_0 and E_1 transitions [261]. The phase dependence of the signals was also monitored. The PR spectra of air-oxidized and annealed surfaces are shown to be substantially different from those of the clean surface. Spectra at the E_0 and E_1 features respond quite differently to these treatments. These differences are explained on the basis of an optical interference phenomenon due to excitons that occur only at E_0 (see Section 4.1). The observed changes in phase of the in-phase/out-phase components of the signal are interpreted in terms of slow surface states.

The built-in potential at the surface of MBE-grown epitaxial GaAs/GaAs has been evaluated from PR measurements in the low-field case, where no FKO's are observed [262]. An increase of the surface potential due to gold deposition was also observed. Based on current transport theory, similar to eqn. (28), Kanata *et al.* [262] have written down an expression for the modulated photovoltage of PR ($V_{\text{a.c.}}$) in terms of the power density of the modulating pump beam, ($P_{\text{a.c.}}$), as well as a d.c. bias beam, P_b . In this derivation it is assumed that all the photogenerated carriers are collected from both the drift and diffusion regions (see eqn. (29)). The expression for $V_{\text{a.c.}}$ is thus

$$V_{\text{a.c.}} = (kT/q) \ln \{[P_{\text{a.c.}} \gamma(1-R) + P_b \gamma(1-R)S]/[P_b \gamma(1-R)S]\} \quad (32\text{a})$$

where S is given by

$$S = (A^{**}T^2\hbar\omega/q)[\exp - (qV_F/nT) + 1] \quad (32\text{b})$$

The authors also show that

$$\partial^3 V_{\text{a.c.}} / \partial (\ln P_{\text{a.c.}})^3 = 0 \quad (33)$$

has only one solution for $P_{\text{a.c.}}$, designated as $P_{\text{a.c.,e}}$.

In the low-field regime of a fully depleted SCR, the PR signal $\Delta R/R$ is linear in $V_{\text{a.c.}}$ (see eqn. (12)). Thus, the dependence of $\Delta R/R$ on $P_{\text{a.c.}}$ is given by eqn. (32a). These authors also show that

$$(P_{\text{a.c.,e}} - P_b)/T^2 = [A^{**}\hbar\omega/q\gamma(1-R)][\exp - (qV_F/nT) + 1] \quad (34)$$

Figure 24 shows the dependence of the amplitude of the PR signal of the direct gap of GaAs as a function of $P_{\text{a.c.}}$ at different temperatures for $P_b = 0.088 \text{ mW cm}^{-2}$. The 633 nm line of a He-Ne laser was used for both pump and bias sources. The solid lines are least-squares fits to eqn. (32a). The values of $P_{\text{a.c.,e}}$ are obtained by taking the third derivative of the solid lines. These are indicated by arrows.

In Fig. 25, $\ln[(P_{\text{a.c.,e}} - P_b)/T^2]$ is plotted as a function of $1000/T$ for a bare GaAs surface (O) and a Au/GaAs Schottky barrier (Δ). The solid lines are least-squares fits to eqn. (34), yielding values of V_F indicated in the figure. The value of 0.78 eV for Au/GaAs is quite similar to that obtained by other workers for the bare and metal-covered (001) GaAs surface, i.e. the Fermi level is pinned near midgap [67-69,233,234].

The effects of using different (110) p-InP surfaces (air-exposed, metal-covered and annealed) on the surface Fermi level position have been studied by PR, including *in situ* measurements in a UHV chamber [263].

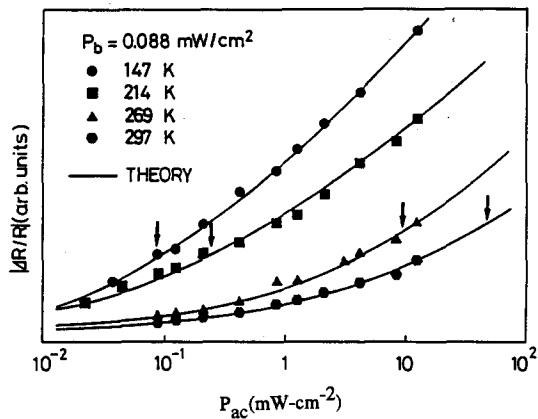


Fig. 24. Dependence of $|\Delta R/R|$ on P_{ac} measured at 147 K (●), 214 K (■), 269 K (▲) and 297 K (●) with P_b of 0.088 mW cm^{-2} . The solid lines are least-squares fits to the theory, and $P_{ac,e}$ are denoted by arrows [262].

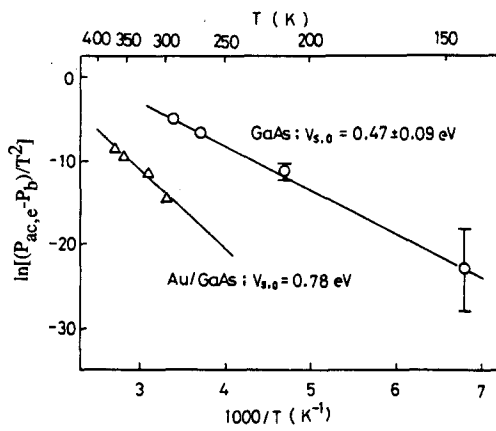
Fig. 25. The plot of $\ln[(P_{ac,e} - P_b)/T^2]$ as a function of $1000/T$. The symbols ○ and △ are the plots for as-grown GaAs and Au/GaAs, respectively [262].

Raccah *et al.* [264] have performed EER measurements from the (111)A and (111)B faces of CdTe in the region of the E_1 transition. The lineshape was fitted using the GFF of eqn. (13). From the (111)A face the lineshape fit requires a large first derivative (piezoelectric) component, a contribution that is absent from the B face signal. These authors associate this effect with two-dimensional interfacial strains between the A face and a thin native oxide that is formed in the electrolyte. They conclude that there exists a region of greatly lowered stability associated with the oxidized A face but not with the oxidized B face.

5.2. Interfaces

The electric field distributions of $\text{Ga}_{0.83}\text{Al}_{0.17}\text{As}/\text{GaAs}(\text{buffer})/\text{GaAs}$ (SI substrate) heterostructures have been determined using PR [22]. By varying both the pump beam wavelength and modulation frequency (up to 100 kHz) the authors were able to identify the component layers; their quality and the properties of the various interfaces. The results yield evidence for a low density of states between the GaAs buffer layer and GaAlAs layer and a relatively large density of interface traps between the substrate and buffer regions. From the frequency dependence of the amplitude of $\Delta R/R$ (see eqn. (20)) from the different regions it was possible to deduce the relevant trap times and because measurements were made up to 100 kHz, trap times as short as 40 μs could be deduced.

Kassel *et al.* have used EER to characterize ZnSe/GaAs and ZnSe/AlAs interfaces [265–267]. They interpret features in the spectra as being due to interface crossover transitions to triangular well interface states. The existence of these well states provided the first unambiguous proof that the ZnSe/GaAs interface is type I. From the observation of these transitions they were able to calculate band offsets and band bendings as well as diffusion lengths across each interface and the amount of interdiffusion. These authors determined band profiles and interdiffusion parameters by solving Poisson's equation and the Schrödinger equation for a net of assumed values of interdiffusion parameters and for the position of the GaAs band edges at the interface. Values for these quantities were then deduced by requiring consistency with the experimental EER results as well as C–V measurements. It was thus possible to obtain information about the height and depth of the interface barrier



induced by interdiffusion, the position of the bands at the interface relative to the Fermi energy and the built-in field on each side of the interface. This work was the first to determine band-edge energies as a function of depth, and thus to show the existence of a conduction band interface barrier induced by interdiffusion, and to measure the short-range interdiffusion.

Figure 26 shows the EER spectra at 300 K of two ZnSe/n⁺GaAs heterojunctions used in this study [267]. In sample 1 (Fig. 26(a)) the ZnSe epilayer was doped as a p-n junction, with the n⁺ layer adjacent to the interface. For sample 2 (Fig. 26(b)) the ZnSe was unintentionally doped. The solid lines are fits to eqn. (13), with the lineshape modified to a primarily Gaussian form [50]. For sample 1 the GaAs (≈ 1.4 eV) and ZnSe (≈ 2.7 eV) spectra are greatly broadened and distorted by the high built-in fields. the GaAs spectrum is also blue-shifted by about 0.1 eV. For sample 2 the only visible effects of the high built-in field are found in the broadening and distortion of the GaAs spectrum. In the fit of the ZnSe spectra in the vicinity of the E_0 transition, for both samples it was necessary to introduce four oscillators in order to reproduce all the features of the lineshape.

Sydot *et al.* [110] have published results on a PR investigation of GaAs/GaAs and GaAlAs/GaAs interfaces (MBE grown) including the effects of temperature, doping, epilayer thickness and pump laser intensity. Lu *et al.* [268] also have reported a similar study for MBE GaAs/GaAs. From the temperature dependence of the observed FKOs they have extracted the temperature dependence of the surface Fermi level.

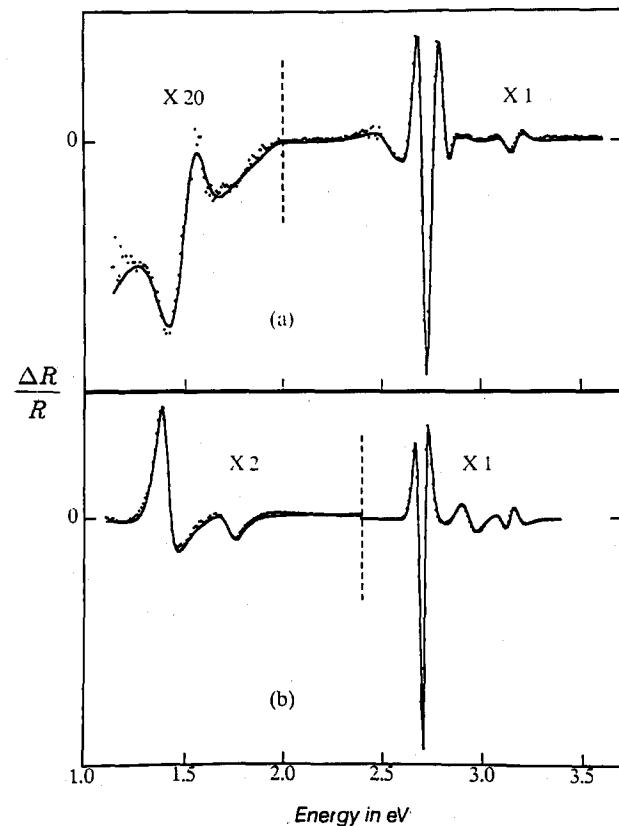


Fig. 26. Electrolyte electroreflectance spectra for ZnSe/n⁺-GaAs samples 1 (a) and 2 (b). For details see text [267].

Goldhahn *et al.* [269] have characterized GaAlAs/GaAs heterojunctions using EER in connection with successive layer removal by anodic oxidation. This technique applied to GaAlAs/GaAs double heterostructures makes it possible to localize the p-n junction with respect to the heterointerfaces. Also, information about the depth distribution of the Al composition has been obtained.

The effect of a thin Ge layer on the surface depletion region of GaAs has been investigated by PR [270]. From the observed changes in the GaAs FKOs, the variation in built-in voltages was deduced.

Several groups have reported the effects of hydrogen passivation in GaAlAs/GaAs structures using EM and PL [271–273]. Cappizzi *et al.* [271] used PR at 300 K and 80 K and PL at 77 K to investigate a heterostructure consisting of 1.1 μm of MBE $\text{Ga}_{0.83}\text{Al}_{0.17}\text{As}$ grown on a 0.8 μm MBE buffer on a (001) SI GaAs substrate. For the PR study, not only was the lineshape (including amplitude) from the GaAs and GaAlAs regions investigated, but also the phase delay angle between the laser excitation and response was monitored. The behaviour of the amplitude and phase angle of the PR signals at 300 K is indicative of the disappearance of surface and interface defects at early stages of hydrogenation. Deep trap passivation in the bulk gives rise to increased PL emission in both the GaAlAs and GaAs signals, the effect being large only for the latter. A concomitant decrease in the phase angle delay was detected. The optimum occurred when the total dose of H ions reaching the surface was $\approx 10^{17} \text{ cm}^{-2}$. When larger doses of H were attained, a high density of new bulk defects developed in the GaAs, which virtually eliminated the PL and reinstated a large phase delay.

6. Electrochemistry

As discussed in several sections above, EM can be used as a powerful method for studying the properties of surfaces and interfaces, including Schottky barriers. Because this modulation method is sensitive to electric fields, many different aspects of the EM signal, such as phase, frequency dependence, amplitude and pump wavelength (PR), can be employed to obtain information.

While EER has been one of the most useful methods of studying the band structure of semiconductors [1–3, 5] it can also be used to investigate the properties of the semiconductor/electrolyte interface, i.e. for electrochemistry. In many respects this interface is very similar to the metal/semiconductor interface, i.e. Schottky barrier.

A number of workers have used EM, particularly EER, to investigate the behaviour of the semiconductor/electrolyte interface. In particular, information has been obtained about the flatband potential, potential distributions, surface states, Fermi level pinning, surface passivation and degradation mechanisms [153, 203, 274–285].

As discussed above, for the case of small modulation the EM signal from the SCR can be written as $\Delta R/R \propto qNV_{\text{a.c.}}L(E - E_g, \Gamma)$ (see eqns. (7), (15) and (19)). This relation is based on the assumption that all of the modulating voltage ($V_{\text{a.c.}}$) appears across the SCR. However, in some circumstances this may not be the case, and only a fraction, f , of $V_{\text{a.c.}}$ may be dropped across the SCR, so that

$$\Delta R/R \propto f[qNV_{\text{a.c.}}L(E - E_g, \Gamma)] \quad (35a)$$

For the case of Fermi level pinning at the semiconductor/electrolyte interface, the parameter f can be expressed as [203, 275, 281]

$$f = [1 - (q/C_h)(\partial N_{ss}/\partial V)] \quad (35b)$$

where C_h is the capacitance of the Helmholtz layer (which corresponds to the entire surface covered with states that can be charged and discharged upon modulation of the surface potential) and N_{ss} is the density of the surface states. From an analysis of the variations of the spectral amplitude with the d.c. bias voltage and the modulation amplitude (eqn. (35)), one can obtain a measure of the flatband voltage that directly relates to the properties of the surface and serves as a reference point in any attempt to understand the distribution of the electric field at the interface. One can also obtain the doping level through evaluation of N (Mott-Schottky plot as in Fig. 10) and actively trace the shifts of the Fermi level with the applied bias. When $(q/C_h)(\partial N_{ss}/\partial V) = 1$, the Fermi level is completely pinned, all the potential drop is at the surface and the EM signal reduces to zero. If, on the other hand, $\partial N_{ss}/\partial V = 0$, either because there are no surface states or because their energy is such that they do not charge and discharge as the surface potential is changed, all the potential drop falls on the space charge layer. In this case, the junction behaves as an abrupt junction and the EM signal is independent of the d.c. bias [203,275,281]. From the quantitative evaluation of the functional dependence of the spectral amplitude with the d.c. bias, the density and energy of the surface states that are responsible for the pinning of the Fermi level can be obtained [203,281,283].

An example of these effects has been observed in the bias dependence of the magnitude of the EER signal (E_1 peak) of n-Si in a methanolic solution [283]. These results are shown in Fig. 27. Figure 27(a) displays the variation of the amplitude of the E_1 EER structure with electrode potential after HF etching, while Fig. 27(b) is the result before etching. Flatband can be seen at the potential in which the signal inverts sign and two potential ranges can be seen in which the Fermi level is pinned: one narrow range around -0.4 V vs. Pt, due to the surface states that were mentioned before and another one at potentials positive to -0.2 V vs. Pt, probably due to accumulation of minority carriers at the surface.

Pahk *et al.* [199] have employed DR₁ to study the etching of SiO₂ films on Si substrates *in situ* in the liquid (HF/H₂O) environment as well as *ex situ*.

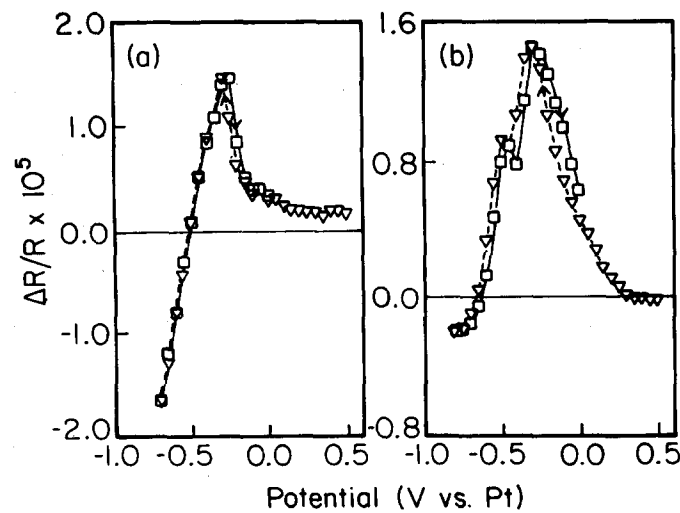


Fig. 27. Variations of the amplitude of the EER signal from the E_1 peak in n-Si with electrode potential: (a) after HF etching and (b) before etching [283].

The EER spectra of n-MoSe₂ and n-WSe₂ under anodic and cathodic bias have been investigated by Scholz and Gerischer [277]. Flatband values inferred from the observed phase change of the signal were in good agreement with those from Mott–Schottky plots.

Batchelor *et al.* [286] have reported an EER study of n- and p-type (001) GaAs in a series of aqueous electrolytes. Their results were modelled by an intermediate-field Franz–Keldysh theory that included the electric field variation within the depletion layer, as discussed in Section 3.1.2 and Section 4.1. Thus they were able to measure the space charge voltage at each applied potential. In all cases, the space charge voltage was found to vary much more slowly than the applied potential on approach to the expected flatband potential. Thus not all the external voltage was dropped across the SCR as discussed above. It was reported that the rapid Fermi level pinning of p-GaAs in 0.1 Mol KOH was passivated by small concentrations of polysulphide ions.

Information about the relaxation time of states at the semiconductor/electrolyte interface has been obtained from the frequency dependence of the PR signal of the E_1 transition of n-Si in air and methanolic solution [284]. For the latter situation, the amplitude of $\Delta R/R$ exhibited a marked decrease with increasing Ω_m because of these surface states. The results were fitted to eqn. (20a) with two sets of surface states with relaxation times of 0.51 ms and 6.5 ms.

7. Epitaxial layers

Various modulation techniques, such as PR, EER and PZR, have been used to study properties of epitaxial layers, such as the strain induced by lattice mismatch and/or growth in SiGe/Si [159], GaAs/Si [287–290], InGaAs/GaAs [183], InAlAs/GaAs [183], InGaAs/InP [291], InGaAsP/InP [161,292], ZnSe/GaAs [189], GaAsP/(111)GaP [293], CdTe/InSb [189], AlGaInP/GaAs [294], CdMnTe/CdTe [295,296], Si/Al₂O₃ [297,298] and ordering in GaInP/GaAs [299–302].

Figure 28 displays the PZR spectrum at 20 K of a 0.1 μm ZnSe pseudomorphic layer grown on a (001) GaAs substrate in the vicinity of the E_0 feature of ZnSe [189]. Note that the spectrum is a doublet rather than the singlet E_0 structure of Fig. 1. The inset is a lineshape fit to eqn. (9c) with $m=2$ using two oscillators. Since the lattice constant of ZnSe is larger than that of GaAs, the pseudomorphic ZnSe epilayer experiences a contraction (compression strain) in the growth plane and hence an extension (tensile strain) normal to this plane. Thus, instead of being cubic the lattice of the ZnSe now has tetragonal symmetry. This reduction in symmetry results in a splitting of the doubly degenerate top of the valence band into “light” (LH) and “heavy” (HH) hole (out-plane) components. It is known from other experiments that the strain described above results in the HH transition being at a lower energy than the LH feature. The fact that in PZR LH features are more intense in relation to HH peaks, in contrast to other modulation methods, is due to the different effects of strain on the two valence levels. This observation, which can be used to identify the nature of HH and LH structures, is discussed in Section 8.3. Shown in the inset is a theoretical lineshape fit using eqn. (4c) with a Lorentzian excitonic profile for the dielectric function, i.e. $m=2$. This fit yields accurate energies for the shift and splitting of the E_0 transition, from which the strain can be evaluated. The observed value of the strain is in good agreement with that deduced from the lattice mismatch.

Nishino *et al.* [299] have measured the ER spectra at 83 K of ordered Ga_{0.5}In_{0.5}P/GaAs fabricated by organometallic vapour phase epitaxy (OMVPE). As a result, it has

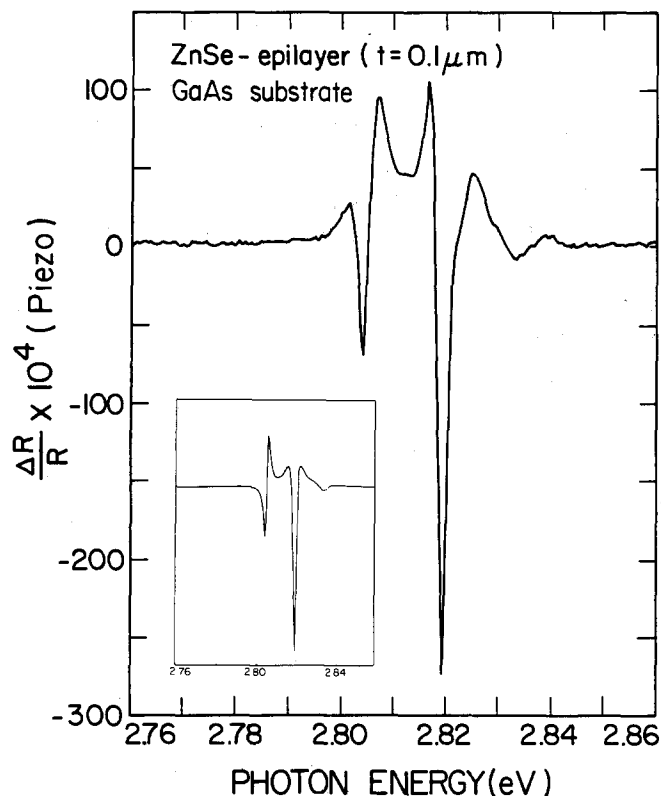


Fig. 28. Piezoreflectance spectrum at 20 K of a 0.1 μm ZnSe epilayer on (001) GaAs in the vicinity of the direct gap of ZnSe. The inset is a theoretical lineshape fit to eqn. (9c) with $m = 2$ using two oscillators [189].

been found that there exist anomalous structures in the region of the E_0 and E_1 band edges of this material. These anomalous structures have never been observed with disordered bulk $\text{Ga}_{0.5}\text{In}_{0.5}\text{P}$ alloys or epitaxial layers grown by liquid phase epitaxy. This investigation was undertaken to explore the observation by transmission electron microscopy that there exists an ordering in the atomic arrangement on the Group III element sublattice in OMVPE-grown $\text{Ga}_{0.5}\text{In}_{0.5}\text{P}$.

Shen *et al.* [249,250], Warren *et al.* [251–253] and Look *et al.* [303] have reported PR studies on low-temperature MBE GaAs with excess As (LT-GaAs). They find essentially no PR signal directly from the LT-GaAs layer. However, by using a modified UN^+ (UP^+) structure, in which the surface of UN^+ is replaced by a LT-GaAs layer and by probing the electric field in the adjacent undoped layer, these authors were able to determine the Fermi level pinning position in the LT-GaAs. Their results strongly support the metallic As precipitate/GaAs theory for annealed LT-GaAs.

Allegre *et al.* [304] have made an unambiguous identification of the HH and LH transitions in strained layer epitaxial systems by comparing wavelength-modulated reflectivity (WMR) and PZR spectra. In the former, the ratio of the HH and LH transitions is 3:1 owing to matrix element effects. However, for the biaxial modulated stress produced by PZR, the LH valence band edge undergoes a shift that is about a factor of two larger than the HH edge. This enhances the former transitions to such an extent as to nearly compensate for the difference in matrix elements. Therefore, the relative intensities of the

HH and LH features are different in PZR as compared to WMR (or PR/ER). This has been verified by investigating a strained CdTe epitaxial layer.

8. Semiconductor microstructures

An extremely significant development in semiconductor research has been the fabrication of synthetic semiconductor microstructures such as QWs, MQWs, SLs and HJs [305,306]. These structures can be grown by a variety of thin film epitaxial techniques, such as MBE, OMCVD, gas phase MBE etc. They can be composed of ultrathin layers ($\approx 100 \text{ \AA}$) of alternating composition (e.g. GaAs/Ga_{1-x}Al_xAs, In_xGa_{1-x}As/GaAs), of alternating doping (e.g. n-GaAs/p-GaAs) or a combination of alternating composition plus doping. Heterointerfaces can be either lattice-matched (e.g. GaAs/Ga_{1-x}Al_xAs) or strained layer (e.g. In_xGa_{1-x}As/GaAs, Si_{1-x}Ge_x/Si). These artificial materials produce a one-dimensional potential along the growth (z) direction such that the electronic bands of the bulk are split into quasi-two-dimensional (2D) quantized subbands.

Modulation spectroscopy is a very powerful tool for investigating many of the fundamental aspects of these microstructures including band offset, well and barrier widths, excitons, strain, coupling (and decoupling) between wells, miniband formation, zone folding in short-period SLs and built-in electric fields. A large variety of III-V, II-VI and GeSi systems have been studied including both lattice-matched and strain layer configurations. There is some evidence that the properties of the 2DEG in MDHJ, MDQW and δ -doped samples can be explored. Also, as in bulk material, this optical method can be used to examine the effects of external perturbations, such as electric and magnetic fields, temperature, hydrostatic pressure, uniaxial stress etc.

Figure 29 shows a single quantum well (type I) that is produced by fabricating a thin layer (L_z) of semiconductor A with band gap E_g^A (e.g. GaAs) sandwiched between two thick layers of material B with band gap $E_g^B > E_g^A$ (e.g. Ga_{1-x}Al_xAs) [305]. Also indicated are the discontinuities in the conduction (ΔE_c) and valence (ΔE_v) bands. For type I (II) heterostructures, $E_g^B - E_g^A = \Delta E_c + \Delta E_v (|\Delta E_c - \Delta E_v|)$, so that in the former the electrons and

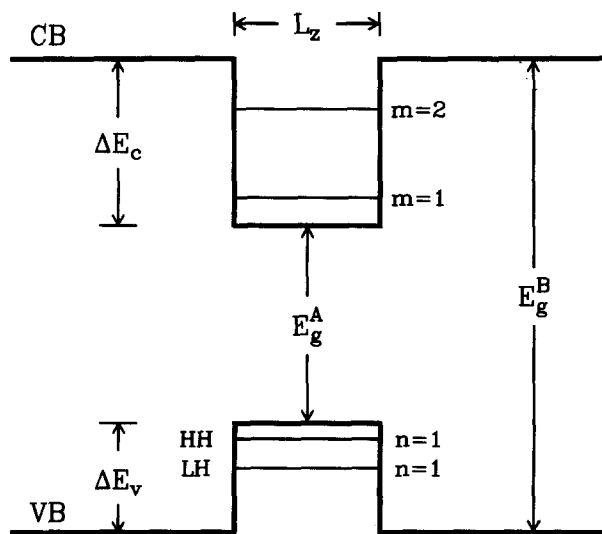


Fig. 29. Schematic representation of the conduction (CB) and valence (VB) band profiles for a type I single quantum well of width L_z [305].

holes have the same spatial confinement while for the latter the electrons are localized in material A and the holes are in semiconductor B. The materials A and B can be either lattice-matched (e.g. GaAs/GaAlAs) or strained layer (InGaAs/GaAs). The quantized energy levels for the electrons and holes are schematically illustrated in Fig. 29. The valence quantum potential removes the heavy and light hole degeneracy of cubic materials, such as diamond- and zincblende-type semiconductors.

The quantization of the energy levels changes the absorption profile from a square root dependence on photon energy of three-dimensional (3D) bulk material (see eqn. (5)) to a two-dimensional (2D) form which consists of a series of quantized step functions independent of photon energy [306]. In addition, the 2D character of the system enhances exciton binding energy effects. The dot-dashed line in Fig. 30(a) shows ϵ_2 for the 3D case of bulk material while the dashed line is the step-like 2D profile. The solid line shows schematically the influence of the excitons. The energy difference between the exciton peak and the corresponding step in the 2D absorption edge is the exciton binding energy.

An MQW is a periodic repetition of the SQW with a barrier thickness (L_B) such that the lowest-lying levels are still discrete (no miniband dispersion), although higher-lying confined as well as unconfined (resonance) states may exhibit marked miniband effects. In an SL there is miniband formation even for the lowest-lying states. In doping SLs the modulation of the potential arises from the periodically alternating n- and p-doping. The superlattice effect (miniband formation) destroys the sharpness of the 2D absorption profile, as illustrated schematically in Fig. 30(b). There are singularities (critical points) in ϵ_2 corresponding to the centre (Γ) and edge (π) of the minizone.

For an infinite potential well, only confined transitions (CT) between the m th conduction and n th valence subbands with $m \equiv n$ are allowed ("symmetry-allowed" transitions). This

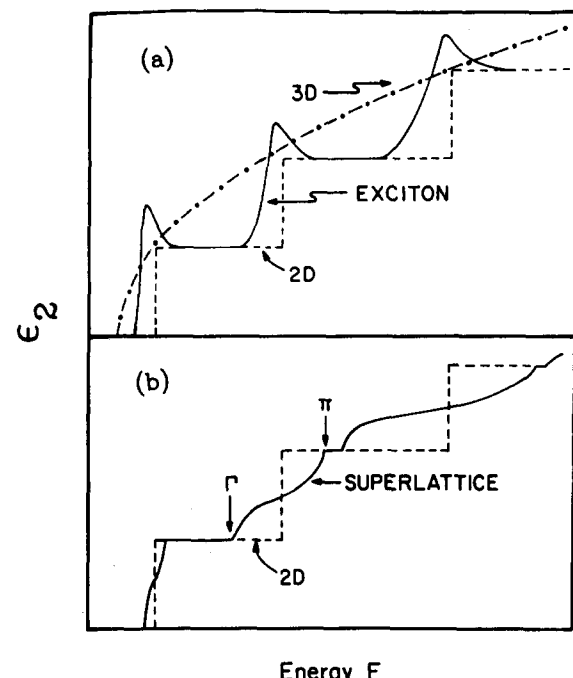


Fig. 30. Schematic representation of ϵ_2 for (a) a three-dimensional (3D) M_0 critical point (dot-dashed line), two-dimensional (2D) joint density of states (dashed line) and exciton (solid line) as well as (b) 2D joint density of states (dashed line) and the influence of superlattice (miniband) formation (solid line) [306].

is a consequence of the nodal structure at the interface and the simple relationship between the number of nodes in the wavefunction and the energy of that state. For finite wells there is no longer a node at the interface and hence “symmetry-forbidden” but “parity-allowed” features with $m=n \pm 2, \pm 4$ etc. may be observed [307], although they are generally weak. The presence of transitions with $m=n \pm 1, \pm 3$ etc. may be induced by wavefunction mixing or electric fields [305,306].

For MQWs and SLs there are also above-barrier resonances, which exhibit miniband effects. The symmetry properties of such unconfined transitions (UT) are more complicated than the CT, since there is no longer a simple relationship between the wavefunction nodes and the energy. The UT no longer make a ladder in energy with respect to the previous one. Additional nodes may appear in the barrier, and hence the parities of the states (with respect to the centre of the well) no longer alternate.

8.1. Lineshape analysis and modulation mechanisms

Figure 31 shows the PR spectra (dotted lines) of a GaAs/GaAlAs MQW ($L_z=200$ Å) at 6 K, 77 K and 150 K in the region of the 11H and 11L excitonic features [12,14]. The notation $mnH(L)$ denotes transitions from the m th conduction to n th valence subband of heavy (H) or light (L) hole character. In general, this notation will be used unless otherwise noted. The solid and dashed lines show fits to the first derivative of Lorentzian (FDLL) and Gaussian (FDGL) profiles, respectively. At 6 K the fit to the Lorentzian is excellent, except for the small structure below 11H (donor-related). In comparing the Gaussian and Lorentzian fits, both functional forms are good near the transition energies, but they differ most in the wings of the curves. The data of Fig. 31(b) cannot be satisfactorily represented by either profile, but rather by some intermediate form. At 150 K the transformation to a Gaussian dielectric function is nearly complete (Fig. 31(a)).

These results also show why $m=3$ in eqn. (4c), i.e. the 2D critical point, provides a reasonable fit to the room temperature experimental data, although it is not the correct functional form [308]. By using $m=3$ instead of $m=2$ (exciton) in eqn. (4c), one essentially takes another derivative of the Lorentzian. This results in a sharpening of the lineshape and improving the fit in the wings. This mimics the first derivative of the dielectric function with a Gaussian absorption profile.

Huang *et al.* [309] have reported a detailed study of the temperature dependence of the PR spectra of a strained layer $\text{In}_{0.21}\text{Ga}_{0.79}\text{As}/\text{GaAs}$ SQW with $L_z=100$ Å. For this system the strain (and well width) creates a large 11H–11L splitting, so that there is no overlap of these two features. While these authors find that the data for $T \geq 80$ K is best fitted by an FDGL, the low-temperature (10 K) signal can be fitted by either FDLL or FDGL. Qiang *et al.* [310] have found the same result in a similar structure. The authors suggest that the FDGL is more appropriate, since the material in the well is an alloy with statistical potential fluctuations.

Several other investigations have confirmed the first derivative excitonic nature of the EM lineshape of the isolated states of semiconductor microstructures. Theis *et al.* [25] have compared the PR spectra at 77 K from a GaAs/GaAlAs MQW with a first-principles theory in which only the exciton linewidth and value of the built-in field are not determined. A comparison has been made of the PR and TR spectra at 300 K from a GaAs/GaAlAs MQW by Shen *et al.* [311]. For the uncoupled 11H and 11L features the two spectra are identical, indicating the first derivative nature of the PR. Also, both lineshapes were fitted using an FDGL form.

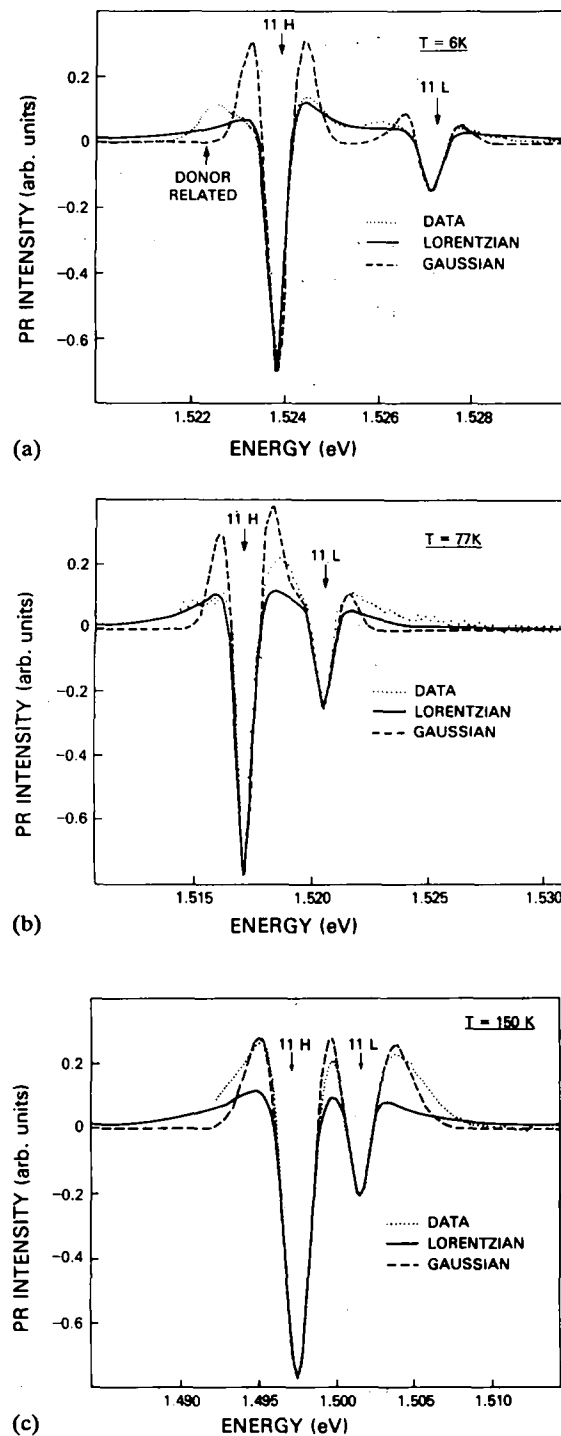


Fig. 31. Experimental PR data (dotted line) at different temperatures in the region of 11H and 11L of a GaAs/GaAlAs MQW. First derivative Lorentzian and Gaussian lineshapes are compared [14].

The influence of miniband dispersion on the EM lineshape has been explored by Shen *et al.* [311,312], Cerdeira *et al.* [313], Niki *et al.* [314] and Coriasso *et al.* [315]. For example, it has been found that the PR and TR spectra are not identical for transitions involving

miniband dispersion [312]. Figure 32 shows the experimental TR and PR (dotted lines) signals at 300 K from the 13H and 22H resonances of a GaAs/GaAlAs MQW. Note that the two spectra are similar for 13H (no miniband formation), but are markedly different for 22H (miniband formation). The solid lines are fits to an FDGL, which produces good agreement with both peaks of the TR but only 13H of the PR. The dashed line is the numerical second derivative of the 22H TR data, which reproduces the PR spectrum of 22H. This provides evidence that the 22H feature of the EM signal is certainly not first derivative and is probably third derivative.

The PR and phototransmittance spectra at 77 K of InGaAs/GaAs strained layer SLs exhibit oscillatory signals at photon energies above the absorption edge [313,314]. The authors interpret this behaviour in terms of FKO's in the SL induced by applied or built-in electric fields and made possible by the large electron miniband dispersion. Coriasso *et al.* [315] have also reported FKO's originating from the band gap of a GaAs/AlAs short-period SL with large miniband dispersion. The observed effect has enabled them to evaluate the reduced effective mass of the miniband in the direction of the growth axis (electric field).

Xu *et al.* [316] have reported a PR study of a GaAs/AlAs gradient period SL. The spectra show oscillations which are attributed to FKO's induced by the quasielectric field in the gradient period SL regions.

The intensity dependence of the PR signal from MQWs has been discussed by Tang [317]. In the low modulation regime it is observed that the amplitude of the signal, $\Delta R/R$, is approximately linear in $P_{\text{a.c.}}$, the intensity of the modulating beam. However, at sufficiently large $P_{\text{a.c.}}$, it is found that $\Delta R/R$ saturates, i.e. becomes almost independent of

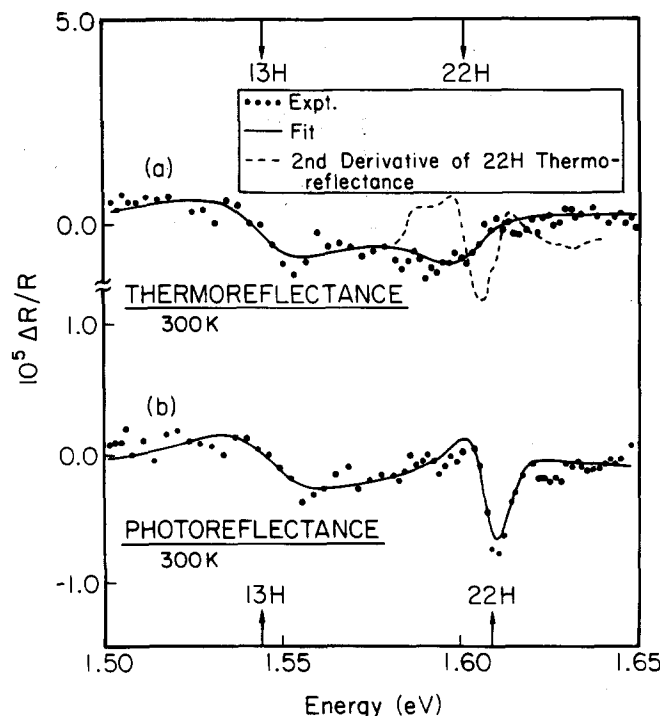


Fig. 32. Experimental (a) TR and (b) PR spectra (dotted lines) at 300 K in the region of 13H and 22H of a GaAs/GaAlAs MQW. The solid lines are fits to an FDGL while the dashed line is the numerical second derivative of the experimental TR data for the 22H feature [312].

$P_{a.c.}$. Such behaviour is consistent with the photovoltaic interpretation of PR (see eqns. (28) and (32)).

In the above considerations it has been assumed that PR is an EM effect. Theis *et al.* [318] have provided evidence that PR in doped QWs is not due solely to EM, but also may contain extrinsic contributions. Ivchenko *et al.* [319] have observed $\Delta R/R > 10\%$ and they attribute this to the neutralization of barrier impurities under illumination.

8.2. Interference effects

As discussed in Section 3.4, the lineshape of any form of modulation spectroscopy can be profoundly affected by optical interference. This is particularly true for semiconductor microstructures, which consist of a number of multilayers. For example, the excitonic PR spectra of GaAs/GaAlAs MQWs were investigated at 300 K at oblique and near normal incidence with different polarized probe beams using a He-Ne laser as the pump [320]. Figure 33 shows the signals in the region of (a) the 11H and 11L excitonic transitions and (b) the GaAlAs band gap at incident angles (θ_i) of 15°, 60° and 80° for p-polarized probe light. As the incident light was scanned over the Brewster angle ($\sim 74^\circ$), the phase of the lineshapes of both sets of structures has shifted by almost 180°. The PR signal near the Brewster angle, e.g. $\theta_i = 60^\circ$, is considerably larger than the other two measurements, owing to the decreased reflectivity.

8.3. Identification of heavy and light hole transitions

While in the GaAs/GaAlAs system the identification of HH and LH transitions is fairly straightforward by comparison with theory, this may not be the case for other systems. For example, in lattice-mismatched microstructures, the strain may invert the order, i.e. the ground state transition could be 11L instead of 11H. Therefore, additional information is required to distinguish the character of a given resonance. There are three procedures which are quite helpful.

By comparing PZR and wavelength-modulated reflectivity (WMR) Mathieu *et al.* [296] and Allegre *et al.* [304] have been able to identify the character of the HH and LH (out-plane) features in GaAs/GaAlAs and CdTe/CdZnTe microstructures, respectively. For the WMR the ratio of the intensities of HH to LH transitions should be in the ratio of 3:1,

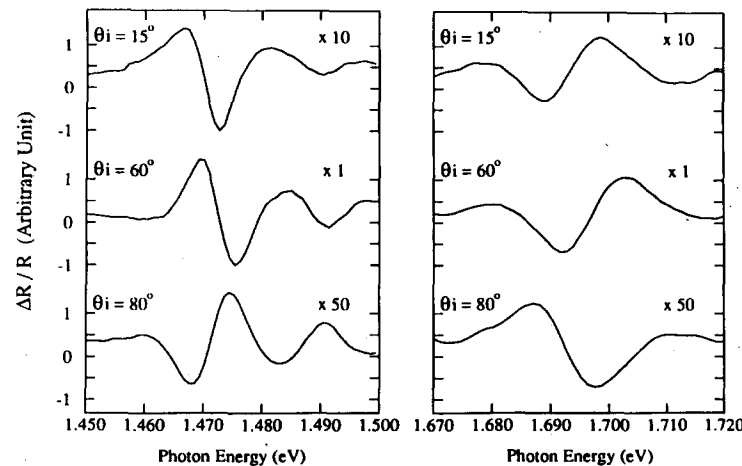


Fig. 33. The PR spectra at 300 K of a GaAs/GaAlAs MQW at incident angles θ_i of 15°, 60° and 80° for (a) 11H and 11L of the MQW and (b) E_0 of GaAlAs [320].

owing to matrix element effects. However, for the biaxial stress produced by PZR the LH valence band undergoes a shift that is about a factor of two larger than the HH edge, as discussed in Section 7. This enhances LH transitions to such an extent as to nearly compensate for the 3:1 difference in matrix elements. Therefore the relative intensities of the HH and LH features are different in PZR as compared to WMR (or PR/ER).

As will be discussed in Section 8.8.4, static uniaxial stress also can be used to differentiate between HH and LH features, based on the different strain dependence mentioned above.

In systems such as InGaAs/GaAs, in which the band gap of the material in the well is smaller than that of the substrate semiconductor, it is possible to perform measurements in the total internal reflection (TIR) mode to identify HH and LH features. This technique involves polarization selection rules that are different for the incident photon polarized along the well (growth) direction and perpendicular to it. For the former, only LH transitions are allowed, while for the latter both types of feature can be seen [321]. This will be discussed further in Section 8.5.2.

Armelles *et al.* [322] have compared PLE and piezomodulated PLE in order to determine the symmetry of the electronic states. The observed relative intensity of the LH and HH transitions from a GaAs/GaAlAs SQW was found to be different in the former case in relation to the latter.

8.4. Topographical scans

Using PR at room temperature, Parayanthal *et al.* [323] have evaluated the topographical variations in quantum level transitions of a GaAs/GaAlAs MQW due to changes in barrier height and quantum well width. The spatial resolution of the measurements was about 100 μm . This measurement was able to detect barrier height changes of several meV and variations in well width as small as 2 Å.

8.5. Compositional SQWs, MQWs and SLs

The following section will discuss modulation experiments on the intrinsic properties of compositional microstructures such as GaAs/GaAlAs, InGaAs/GaAs, CdTe/CdMnTe, SiGe/Si etc. In Section 8.7 the effects of external perturbations, such as electric field, temperature, hydrostatic pressure, uniaxial stress and magnetic fields will be considered.

8.5.1. $\text{GaAs}/\text{Ga}_{1-x}\text{Al}_x\text{As}$ system

A considerable number of modulation experiments have been performed on this lattice-matched heterostructure configuration. Most of these works are discussed in several review articles [11–15,59,173,324–327]. Some recent articles of interest include the use of DR₂ [36,37,84] and infrared photomodulation [26,328] to study these microstructures.

With a few exceptions, all of the above studies have been performed on (001)-oriented material with a square well configuration. Shanabrook *et al.* [329] reported PR studies of (111)-oriented MQWs, while El Khalifi *et al.* [330] and Castrillo *et al.* [331] have performed both WMR, PZR, and PR spectroscopies on (113)-oriented SQWs. The electronic states confined in a parabolic well have been observed in PZR by Lee *et al.* [332]. Kopf *et al.* [333] have used EBER to study analogue-graded parabolic and triangular quantum wells of GaAs/GaAlAs. A PR investigation of a GaAs/AlAs gradient period SL has been reported by Xu *et al.* [316].

As an example of the type of information that can be obtained from modulation experiments on this system, Fig. 34 displays the PR spectra (dotted lines) at 300 K from four GaAs/Ga_{0.82}Al_{0.18}As MQWs all having $L_z = 71 \text{ \AA}$, but with different barrier widths ($L_B = 201 \text{ \AA}$, 150 \AA , 99 \AA and 71 \AA) [334]. The arrow at the bottom of the figure is the energy of the direct (E_0) gap of the Ga_{0.82}Al_{0.18}As barrier material, as determined from PR on a thick epilayer. Thus all features above this energy are due to transitions involving unconfined states. The solid lines are fits to an FDGL. The obtained transition energies are indicated by arrows and listed in Table 1. The authors report that above about 1.52 eV, FDLL or TDFF lineshape fits yielded comparable results.

In order to identify the origins of the large number of features in the PR spectra, the authors performed a theoretical calculation of not only the transition energies but also matrix elements (intensity) using an envelope function model. Exciton binding energy corrections were taken into account. Also listed in Table 1 are the results of this calculation. The best overall agreement was found using a conduction band offset parameter Q_c ($= \Delta E_c / (\Delta E_c + \Delta E_v)$) of 0.65 and the indicated values of L_z and L_B . The three features below 1.52 eV are due to 11H(Γ, π), 11L(Γ, π) and 12H(Γ, π) transitions, respectively. The notation (Γ, π) indicates that the states at the minizone centre (Γ) and edge (π) are essentially degenerate, i.e. there is no miniband dispersion because of the relatively large L_B .

The first structure above 1.52 eV, identified as 12H, is fairly sharp for the 71 \AA /201 \AA and 71 \AA /150 \AA materials, but becomes markedly broader for the 71 \AA /99 \AA case and

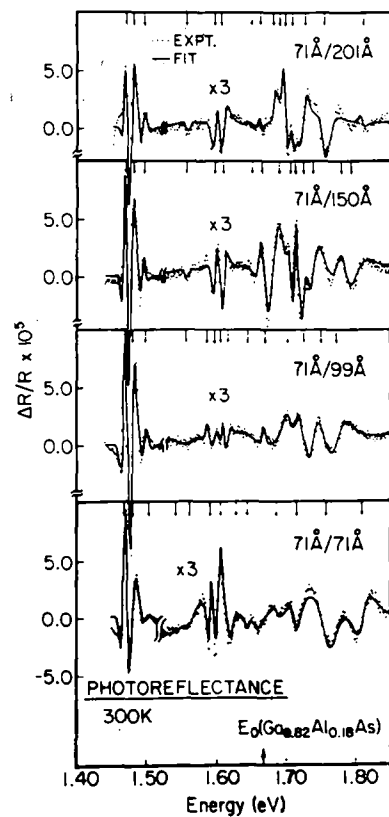


Fig. 34. Photoreflectance spectra at 300 K (dotted lines) of a series of four GaAs/Ga_{0.82}Al_{0.18}As MQWs having the same L_z (71 \AA) but different L_B . The solid lines are fits to an FDGL yielding the energies indicated by arrows [334].

TABLE 1. Experimental and theoretical values of the various confined and unconfined quantum transitions of several GaAs/Ga_{0.82}Al_{0.18}As multiple quantum wells with different barrier layer thicknesses. The unconfined states occur above $E_0(\text{Ga}_0\text{.82}\text{Al}_0\text{.18}\text{As}) = 1.673 \text{ eV}$, as indicated by the dashed line [334]

Transition	$L_z/L_B = 71 \text{ \AA}/201 \text{ \AA}$		$L_z/L_B = 71 \text{ \AA}/150 \text{ \AA}$		$L_z/L_B = 71 \text{ \AA}/99 \text{ \AA}$		$L_z/L_B = 71 \text{ \AA}/71 \text{ \AA}$	
	Expt.	Theory	Expt.	Theory	Expt.	Theory	Expt.	Theory
11H(Γ , π)	1.469	1.467 ^a	1.469	1.467 ^a	1.469	1.466 ^a	1.467	1.465 ^a
11L(Γ , π)	1.479	1.481 ^b	1.480	1.481 ^b	1.479	1.480 ^b	1.479	1.478 ^b
12H(Γ , π)	1.494	1.502 ^c	1.495	1.502 ^c	1.497	1.502 ^c	1.502	1.501 ^c
13H(I)		1.547 ^c		1.546 ^c		1.546 ^c	1.540	1.544 ^c
	1.555		1.555		1.555			
13H(π)		1.548 ^c		1.549 ^c		1.551 ^c	1.560 ^c	1.556 ^c
21L(π)		1.590 ^d		1.589 ^d	1.587	1.586 ^d	1.589	1.584 ^d
	1.595		1.595					
21L(I)		1.591 ^d		1.592 ^d	1.599	1.597 ^d		1.605 ^d
							1.604	
22H(π)		1.609 ^d		1.608 ^d	1.607	1.605 ^d		1.601 ^d
	1.604		1.607					
22H(I)		1.6010 ^d		1.611 ^d	1.618	1.616 ^d	1.626	1.626 ^d
22L(π)	1.644	1.649 ^d	1.647	1.648 ^d	1.638	1.644 ^d	1.642	1.639 ^d
22L(I)	1.658	1.655 ^d	1.662	1.658 ^d	1.666	1.667 ^d	1.685	1.689 ^e
33H(I)	1.680	1.684 ^e	1.682	1.690 ^e	1.704	1.704 ^e	1.718	1.722 ^e
33L(I)	1.689	1.693 ^e	1.705	1.704 ^e	1.728	1.731 ^e	1.759	1.766 ^e
34H(π)	1.696	1.696 ^e	1.713	1.713 ^e	1.748	1.755 ^e	1.809	1.812 ^e
43H(π)		1.712 ^e	1.727	1.734 ^e	1.778	1.776 ^e		
	1.706							
33L(π)		1.712 ^e	1.740	1.741 ^e				
45H(I)	1.728	1.743 ^e	1.779	1.788 ^e				
54H(I)	1.754	1.757 ^e	1.793	1.799 ^e				
56H(π)	1.806	1.809 ^e						

^aExciton binding energy of 8 meV.

^bExciton binding energy of 10 meV.

^cExciton binding energy of 7 meV.

^dExciton binding energy of 6 meV.

^eExciton binding energy of 4.5 meV.

splits into a doublet for the smallest L_B . As L_B decreases, there is increased miniband dispersion, resulting in a well-defined doublet for $L_z = 71 \text{ \AA}$. Note also that 12H has become broader for the narrowest L_B , indicating the onset of miniband dispersion.

The 22L transition, which shows distinct miniband dispersion (see Table 1), is interesting since both Γ and π are confined for the three samples with the widest L_B . For the narrowest barrier material 22L(I) becomes unconfined while 22L(π) is still confined. The energy separation between 22L(I) and 22L(π) is a sensitive function of L_B , even when both are confined, and hence can be used to evaluate this quantity.

The excited states of the heavy and light hole excitons in GaAs/GaAlAs MQWs have been observed using PR at 10 K [335] and PRE at 77 K [22]. Theis *et al.* [335] report the observation of the 1s and 2s states of the 1H and 1L free excitons based on their high resolution (0.06 meV) measurements. For "symmetry-allowed" transitions they used the notation $nH(L)$. The PR data were analysed by comparison with an effective-mass theory based on a modulation of the electric field as the dominant mechanism. Figure 35 is a comparison of PLE data (4 K) and the PR signal (6 K). The PLE spectrum has been

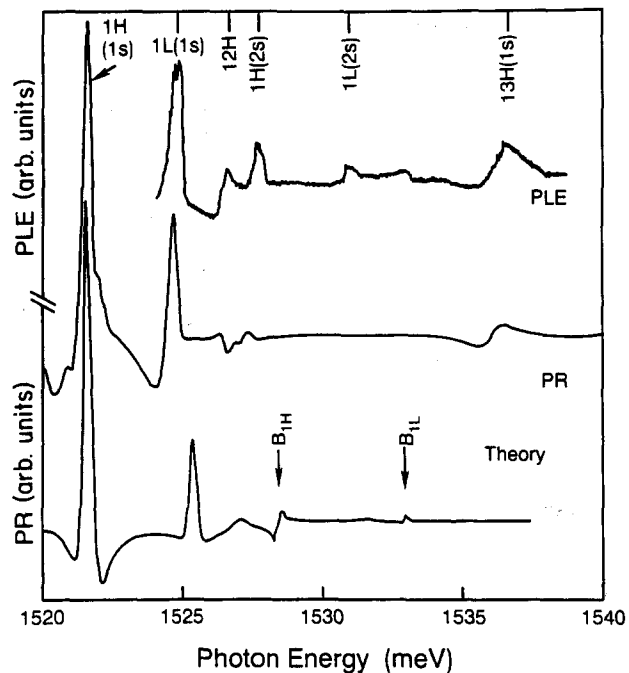


Fig. 35. Comparison of the experimental PLE (upper curve) and PR (center) spectra with a theoretical calculation for a GaAs/GaAlAs MQW [335].

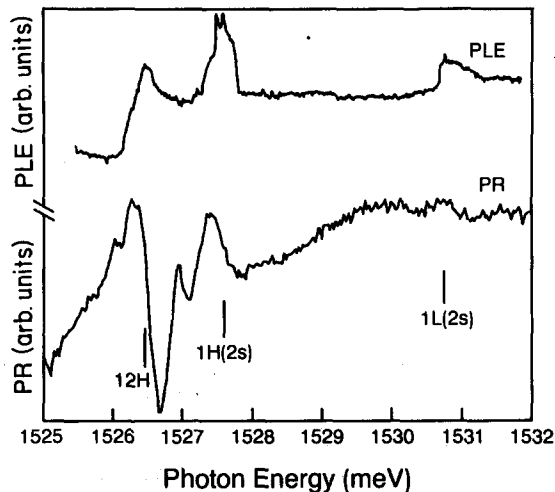


Fig. 36. An expanded view of the PLE (upper) and PR (lower) spectra of Fig. 35, showing the exciton excited states (2s) of the 1H and 1L transitions. Also shown is the "symmetry-forbidden" 12H feature [335].

shifted lower by 0.25 meV to account for the temperature difference. A theoretical fit is also shown in the figure. An expanded view of the PLE (upper) and PR (lower) spectra in the range 1525–1532 meV is presented in Fig. 36. Both the PLE and PR data exhibit well-defined features corresponding to the ground state (1s) and first excited state (2s) of both the 11H and 11L free excitons. Note also in Fig. 35 the presence of the "symmetry-forbidden" 12H and 13H ("parity-allowed") features. In the theoretical curve of Fig. 35 the structures marked B_{1H} and B_{1L} correspond to 2D band-to-band continuum transitions

of 1H and 1L, respectively (see Fig. 30). The authors conclude that the PR spectra show no evidence for such quantum-confined Franz-Keldysh-type features.

The influence of zone folding in short-period $(\text{GaAs})_m/(\text{AlAs})_n$ SLs has been observed by comparing PR and PL [336–340]. In this case, PL occurs from the lowest state, while in general PR measures the density of states and thus the direct gap (neglecting BSR effects). In indirect gap material the PL lines would be from the lowest indirect transition while PR would involve the direct gap and hence would have a feature at higher energies. Figure 37 shows the 300 K PR and PL spectra for a $(\text{GaAs})_5/(\text{AlAs})_5$ SL [338]. The PL data exhibits a peak at a lower energy than the PR transition energy, denoted by the arrow, which was obtained from a lineshape fit. For samples with $m=n \geq 7$ the peaks of the two spectra occur at the same energy. This demonstrates that for $m=n \leq 7$ the gap for these short-period SLs is indirect as a consequence of zone folding.

Above-barrier quasi-bound states in a single quantum well have been observed in PZR [341,342] and PR [343]. These spectra show oscillatory behaviour, which is the result of quantum interference in the continuum state wavefunction [344]. Optical transitions within the unconfined region of quasiperiodic GaAs/GaAlAs SLs have been detected by Tai *et al.* [345]. The quasi-stationary states of a GaAlAs step on GaAs have been observed in PR by Shen *et al.* [346].

Modulation spectroscopy experiments are potentially extremely useful for determining band offset parameters because of the larger number of observed transitions, even at 300 K. For the (001) GaAs/GaAlAs heterointerface the value of $Q_c = 0.65$ was reasonably well established by the time most modulation experiments were performed on this system. Thus these studies were not central to this evaluation, although the results of investigations such as Figs. 2 and 34 could have been employed. However, for the (111) case a PR study at 150 K has been instrumental in gaining information about the band alignment for this crystallographic direction [329]. Three (111) GaAs/GaAlAs MQWs with $L_z = 370 \text{ \AA}$, 145 \AA and 93 \AA were investigated. By comparison of the observed intersubband energies with an envelope function calculation, the authors deduce a value of $Q_c = 0.55$, which is somewhat smaller than that for the (001) interface.

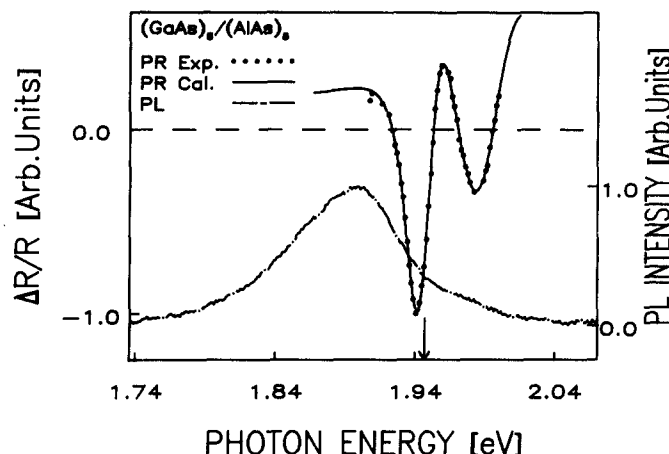


Fig. 37. Room temperature experimental PR (dotted curve) and PL (dot-dashed curve) spectra for a $(\text{GaAs})_5/(\text{AlAs})_5$ SL. The solid curve is a lineshape fit to the PR data yielding the transition energy shown by the arrow [338].

In Sections 8.5.2 and 8.5.3 on the strained layer $\text{In}_x\text{Ga}_{1-x}\text{As}/\text{GaAs}$ and $\text{GaSb}/\text{Ga}_{1-x}\text{Al}_x\text{Sb}$ systems, respectively, it will be shown that modulation studies have played an important role in the determination of the band offset parameter for these heterojunctions.

8.5.2. $\text{In}_x\text{Ga}_{1-x}\text{As}/\text{Ga}_{1-y}\text{Al}_y\text{As}$ system

Strained layer heterostructures allow the use of lattice-mismatched materials without the generation of misfit dislocations. This freedom from the need for precise lattice matching greatly widens the choice of compatible materials and significantly increases the ability to control the electronic and optical properties of such structures.

In such systems, both the strain and quantum confinement play important roles in the determination of the properties of the electron and hole quantum states. For such a strained layer system it is useful to define the conduction band offset parameter as

$$Q_c = \Delta E_c / (\Delta E_c + \Delta E_v^{HH}) \quad (36)$$

where ΔE_v^{HH} is the heavy hole valence band discontinuity.

When grown on a GaAs (AlAs) buffer the $\text{In}_x\text{Ga}_{1-x}\text{As}$ layers sustain a biaxial in-plane compression and a corresponding extension (tensile strain) along the growth direction. The strain considerably alters the band structures of the $\text{In}_x\text{Ga}_{1-x}\text{As}$ material [194]. The band gap is shifted to higher energies by the compressive hydrostatic component of the strain, while the tensile (001) uniaxial strain splits the HH-LH degeneracy at the BZ centre so that the HH (out-plane) valence band is the ground state.

In such a system the relative positions of the bands in the $\text{In}_x\text{Ga}_{1-x}\text{As}$ wells and the GaAs barriers can lead to two possible configurations of the quantum potential, as illustrated schematically in Fig. 38. For $Q_c \leq 0.5$ (left-hand side) the electrons and both heavy and light holes are confined in the $\text{In}_x\text{Ga}_{1-x}\text{As}$ wells, i.e. we have a type I configuration for both types of hole. However, for $Q_c \geq 0.5$ the configuration on the right-hand side is appropriate. The electrons and heavy holes are in the $\text{In}_x\text{Ga}_{1-x}\text{As}$ region (type I) while the light holes are in the GaAs region (type II).

There has been extensive work on the $\text{In}_x\text{Ga}_{1-x}\text{As}/\text{GaAs}$ system using various modulation methods, such as PR [309, 310, 313, 320, 347–360], EBER [361] and DR₂ [32–34]. Quantum wells of GaAlAs/InGaAs/GaAs have been studied using EBER [362]. All the above investigations involved material grown on (001) GaAs buffer/substrates, with the exception of Reddy *et al.* [347], who employed (001) Si substrates with a GaAs buffer.

Figures 39(a) and 39(b) show the PR spectra at 300 K for $\text{In}_x\text{Ga}_{1-x}\text{As}/\text{GaAs}$ MQWs having (a) $L_z = 42 \text{ \AA}$, $L_B = 200 \text{ \AA}$ and $x = 0.256$ and (b) $L_z = 81 \text{ \AA}$, $L_B = 200 \text{ \AA}$ and $x = 0.236$ [348]. Both signals are extremely rich. The transition energies, as obtained from a

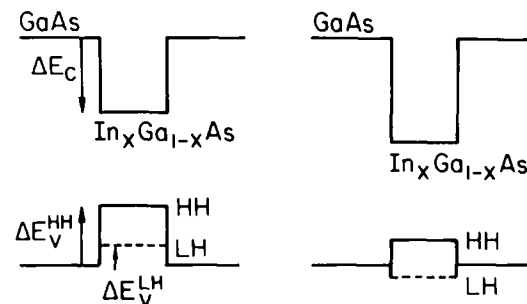


Fig. 38. Possible energy band configurations in a strained layer $\text{In}_x\text{Ga}_{1-x}\text{As}/\text{GaAs}$ quantum well. The left-hand side occurs for $Q_c \leq 0.5$ while the right-hand alignment is for $Q_c \geq 0.5$ [349].

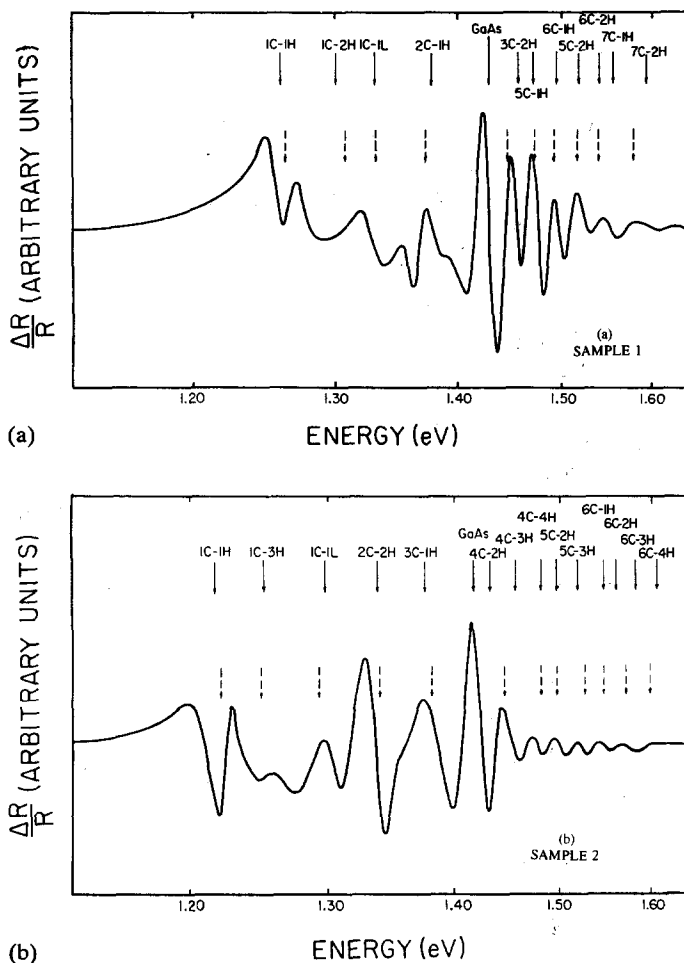


Fig. 39. Experimental PR spectra for two $\text{In}_x\text{Ga}_{1-x}/\text{GaAs}$ MQWs at 300 K. The dashed arrows give the energies derived from a lineshape fit, while the solid arrows are the energies of the indicated excitonic transitions obtained from theory [348].

lineshape fit, are denoted by dashed arrows. The feature marked ‘GaAs’ corresponds to the direct gap of GaAs and originates in the buffer/substrate. Obviously the features with energies higher than the GaAs band gap should be associated with subbands having energies higher than the barrier, i.e. unconfined states.

In order to identify the origins of the larger number of features in the PR spectra of Figs. 39(a) and 39(b), the authors performed a theoretical calculation, including strain, based on the envelope function approximation for both CT and UT. Appropriate exciton binding energies for the CT were taken into account. The energies of the UT were determined from a calculation of the transmission coefficient. The solid arrows indicate the transition energies obtained from the theoretical calculation using the above values of L_z , L_B and x with $Q_c = 0.70$. These authors use the notation $mC-nH(L)$ to denote the conduction (C) to heavy (H) and light (L) hole transitions. Overall, there is very good agreement. The authors did not state whether the UT transitions originated at the Γ or π points of the minizone.

The features with energies above the GaAs barrier should involve unconfined electron subbands. However, it was found that transitions with energies below the GaAs barrier can

also involve unconfined subbands. The feature 2C-1H at energy 1.371 eV in Fig. 39(a) is one of the transitions associated with the second conduction subband, which is unconfined. Only the first conduction subband is confined in this sample.

It was observed in this study that narrow wells lead to stronger UT, and such transitions are very weak when the well width is wider than 200 Å. The mole fraction x has only a little effect on the intensity of such PR signals. Very strong signals have been observed in the material with a well width $L_z = 42$ Å and $x = 0.256$. A monotonic decrease of unconfined transitions is seen as the quantum well thickness is increased from $L_z = 42$ to 200 Å. This can be explained qualitatively as follows: first, the wavefunction of unconfined conduction bands must be located around the well region. For a narrow well, the overlap between the wavefunctions of conduction and hole states must be large, causing a strong PR signal. Second, the PR signal is proportional to k_z , the cutoff of the Brillouin zone in the z -direction. $k_z \approx 1/L_z$ is larger for an MQW with a narrow well width, and so is the PR signal. Third, when the well width becomes wider, the signal from the different heavy hole subbands and the same unconfined conduction states overlap. This introduces extra cancellation between the neighbouring signals.

Ksendzov *et al.* [321] have recently reported PR measurements of (001) $\text{In}_x\text{Ga}_{1-x}\text{As}/\text{GaAs}$ SQWs ($x = 0.11$ and 0.19). They were able to study the polarization dependence of the PR spectra at 300 K by performing measurements not only in the conventional configuration (light incident along the growth axis) but also by using a TIR mode. As discussed in Section 8.3, this TIR study allowed them to make an unambiguous identification of the HH and LH states which is an important factor in determining Q_c . As pointed out previously, the HH-LH distinction in the GaAs/GaAlAs system was made by comparing PZR and WMR (or PR/ER).

The dotted line in Fig. 40(a) shows the experimental PR spectrum in the conventional configuration at 300 K from the $\text{In}_{0.19}\text{Ga}_{0.81}\text{As}/\text{GaAs}$ sample ($L_z = 107$ Å). In the conventional configuration the k vectors of the pump and probe beams are along the (001) growth direction and hence only xy -polarization is allowed. The solid line is a least-squares fit to a FDGL. The obtained values of the intersubband energies (A-D) are designated by arrows at the top of the figure. The dotted lines in Figs. 40(b) and 40(c) are the PR spectra in the TIR mode for z - and xy -polarizations, respectively. Peak A is present in the xy -polarization spectrum, but is very weak in the z -polarization data. Structures B and D are seen for both polarization modes. For the xy configuration, both heavy and light hole transitions are allowed, while for the z -polarization state only light hole transitions should be observed. Thus A is identified as 11H, whereas B and D originate from LH states. No identification of the structure C was done on a similar basis since it could not be observed in TIR due to the low signal-to-noise ratio.

To complete the identification of the PR features, a theoretical calculation based on the envelope function approximation, including strain and exciton effects, was performed. Figure 41 shows a comparison of the experimental results with the theoretical calculation for different values of Q_c . The dotted vertical lines are the experimental energies of A-D, the shaded regions being the error bars. The solid lines indicate the calculated results for the various $mn\text{H(L)}$ transitions as a function of Q_c (including exciton binding energy). The best fit is obtained for $Q_c = 0.67 \pm 0.07$. Note that the 11H-11L separation is very sensitive to Q_c for $Q_c \geq 0.5$ (type II for the light holes). For smaller values of Q_c , the light holes are type I and hence the 11H-11L separation is not so dependent on Q_c . Similar measurements were made for the $x = 0.11$ sample, yielding $Q_c = 0.45 \pm 0.07$.

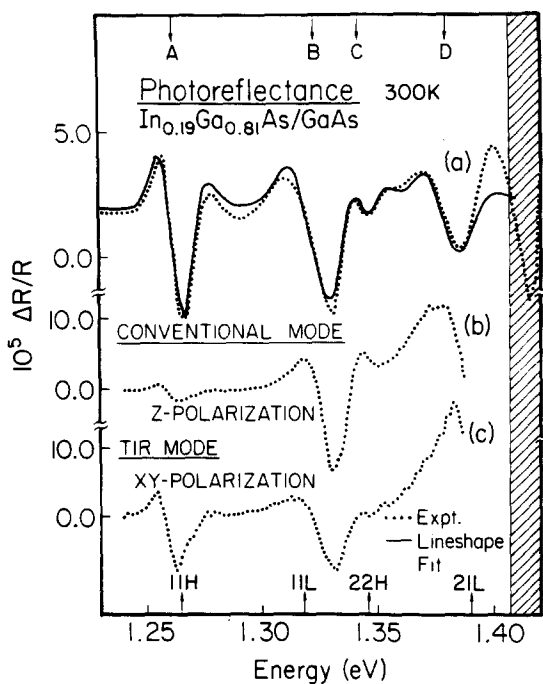


Fig. 40. Photoreflectance spectra (dotted lines) at 300 K from an $\text{In}_{0.19}\text{Ga}_{0.81}\text{As}/\text{GaAs}$ SQW (a) in the conventional mode, (b) in the TIR mode for z -polarization and (c) in the TIR mode for xy -polarization. The solid line is a fit to an FDGL yielding the energies indicated by arrows [321].

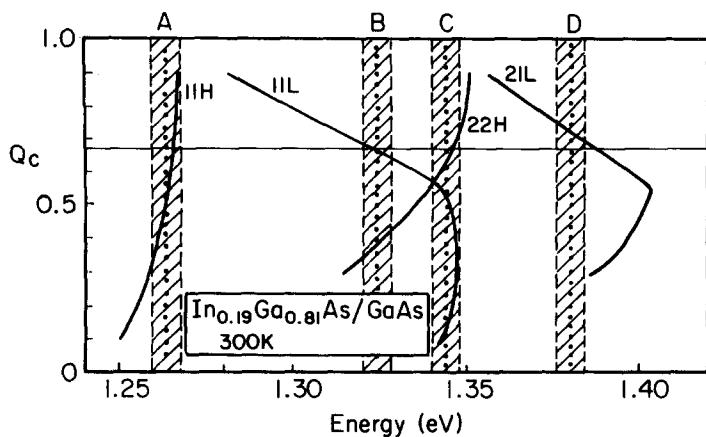


Fig. 41. Theoretical energies of various $mnH(L)$ transitions (solid lines) as a function of Q_c (eqn. (36)) for an $\text{In}_{0.19}\text{Ga}_{0.81}\text{As}/\text{GaAs}$ SQW. The dotted lines are the experimental values including error bars [321].

The study of Ksendzov *et al.* [321] on two InGaAs/GaAs SQWs with different In composition showed a trend in Q_c consistent with the suggestion of Joyce *et al.* [363]. By taking values of Q_c from a large number of experiments they find that the band alignment shows a monotonic dependence on the In concentration with $Q_c \sim 0.4$ for $x \leq 0.1$ and $Q_c \sim 0.8$ for $x \geq 0.2$. The theoretical calculation of Jogai [364] is in agreement with this trend.

Some very interesting properties of monolayer and submonolayer InAs/GaAs quantum wells have been observed by several groups using PR, PL and PLE [354,355,357,365]. These

measurements provide evidence for the strong localization of the HH and LH excitons, even in submonolayer wide InAs quantum wells.

A strong indication of exciton formation in the ultra-thin InAs layer comes from a comparison of the PL, PLE and PR spectra shown in Fig. 42 [355]. The PLE data exhibit distinct exciton absorption peaks localized at 1.473 eV (E_{11h}) and at 1.496 eV (E_{11l}) in addition to the 1s and 2s states of the bulk GaAs exciton peak at 1.515 eV (E_x^{1s}) and 1.5185 eV (E_x^{2s}), respectively. The E_{11h} peak lies at the energy of the B band observed in the PL spectra (bottom traces in Fig. 42). In spite of the ultra-thin well width and of the high strain in the InAs lattice plane, a Stokes shift between the PL and PLE was not observed.

The PR spectrum (PR line in Fig. 42) exhibits two sharp resonances corresponding to the E_{11h} and E_{11l} ones observed in the PL and PLE spectra and a weak additional resonance around 1.502 eV. Analogously, the authors observed a reflectivity resonance at energy coincident with the GaAs exciton peak in the PLE curve. The excitonic nature of the E_{11h} and E_{11l} transitions is confirmed by the lineshape analysis of the PR spectrum shown in Fig. 42 (dashed line). The main features of the experimental spectrum can only be fitted by assuming an excitonic resonance characterized by a FDLL at low temperature and taking into account the exciton eigenenergies deduced from the peaks of the PLE spectrum. They conclude that the E_{11h} and the E_{11l} PLE peaks can be attributed to the heavy and light hole excitons formed in the submonolayer InAs well.

The observed temperature dependence of the PR spectra supports this assignment. The E_{11h} and E_{11l} resonances red-shift by about 85 meV in the temperature range 5–300 K, in agreement with the subband shift of the InAs well, while the bulk GaAs exciton

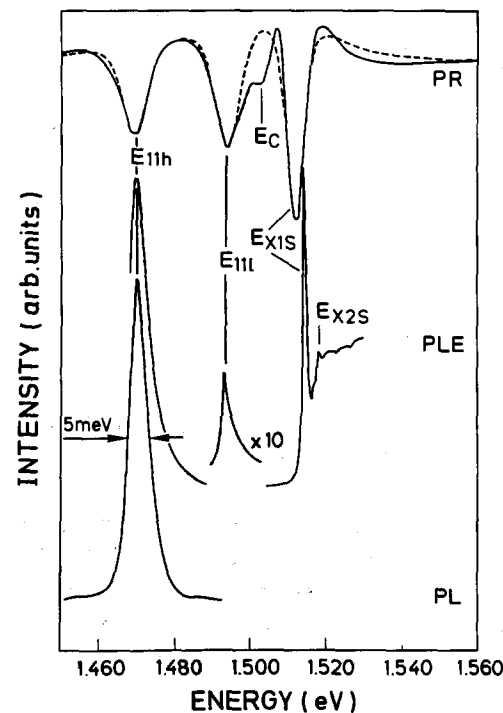


Fig. 42. Experimental PL, PLE and PR spectra (solid lines) at 4.2 K from an ultra-thin InAs/GaAs MQW. The dashed line superimposed on the PR data is a lineshape fit [355].

resonance red-shifts by about 100 meV, as expected for the temperature dependence of the GaAs band gap. It should be mentioned that the weak resonance around 1.502 eV is related to transitions involving states quasiresonant to the GaAs valence band continuum, as confirmed by systematic PLE measurements as a function of the detection wavelength, and it has not been included in the calculation of the PR lineshape. The above results provide clear evidence of exciton formation in submonolayer InAs quantum wells. The authors discuss the ramifications of this observation.

The properties of an $\text{In}_{0.17}\text{Ga}_{0.13}\text{As}/\text{Ga}_{0.7}\text{Al}_{0.3}\text{As}$ MQW have been investigated using Schottky barrier ER [366]. A value of $Q_c=0.61$ for this system has been deduced from the measurements. The authors also have observed some anomalous features. The temperature and barrier thickness of these structures suggest that they might possibly arise from electronic coupling between the quantum well states and states caused by defects or impurities.

Using wavelength-modulated reflectivity at 2 K, Gil *et al.* [367] have observed the quantum well ground state and excited states of several InGaAs/GaAlAs SQWs. To account for the dependence of these energies on In and Al concentration it was necessary to include the strain-induced coupling between the LH and spin-orbit split valence bands.

Rodriguez *et al.* [368] have studied InAs/AlAs SLs using PR and spectral ellipsometry in the E_1 , $E_1 + \Delta_1$ region. Although they have observed the influence of strain on the transition energies they find no evidence for quantum confinement effects as reported by Mendez *et al.* [6] and Erman *et al.* [7] for these features in GaAs/GaAlAs MQWs.

All the above studies on InGaAs/GaAs system have been performed on (001)-oriented material. Shen *et al.* [254,255] have recently reported a PR study on a [111]B grown InGaAs/GaAs system. A modified UN⁺ structure with a 100 Å undoped $\text{In}_{0.15}\text{Ga}_{0.85}\text{As}$ quantum well inserted in the middle of the undoped GaAs layer is used in their study. This structure has a large internal field generated by the piezoelectric effect. Therefore no spectral feature from the InGaAs quantum well is observed. However, by probing the electric field in the adjacent undoped GaAs layer, they are able to determine the piezoelectric field in the InGaAs quantum well. The measured value is in good agreement with the theoretical prediction.

8.5.3. $\text{GaSb}/\text{Ga}_{1-x}\text{Al}_x\text{Sb}$ system

In contrast to the InGaAs/GaAs heterostructures, in the strained layer $\text{GaSb}/\text{Ga}_{1-x}\text{Al}_x\text{Sb}$ system the valence ground state can be either HH or LH (out-plane), depending on the relation between the strain and quantum confinement. The GaSb wells are under a biaxial tension which produces a uniaxial compression along the growth direction. This effect decreases the gap and leaves LH as the ground state. On the other hand, the quantum confinement acts in the opposite direction.

Electroreflectance [369], PR [370] and TR [324] have been used to study this microstructure. The PR spectrum (dotted line) at 77 K of a (001) GaSb/AlSb MQW with $L_z=260$ Å and $L_B=280$ Å is displayed in Fig. 43 [370]. Because of the large confinement energy in this system there are a large number of CT and hence the spectrum is very rich. Measurements were also made on a sample with $L_z=130$ Å and $L_B=140$ Å. The solid line is a fit to an FDGL. The obtained values of the transition energies are indicated by arrows. Note that the lowest-lying feature is about a factor of three smaller than the second peak. This is opposite to results for the GaAs/GaAlAs system (see Fig. 31) for which the heavy hole is the ground state, i.e. 11H lies below 11L. Thus, for the GaSb/AlSb sample of Fig.

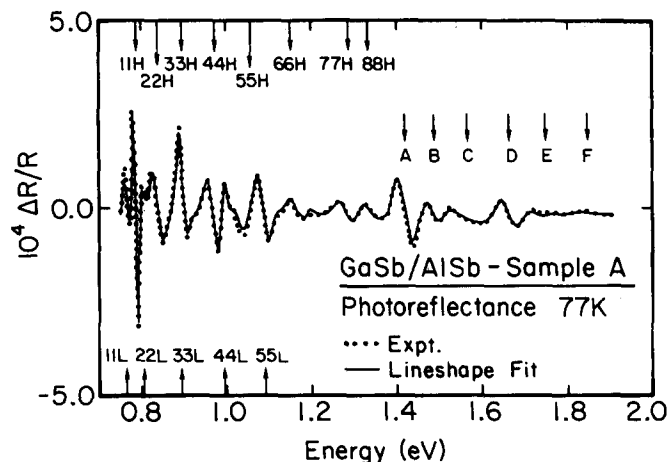


Fig. 43. Photoreflectance spectrum (dotted line) at 77 K of a GaSb/AlSb MQW. The solid line is a fit to an FDGL yielding the energies indicated by arrows [370].

43 there is a strain-induced mass reversal so that 11L is the ground state. The 11L–11H splitting is a measure of the strain distribution.

The origins of the various features in Fig. 43 below 1.4 eV were identified by comparison with an envelope function calculation, including strain and exciton binding effects. The best overall fit was obtained using $Q_c = 0.85 \pm 0.08$ (before strain). Above 1.4 eV (i.e. features A–F) the excellent agreement between experiment and theory could not be maintained. The authors discuss possible explanations, including Γ -X interactions due to the proximity of the X indirect conduction band of the AlSb.

8.5.4. Other III-V systems

Various modulation methods have been used to investigate QWs and SLs of InGaAs/InP [371,372], GaInP(ordered)/GaAs [373], GaInP/GaAs [374], GaP/InP [375], InGaAsP/InP [376], InAsP/InP [377], InGaAs/InAlAs [378] and GaAsSb/GaAs [379]. Ehrenfreund *et al.* [25] have reported infrared photomodulated studies on InGaAs/InP MQWs. Kopf *et al.* [333] have performed an EBER study of GaInAs/AlInAs parabolic and triangular quantum wells lattice matched to InP and they found the conduction band offset $Q_c = 0.65$.

8.5.5. II-VI systems

Quantum structures of $Cd_{1-x}Mn_xTe/CdTe$ [324], $Cd_{1-x}Zn_xTe/CdTe$ [296,304], $Cd_{1-x}Mn_xTe/Cd_{1-y}Mn_yTe$ [324] have been studied using PZR at low temperatures. Important information about band offset parameters has been obtained. The reader also is referred to ref. 325.

8.5.6. GeSi/Si and GeSi/Ge systems

One of the most interesting applications of modulation spectroscopy in semiconductor microstructures has been the work on short-period strained (001) GeSi SLs fabricated on substrates of Si [380–382], Ge [383–387] and GeSi [388,389]. Also, Pearsall *et al.* [390] reported ER measurements on SiGe MQWs on Si substrates. Many of the above works have been reviewed by Pearsall [391,392].

There has been considerable interest in short-period SLs of this technologically important system, owing to the possibility of enhancing both the optical absorption coefficient near the band gap and the radiative recombination rates. The most intriguing question is that

of band gap conversion from an indirect gap (e.g. Si) to a quasidirect gap due to structurally induced zone folding along the SL growth direction.

The first evidence for such structurally induced modifications of the band structure were reported by Pearsall *et al.* [380,381] using Schottky barrier ER. Figure 44 shows the ER spectra of an ordered $\text{Ge}_4\text{Si}_4/\text{Si}$ short-period SL [380]. For this configuration, the Ge part of the SL is under a two-dimensional compressive strain resulting in a tensile uniaxial strain along the (001) SL growth direction. The optical features denoted as 8 (0.76 eV), 7 (1.25 eV) and 6 (2.31 eV) are characteristic of neither the cubic Si nor the strained Ge and have been ascribed to quasidirect transitions induced by zone folding effects. Similar features also have been reported in ER and PR by Asami *et al.* [381] on $\text{Ge}_4\text{Si}_4/\text{Si}$, $\text{Ge}_3\text{Si}_5/\text{Si}$ and $\text{Ge}_2\text{Si}_6/\text{Si}$. The possible role of interference effects in this spectral region has been discussed by Pearsall *et al.* [391,392] and Gell *et al.* [384].

For GeSi short-period SLs fabricated on (001) Ge substrates, the Si is under a two-dimensional tensile strain with the concomitant uniaxial compression along the growth direction. Under these conditions, the Si conduction band lies along the SL axis and it will be mixed by the SL potential with zone-centre states, with the possibility that this SL might be quasidirect. Pearsall *et al.* [383] have reported Schottky barrier ER measurements at 90 K on $\text{Ge}_6\text{Si}_4/\text{Ge}$ and $\text{Ge}_7\text{Si}_3/\text{Ge}$ samples. For comparison purposes, bulk Ge also was evaluated. These results are shown in Fig. 45. All three spectra show distinct features at 0.88 eV and 1.18 eV, corresponding to E_0 and $E_0 + \Delta_0$ for Ge. For the two SLs these peaks originate in the Ge buffer/substrate. The fine structure in the Ge E_0 transition, which is apparent in all three spectra, is the "lineshape rotation" interference effect discussed in Section 4.1. The SL spectra are more complex than the Ge signal, exhibiting additional structures near 0.94 eV and 1.24 eV, as evaluated from a TDFF fit to the data. Pearsall *et al.* have identified these peaks as due to transitions involving quasidirect zone-folded states [383].

The data of Fig. 45 are complicated by (a) the proximity of E_0 (0.88 eV) and $E_0 + \Delta_0$ (1.18 eV) of the Ge substrate/buffer to the zone-folded states and (b) the fact that the Ge substrate ER features exhibit FKO's. Subsequent studies, in which an external d.c. electric field was applied to these samples, revealed a very complex structure which has not been fully interpreted [392] (see Section 8.8.1).

Piezoreflectance [385,387] and PR [387] at 77 K have been performed on short-period GeSi/Ge SLs, including two samples with the same specifications as Pearsall *et al.* [383].

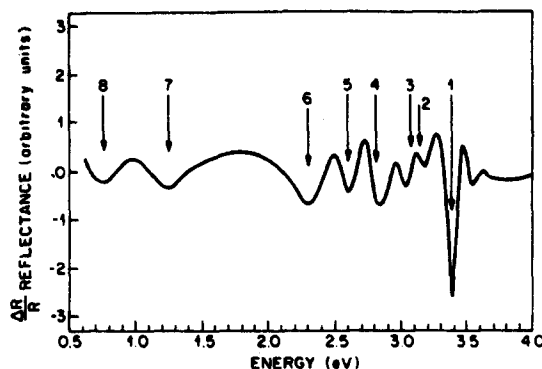


Fig. 44. Electroreflectance spectrum of a $\text{Ge}_4\text{Si}_4/\text{Si}$ short-period SL. New transitions are resolved at 0.76(8), 1.25(7) and 2.31(6) eV [379].

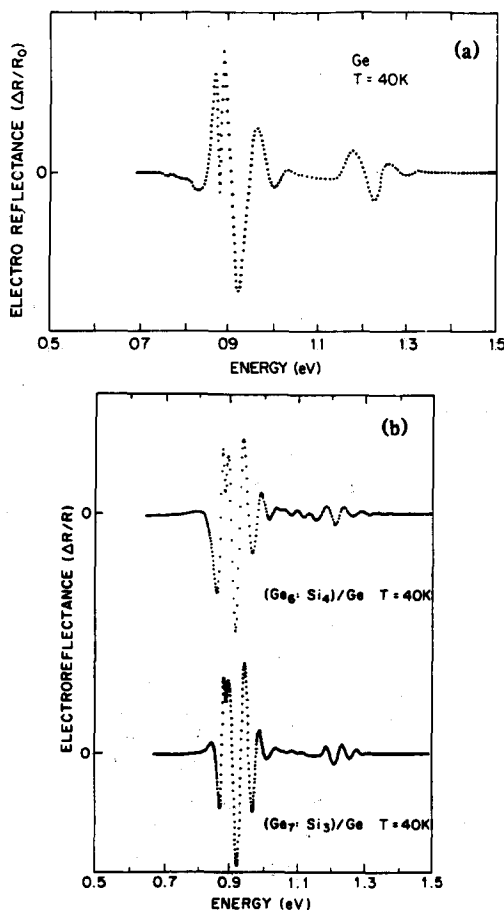


Fig. 45. Electroreflectance spectra at 40 K from (a) bulk Ge, (b) $\text{Ge}_6\text{Si}_4/\text{Ge}$ SL and (c) $\text{Ge}_7\text{Si}_3/\text{Ge}$ SL [383].

The PR spectra are very similar to Fig. 45, exhibiting complex structure near E_0 and $E_0 + \Delta_0$ of Ge. The observed PZR features are clearly due to quantum-confined transitions in the Ge spacer regions, not pseudodirect transitions in the short-period GeSi portion of the samples. The PR spectra, however, apparently exhibited no signal from the Ge spacer regions. This point is still under investigation.

Dafesh *et al.* [388,389] have reported PR at 87 K on a short-period strain-symmetrized (001) $\text{Si}_8\text{Ge}_{32}/\text{Ge}_{0.8}\text{Si}_{0.2}/\text{Si}$ structure. These authors have observed a rich spectrum with 15 features between 1.1 and 2.7 eV. The lineshape was fit to the TDFF. They assigned four of these features as being due to transitions in the alloy buffer, but conclude that the remainder originate from the synthesis of a new superlattice material. Calculated transition energies are found to agree well with experiment for most of the remaining features.

8.6. Doping superlattices

Semiconductors microstructures with quantized 2D electron and hole subbands can also be formed by (a) a periodic doping profile of n- and p-doped layers, possibly separated by undoped (intrinsic, i) regions (nipi structures) or (b) a combination of alternating composition plus doping (hetero-nipi structures) [306]. These configurations exhibit properties not found in either bulk crystals or compositional SLs. These nipi structures have an “indirect gap” in real space, long electron–hole recombination lifetimes because of the spatial separation

of the carriers and a 2D subband structure that can be tailored independently for each carrier type.

The first modulation spectroscopy experiment on nipi material was reported by Gal *et al.* on InP doping SLs [393]. Subsequently, work on GaAs nipi samples was performed by Shen *et al.* [394], Tang *et al.* [395], Linder *et al.* [396] and Alperovich *et al.* [397,398]. The latter investigation involved material fabricated by δ -doping. Studies of GaAs/GaAlAs heteronipis have been published by Tang *et al.* [399] and Kiel *et al.* [400].

In a number of the above samples PR features were observed which were interpreted in terms of transitions between valence and electron subbands (including miniband formation) in the p- and n-layers, respectively [394,395,399]. Gal *et al.* [393] considered only quantization of the electron subbands. However, because of the large number of possible allowed interband transitions it is difficult to make a unique assignment of the experimental data in nipi structures [394], in contrast to compositional MQWs and SLs (see, for example, Fig. 34 and Table 1).

Franz-Keldysh oscillations associated with the large built-in fields in these structures have been reported in refs. 394, 396, 397 and 400. The dependence of the signals on temperature, chopping frequency, light levels and applied electric field have been investigated. An increase in chopping frequency is found to decrease the amplitude of the PR signal intensity, making it possible to evaluate carrier recombination times similar to the analysis of Section 4.5. The effect of d.c. background illumination was to flatten the bands and hence reduce the built-in fields and carrier lifetime.

8.7. Two-dimensional electron gas (2DEG)

A 2DEG can be formed in modulation-doped heterojunctions (MDHJ) (e.g. GaAs/GaAlAs), modulation-doped quantum wells (MDQW) (e.g. GaAlAs/GaAs/GaAlAs, pseudomorphic GaAlAs/InGaAs/GaAs) or δ -doped material. Although modulation studies of the 2DEG in GaAlAs/GaAs MDHJ and δ -doped GaAs have been the subject of considerable controversy, conclusive evidence for the properties of the 2DEG in the GaAlAs/InGaAs/GaAs system has recently been reported [401,402].

In their original PR work, Glembocki *et al.* [9,10] reported oscillatory features above the band gap of GaAs in a GaAs/GaAlAs MDHJ. They initially assigned these structures simply to transitions from the GaAs valence band to the quantized levels in the nearly triangular shaped potential at the interface. Snow *et al.* subsequently calculated the absorption profile from such a heterointerface including contributions from the extended valence band states into the first five conduction subband states at the "triangular" interface potential [403]. They assumed that the modulation mechanism was the variation in N_s , the 2DEG density. They reported that the only structure evident in the calculation was due to FKO's arising from structure in the energy dependence of the interband matrix elements. However, they concluded that there was no structure in the absorption edge that could be identified with the subband energies. Their measured ER data were in good agreement with the theoretical calculation, although the PR spectrum appeared quite different and exhibited a marked temperature dependence. Tang performed a similar calculation for both MDHJ and δ -doped structures [404].

Since that time there have been a considerable number of investigations, mostly PR and DPR, on modulation-doped GaAs/GaAlAs heterojunctions [23,75,111,405–413] and δ -doped GaAs [407,414–419]. While there is general agreement that the observed oscillatory features above E_0 of GaAs are FKO's, their origin is a subject of some dispute. This is

because in the GaAlAs/GaAs MDHJ or GaAs δ -doped systems there exist electric fields associated with E_0 of GaAs, not only in the region of the 2DEG, but also in other portions of the sample. This problem can be averted by studying the GaAlAs/InGaAs/GaAs MDQW system, since in this case the 2DEG signature will be associated with the InGaAs section of the sample, which is spectrally separated from the other signatures.

Several authors have presented evidence that the oscillatory structure observed in GaAs/GaAlAs MDHJs or δ -doped GaAs is due not to the properties of the 2DEG (i.e. quantum FKO's as in ref. 107), but are actually FKO's associated with electric fields in other GaAs portions of the structure. For example, consider δ -doped (n-type) GaAs such that the impurity sheet is a distance D from the front surface. At the bottom of the "V" shaped potential of the δ -doping the Fermi level lies somewhat above the conduction band edge, while at the surface E_F is pinned about midgap (≈ 0.7 V) due to surface states. This situation is illustrated schematically in the 300 K panel for Fig. 46 [417]. Therefore, a uniform electric field of about $0.7V/D$ (where D is the distance from the front surface) would exist in the region between the front surface and the impurity layer. Note that this configuration is quite similar to the UN⁺/UP⁺ structures discussed in Sections 3.1.2 and 5.1. Similarly, for an MDHJ the Fermi level is just above the conduction band edge at the heterointerface. However, at the buffer/substrate interface there could be trapped charge which pins the Fermi level at some value between midgap and the valence band edge. For example, the presence of carbon (acceptor) at this interface would lead to the latter situation.

Pan *et al.* have measured the PR spectra from GaAs/GaAlAs MDHJ samples (a) after sequential etching steps (in phosphoric acid) and (b) as a function of external electric field [409]. They conclude that the oscillations above the GaAs band gap are FKO's originating from the large surface electric field and are not directly associated with the properties of the 2DEG. Bernussi *et al.* [407] and Novellino *et al.* [412] have reached a similar conclusion, based on studies of GaAs/GaAlAs MDHJ and GaAs δ -doped samples as functions of temperature, illumination and material parameters. For example, the electric field deduced

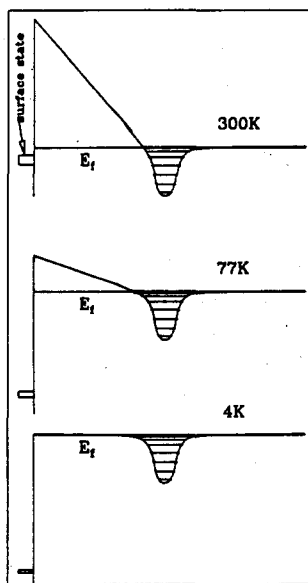


Fig. 46. A schematic representation of the conduction band structure and the surface states of δ -doped GaAs material at 300, 77 and 4 K under modulated photo-excitation conditions [417].

from the FKO_s in δ -doped material with different cap layer thicknesses (D) scales approximately as $0.7V/D$, as discussed previously. Also, the temperature and illumination dependencies of the electric fields are similar to those seen for UN⁺(UP⁺) structures (see Fig. 22). The observed electric fields, as deduced from the FKO_s, go to zero as the temperature is decreased. Such behaviour can be explained by a surface photovoltaic effect (see eqn. 28(a)), as illustrated schematically in the 77 K and 4 K panels of Fig. 46, but is not accounted for on the basis of interband transitions involving the 2DEG [407,412].

However, other workers contend that the PR signals from GaAs/GaAlAs MHHJs and δ -doped GaAs do contain information about the 2DEG. Using different pump wavelengths, Tang [404] has found a first derivative-like feature in a modulation-doped heterojunction. The author believes the dominant modulation is electron filling in the first quantized subband in the 2DEG system. Using DPR, Sydor and his group have investigated MDHJ and δ -doped samples [23,111,411,416,420–422]. They report that this approach eliminates signals from surface field effects and hence can be used to extract the PR signature from the triangular potential well region which contains the 2DEG. The solid line in Fig. 47 shows the PR spectrum at 300 K from a highly photoluminescent GaAs/GaAlAs MDHJ whose cap has been etched off [411]. The level of the laser-induced PL is shown by the labelled line. There are small oscillations on top of the GaAs band gap signal around 1.45 eV. The broken and dash-dot lines display the DPR spectra using 441 nm/632 nm and 476 nm/632 nm matched pump beams, respectively. The dot-dashed trace exhibits no evidence of structure from the GaAs band gap, but exhibits two well-defined peaks labelled E_0 (not to be confused

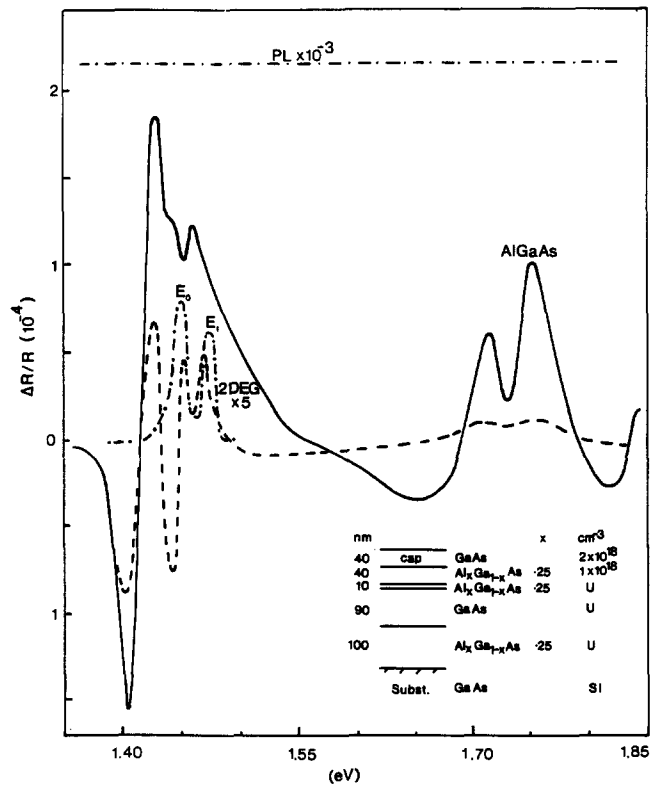


Fig. 47. Photoreflectance (solid line) and DPR (dashed and dot-dashed lines) spectra from a GaAs/GaAlAs MDHJ sample. The dashed and dot-dashed traces correspond to pump wavelengths of 441/633 nm and 476/633 nm, respectively [411].

with the direct gap of GaAs) and E_1 at 1.447 eV and 1.472 eV, respectively. The authors interpret these features as being due to transitions to the first two quantized energy levels ($n=0, 1$) of the 2DEG in the nearly triangular well at the GaAs/GaAlAs interface. Thus, these authors conclude that, using DPR, they can indeed observe effects directly related to the 2DEG.

Martins *et al.* also have investigated the temperature dependence of the PR signal from an MDHJ [410]. In contrast to the observations of refs. 407 and 408 discussed above, they find that the obtained field does not go to zero as the temperature is lowered, but has a behaviour consistent with that of a 2DEG.

Another interesting aspect of PR from GaAs/GaAlAs 2DEG structures has recently been published. Photoreflectance from GaAs/GaAlAs MDHJs at 4 K in sample regions shaded from laser pump beam illumination has exhibited low-level signals attributed to the modulation of the 2DEG. It was reported that the signal persisted furthest from the illuminated portion in samples with exceptional 2DEG mobility [423].

As mentioned above, GaAlAs/InGaAs/GaAs MDQW structures offer a more well-defined system in which to study modulation spectroscopy of the 2DEG [401,402]. In such samples, the 2DEG resides in the InGaAs channel, which is spectrally separated from the other regions of the material, i.e. GaAlAs and GaAs. A detailed PR study at 300 K of three step-doped pseudomorphic $\text{Ga}_{1-y}\text{Al}_y\text{As}/\text{In}_x\text{Ga}_{1-x}\text{As}/\text{GaAs}$ MDQWs with nominal $L_z = 100 \text{ \AA}$, $y=0.2$, $x=0.2$ (samples 1 and 2) or $x=0.16$ (sample 3) has been performed by Yin *et al.* [402]. The authors detected several features from the InGaAs MDQW portion of the samples in addition to signals from the GaAlAs and GaAs regions. The InGaAs spectra exhibit an unusual EM spectroscopy lineshape. These spectral features can be explained on the basis of a step-like two-dimensional density of states, due to the screening of the excitons by the 2DEG, and a Fermi level filling factor. From the details of the lineshape fit they extracted the Fermi level position and hence N_s . The obtained values for the electron sheet density are in good agreement with Hall measurements on the same samples. In addition, several intersubband transition energies in the InGaAs MDQW can be obtained. By comparing these experimental energies with a theoretical self-consistent Schrödinger–Poisson calculation, it was also possible to evaluate other important materials parameters, such as L_z , In composition and built-in electric field. The GaAlAs signal also yielded the Al composition (y).

The solid lines in Fig. 48 are the PR traces originating in the InGaAs MDQW section of the samples. The lineshapes are unusual for modulation spectroscopy from a QW system. Such traces generally exhibit sharp, derivative-like features (i.e. positive and negative lobes) associated with excitons, even at 300 K. In addition, these reported lineshapes are symmetrical (see, for example, Fig. 2). The traces of Fig. 48 lie on only one side of the baseline, with the exception of the highest-lying sharp peak of sample 3. We shall return to this resonance later.

Electromodulation lineshapes from a bound system can be expressed by eqns. (1) and (17). In undoped QW structures, even at 300 K, the absorption profile (ϵ_2) consists of sharp excitonic peaks, superimposed on a step-like two-dimensional (2D) joint density of states (2DJDS). In this case, $\Delta\epsilon$ in eqns. (1) and (17) will be the first derivative of a Lorentzian or Gaussian profile, depending on the nature of the broadening mechanism of the exciton. However, the presence of a sufficiently dense 2DEG (or 2D plasma) produces a screening which wipes out these strong excitonic resonances. In such a system, the intersubband transition absorption function will be a broadened step-like 2DJDS multiplied

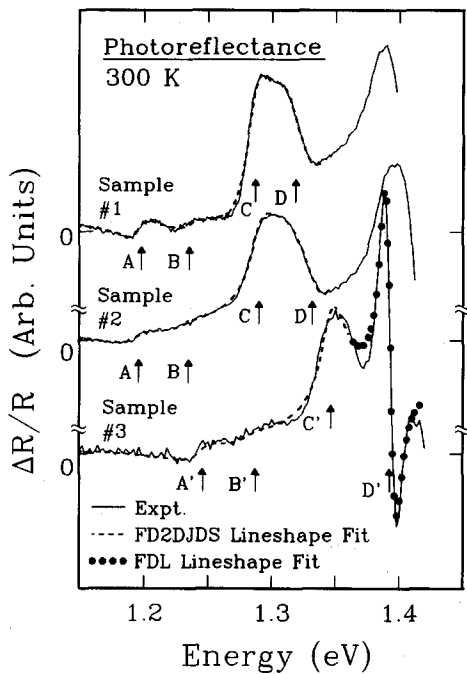


Fig. 48. Solid lines are the experimental photoreflectance spectra from the InGaAs region of three GaAlAs/InGaAs/GaAs MDQWs. The dashed and solid lines are least-squares fits to FD2DJDS and FDL lineshapes, respectively. The obtained values of the intersubband energies are designated by arrows [402].

by a Fermi level filling function. This lineshape can be expressed as [402]

$$\epsilon_2 = \sum_j I_j \text{Im}\{\ln[E_j(mnH) - E + i\Gamma_j]\}[1 - f_e^j] \quad (37a)$$

where I_j is the amplitude of the j th spectral feature, Im denotes the imaginary part, E is the photon energy, Γ_j is the broadening parameter and $E_j(mnH)$ is the intersubband energy given by

$$E_j(mnH) = E_{m,j}^c - E_{n,j}^v(H) \quad (37b)$$

In eqn. (37b), $E_{m,j}^c$ and $E_{n,j}^v(H)$ are the energies of the m th conduction and n th heavy hole (out-plane) valence subbands, respectively, associated with the j th feature.

The Fermi function in eqn. (37a) can be expressed as:

$$f_e^j = \{1 + \exp[\lambda E - \lambda E_j(mnH) - E_j(m)]/kT\}^{-1} \quad (38a)$$

with

$$E_j(m) = (E_F - E_{m,j}^c) \quad (38b)$$

where E_F is the Fermi energy.

The parameter λ in eqn. (38a) is given by

$$\lambda = m_h^*/(m_c^* + m_h^*) \quad (38c)$$

where m_c^* and m_h^* are the conduction and in-plane heavy hole effective masses, respectively, in units of the free electron mass.

The dashed lines in Fig. 48 are least-squares fits to eqns. (1), (17), (37) and (38). This first-derivative of a 2DJDS lineshape is designated as an FD2DJDS lineshape. The fitting parameters are A_j , $E_j(mnH)$, Γ_j and $E_j(m)$. The obtained intersubband energy gaps, $E_j(mnH)$ for $j=A, B, C$ and D (except for sample 3 with $j=A', B'$ and C') are indicated by arrows and are also listed in Table 2. The sharp, high-energy "S"-shaped structure of sample 3 (labelled D') has been fitted with eqns. (1) and (17) using a Lorentzian absorption profile (dotted line). This first derivative of a Lorentzian lineshape is labelled FDL. The obtained intersubband energy is also indicated by an arrow and is presented in Table 2.

These features for samples 1 and 2 correspond to $mnH=11H$ ($j=A$), $12H$ ($j=B$), $21H$ ($j=C$) and $22H$ ($j=D$). The situation for sample 3 is more complex. The background on which these resonances are superimposed is due to the Fermi filling factor ($1-f_e^j$), in eqn. (37a). The fit to this background makes it possible to evaluate $E_A(m)=62$ meV, 71 meV and 56 meV for samples 1, 2 and 3, respectively.

In order to identify the origins (i.e. m and n) of the InGaAs MDQW features, the authors have performed a theoretical self-consistent Schrödinger-Poisson calculation of the subband and intersubband energies and intersubband intensities (wavefunction overlap) including the influence of the large electric field in the InGaAs MDQW. These theoretical results are also listed in Table 2. For samples 1 and 2 the overall agreement is very good, if structure A is identified with 11H etc. For sample 3 the features A' and C' can be correlated with 11H and 21H, respectively. The question of the nature of B' and D' is discussed below.

Based on this calculation, it is also possible to evaluate the position of E_F relative to the electron ground state ($m=1$) of the system. Since $m=1$ for the features $E_A(mnH)$, one can determine that $E_A(m)=E_A(1)$. Hence, from the above-mentioned fitted values of $E_A(m)$ and eqn. (38a), the authors conclude that $E_F-E_1^c=+62$ meV, +71 meV and +56

TABLE 2. Experimental and theoretical values of various intersubband transition energies from the InGaAs MDQW region of three $Ga_{1-y}Al_yAs/In_xGa_{1-x}As/GaAs$ MDQWs. Also listed are N_s from the room temperature PR experiments and Hall measurements at 77 K and 300 K (parentheses) [402]

Sample	Intersubband characteristics				$N_s (10^{12} \text{ cm}^{-2})$	
	Spectral feature	Expt. (eV)	Theory (eV)	Transition	PR expt.	Hall measurement
1	A	1.198	1.203 ^a	11H ^a	1.90 ± 0.2^a	$1.90 \pm 0.1 (1.60 \pm 0.1)^e$
	B	1.235	1.238 ^a	12H ^a		
	C	1.287	1.307 ^a	21H ^a		
	D	1.319	1.341 ^a	22H ^a		
2	A	1.196	1.204 ^b	11H ^b	2.15 ± 0.25^b	$2.00 \pm 0.1 (1.77 \pm 0.1)^e$
	B	1.234	1.239 ^b	12H ^b		
	C	1.292	1.307 ^b	21H ^b		
	D	1.332	1.342 ^b	22H ^b		
3	A'	1.246	1.246 ^c	11H ^c	1.85 ± 0.20^c	$1.75 \pm 0.1 (1.68 \pm 0.1)^e$
	B'	1.287	-	(12H) ^{c,d}		
	C'	1.346	1.341 ^c	21H ^c		
	D'	1.393	-	(22H) ^{c,d}		

^a $y=0.195, x=0.2$

^b $y=0.185, x=0.2$

^c $y=0.175, x=0.16$

^dThe 2H valence level is unbound.

^e300 K.

meV for samples 1, 2 and 3, respectively. The quantity $E_2^c - E_1^c$ (~ 100 meV) can be obtained from the separation between 21H and 11H (see Table 2). Thus the Fermi level lies between the $m=1$ and $m=2$ conduction subbands.

It can be shown that for the case of a broadened step-like 2D density of electron states, N_s is given by (for $kT \ll E_F$) [402]

$$N_s = (m_e^*/\pi\hbar^2) \sum_m \int_0^\infty \{(1/2) + (1/\pi) \arctan[(E - E_m^c)/\Gamma_m]\} \times \{\exp[(E - E_F)/kT] + 1\}^{-1} dE \quad (39)$$

From eqn. (39) and the values of E_F and E_m^c discussed above, the calculated numbers for N_s for the three samples listed in Table 2 were obtained. There is very good agreement between the PR analysis of N_s and the 77 K Hall measurements, which also are displayed in Table 2. For completeness, also listed in Table 2 are the N_s values from the 300 K Hall determinations.

Consider the question of sample 3. Because of the lower In content of this sample in relation to the other two materials, the 2H valence level becomes unbound, and hence m2H transitions should be very weak in a one electron picture. However, experimentally Fig. 48 shows evidence for the contribution of 12H (feature B') and a very strong FDL resonance (D') which appears to correspond to 22H. The fact that the D' structure has an FDL lineshape strongly suggests that its origin is an unscreened exciton. Clearly further work needs to be done with regard to this peak.

Both the GaAs and GaAlAs features in the PR spectra of ref. 402 exhibit pronounced FKOs, which made it possible to obtain the electric fields in the respective regions. Also, from the positions of the GaAlAs peaks it was possible to evaluate the Al compositions. Comparison of the fields deduced from the FKOs with the self-consistent Schrödinger–Poisson calculation yielded information about pinning levels at various interfaces.

Yin *et al.* also have used PR and Schottky barrier ER to perform a similar characterization of the 2DEG in a planar-doped pseudomorphic GaAlAs/InGaAs/GaAs MDQW structure ($L_z = 150$ Å) in the temperature range 79 K $< T < 304$ K [401]. In this sample, the Fermi energy was close to the second conduction subband. As in the previous work, the value of N_s (2.2×10^{12} cm $^{-2}$ at 304 K) deduced from the EM spectra was in good agreement with a Hall measurement.

8.8. External perturbations

8.8.1. Electric fields

Studies of the effects of externally applied electric fields have been very important in the understanding of many fundamental properties of semiconductor microstructures, including the quantum confined Stark effect in SQWs [8,378,424], coupling (and decoupling) between symmetric [76,378,424,425] and asymmetrically [426] coupled double quantum wells and Wannier–Stark quantization [360,424,427–430] in III–V SLs. External electric field-dependent ER and electrotransmission have been performed on two GaAs/Ga_{0.7}Al_{0.3}As MQWs ($L_z = 87$ Å and 158 Å) [431]. Pearsall has reported the influence of an external electric field on the ER spectra at 40 K from an (001) Ge₆Si₄/Ge short-period SL [392]. The influence of large electric fields, generated by the strain-induced piezoelectric effect, has been observed in an InGaAs/GaAs SQW [432]. This experiment is discussed in Section 8.8.4.

The details of the field-induced changes in the ER spectra of asymmetrically (InGaAs/GaAs and GaAs/GaAlAs) [426] and symmetrically (GaAs/GaAlAs) [76] coupled double

quantum wells have been used to evaluate not only energy shifts, but also to characterize the resonance of the coupling. Figure 49 shows a schematic diagram of the InGaAs/GaAs asymmetrically coupled double quantum well (ASDW) structure [426]. For clarity, only the $m=1$ conduction and $n=1$ heavy hole states are indicated. With no field ($F=0$), the subbands in neighbouring wells are not in resonance. This is in contrast to the symmetric coupled double quantum well (SCDW) in which both electrons and holes (HH and LH) strongly couple for $F=0$. Thus for the ASDW the applied field can control separately the coupling between electrons or holes. A direct (D,d) or indirect (I,i) transition is one which results in a large probability that the photoexcited electron and hole end up in the same or different wells, respectively. The upper and lower case letters represent transitions originating in the wide and narrow wells, respectively. Also, for clarity Fig. 49 indicates only transitions from the wide well. At $F=0$ indirect (I,i) transitions are forbidden, since there is no overlap of either the electron or hole states. With an applied field there is a resonant coupling between the two wells and hence the indirect transition is possible. Figure 49 shows the case for coupling of the electron states. The authors point out that in resonance, the direct and indirect designation lose their meaning, since there are equal amounts of wavefunction in both wells. At higher fields, the states decouple and the wells once again become isolated.

Figure 50 shows a series of ER and photoconductivity (PC) spectra at 10 K for biases near resonance for the InGaAs/GaAs sample. For $F=10 \text{ kV cm}^{-1}$ (low-field) transitions from both the wide (11HD, 11LD, 11HI) and narrow (11Hi, 11Hd) wells are observed. Based on a lineshape analysis (but not a detailed fit) the authors conclude that the lineshapes

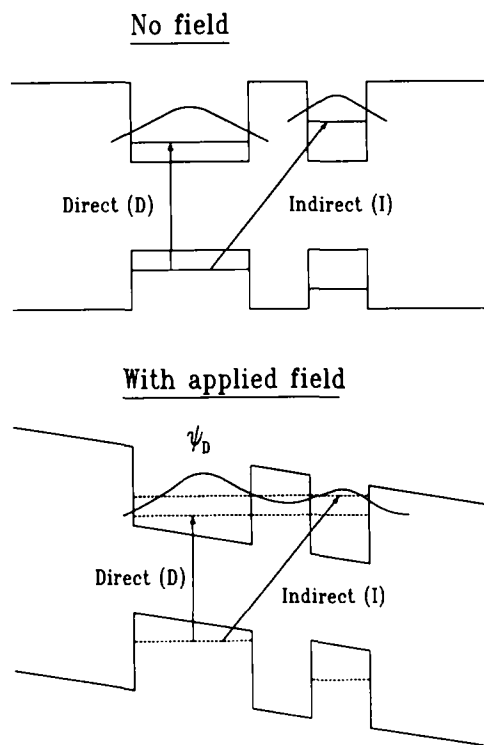


Fig. 49. Schematic representation of an asymmetrically coupled double quantum well system as a function of electric field [426].

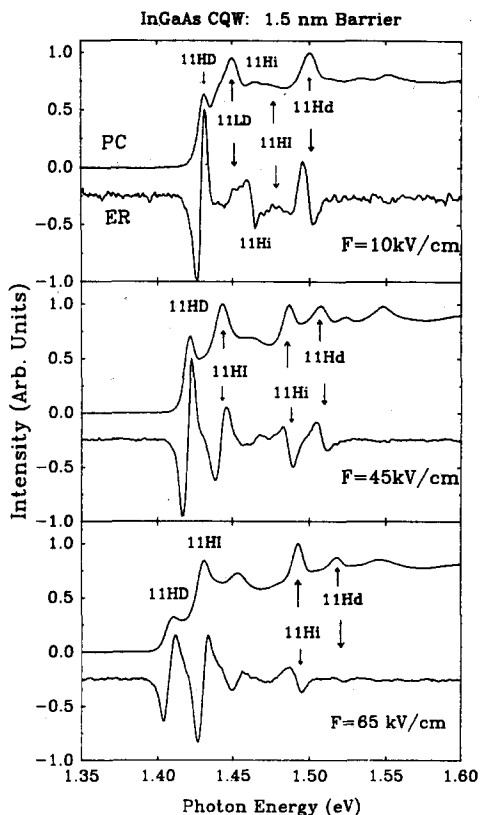


Fig. 50. A comparison of electroreflectance (ER) and photoconductivity (PC) spectra of an InGaAs/GaAs asymmetrically coupled double quantum well for fields of 10 kV cm^{-1} , 45 kV cm^{-1} and 65 kV cm^{-1} [426].

for 11HD and 11Hd are due to the gap modulation term of eqn. (17), i.e. $\partial\epsilon/\partial E_g$. Using a detailed line shape fit, Huang *et al.* [76] also concluded that for the SCDW that $\partial\epsilon/\partial E_g$ is the dominant term.

The middle trace of Fig. 50 ($F=45 \text{ kV cm}^{-1}$) displays spectra at a field near the resonant condition for the electrons. The main peaks in the PC data are split into two structures of nearly equal intensity, associated with direct and indirect transitions. At this field the ER data also exhibit two structures per well. More importantly, the phase relation between the transitions in the wide and narrow wells is clear. It is this aspect of the ER spectrum, as well as its sharpness, that allows the modulation method to be more specific than the PC results. This phase relation is a direct consequence of the fact that the energy levels shift in opposite directions in the wide and narrow wells.

The bottom part of Fig. 50 shows the spectra at a field ($F=65 \text{ kV cm}^{-1}$), which is beyond the resonance point. Transitions which were once direct are now getting weaker, and those that were indirect are stronger. Further increases in field create a situation in which 11HI and 11Hi dominate.

In order to understand more fully the ER spectra of Fig. 50, the authors have theoretically evaluated the field-dependent energies (and wavefunctions) of the various transitions. There is excellent agreement between the experimentally determined energies and the calculation. The authors find that the slopes of the field dependence of the energies for the wide well are opposite to those for the narrow well, which explains the phase differences between 11HD(I) and 11Hd(i) in Fig. 50. It was also found that the slope of 11Hi changes sign at

about 75 kV cm^{-1} . A high-field ($F = 135 \text{ kV cm}^{-1}$) measurement verified the phase change of this feature in relation to the low-field phase.

A similar detailed analysis of both energies and phases has been reported in an ER study at 77 K of a GaAs/GaAlAs SCDW [76]. The high fields reached in this work (300 kV cm^{-1}) made it possible to observe not only (a) decoupling effects and Stark shifts (i.e. shifts linear in F) at low fields but also (b) at high fields a substantial QCSE and field-induced broadening (due to tunnelling effects) of the fundamental heavy hole transition in the decoupled wells.

Shields *et al.* have reported a 17 K study of the dependence of external electric fields on the ER and electrotransmission spectra of two GaAs/GaAlAs MQWs [431]. Photocurrent and transmission spectra were also taken at different biases for comparison. Each technique shows splittings of the fundamental conduction to heavy and light hole transitions, i.e. 11H and 11L, respectively. The authors argue that these bias-dependent splittings derive from sudden changes in the well width at certain depths in the stack.

Electrotransmission has been used to study the effects of electric fields on the electronic states of InGaAs/InAlAs [433,434] and InGaAs/InGaAsP [435] quantum wells.

In an SL the wavefunctions extend throughout the entire microstructure, owing to resonant coupling between the quantum wells, which results in the formation of a miniband (see Fig. 34). This resonant condition is broken by the application of an electric field. Also, the eigenstates tend to localize in the quantum wells (Wannier–Stark localization). This localization also causes Stark ladder formation, i.e. interband transition energies that are red (blue) shifted linearly in the field.

Using Schottky barrier ER at low temperatures, Voisin *et al.* [427] have observed Wannier–Stark quantization in a GaAs/GaAlAs SL. This Wannier–Stark quantization manifests itself as an effective blue shift of the optical absorption edge and is also accompanied by a new type of electro-optic oscillation of the absorption coefficient, which is periodic in F^{-1} . Figure 51(a) shows the low-temperature and low-voltage ER spectrum of the SL. The data show rich and sharp structures in the energy range corresponding to the lowest-lying quantized SL transitions. The sharp features denoted A and B correspond to 11H and 11L transitions at the minizone centre (Γ), respectively, while C and D are due to 11H and 11L at the minizone edge (π), respectively. This gives a direct measure of the subband widths. The evolution of the ER spectra with increasing reverse bias is shown in Fig. 51(b). The main lines A and B at first clearly shift toward higher energies, while their amplitudes increase. Then at higher fields, both the blue shifts and the amplitudes tend to saturate and a hint of a red shift is observed. This latter effect is due to the intrawell QCSE, as discussed above. Other structures, probably due to “indirect” transitions can be observed in the spectra of Fig. 51(b), particularly below the A[11H(Γ)] feature.

Using ER at 77 K on a GaAs/GaAlAs SL, Nakayama *et al.* [429] have, for the first time, observed Stark ladder formation of the second quantized state in addition to the ground state (see Figs. 51(a) and 51(b)). From a comparison between ER and PC they deduce that ER is much more sensitive for probing the Stark ladder transition than PC. In related studies, resonant coupling between Wannier–Stark localized states was detected using ER [430,436,437]. The Stark ladder behaviour of the X levels in a type II GaAs/AlAs SL has been observed in ER [428].

Schneider *et al.* [438] and Ribeiro *et al.* [439] have observed the step-by-step evolution of the electromodulation signal from FKOs to Wannier–Stark localization as a function of d.c. bias voltage in GaAs/AlAs and InGaAs/GaAs SLs, respectively.

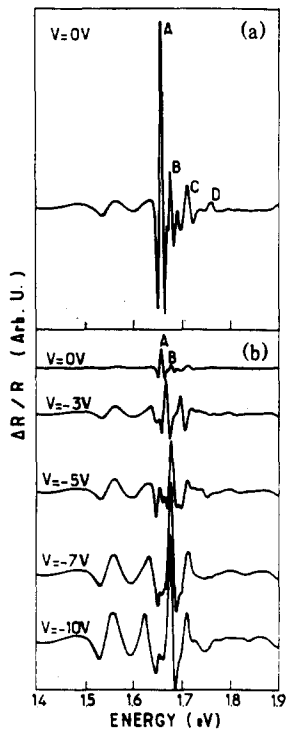


Fig. 51. (a) Low-temperature and low-voltage electroreflectance spectrum of a GaAs/GaAlAs SL and (b) evolution of the features with applied reverse bias [427].

The effect of an external electric field on the ER signals at 40 K from a (001) $\text{Ge}_6\text{Si}_4/\text{Ge}$ short-period SL as well as (001) bulk Ge (E_0) has been presented by Pearsall [392]. The E_0 spectra of the bulk Ge exhibit FKO's and the "lineshape rotation" discussed in Section 4.1. The ER traces from the SL sample are quite complicated because of the proximity of E_0 and $E_0 + \Delta_0$ components from the Ge buffer/substrate and the signals from the Ge_6Si_4 SL. For high reverse bias there is a pronounced "red shift" of the entire SL spectrum. No definitive explanation for this effect has been given.

8.8.2. Temperature

8.8.2.1. Temperature dependence of intersubband transitions Systematic studies of the effects of temperature on the modulated spectra of various microstructures have revealed important information about the dependence of (a) the energies of quantized levels [181,192,193,309,310,337,340,356,357,440,441], (b) the broadening parameter [192,193,309,310,337,442], (c) zone-folding effects [443] and (d) the details of the lineshape (see Section 8.1). Investigations of the temperature dependence of the broadening parameter are of special interest, since they can be used to study the fundamental nature of the electron (exciton)-LO phonon interaction in reduced dimensional systems [192,193].

The temperature dependence of the quantized energy levels in the GaAs/GaAlAs [192,193,440], InGaAs/GaAs [309,310] and $\text{Ge}_{32}\text{Si}_8/\text{GeSi}$ [384] systems is essentially the same as that of the direct gap of the relevant bulk constituent material, with the exception of Ge-rich $(\text{Si})_m/(\text{Ge})_n$ SLs [181] and monolayer InAs/GaAs structures [357]. For InAs/GaAs SQWs with 2, 3 and 4 monolayer thicknesses the fundamental 11H transition has a temperature-

dependent red shift that is approximately linear, with slope of -2.2×10^{-4} eV K $^{-1}$. This is significantly lower than that of either bulk constituent material ($\sim -4 \times 10^{-4}$ eV K $^{-1}$). No explanation was given for this effect [357].

8.8.2.2. Temperature dependence of the linewidth The temperature variation of the broadening parameter, $\Gamma(T)$, of the 11H exciton feature of quantum structures offers an interesting way to explore the dependence of the electron-LO phonon coupling on dimensionality. In reduced dimensional systems, the electron (exciton)-optical phonon interaction is affected not only by changes in the electron wavefunction due to the confining potential, but also by changes in the LO phonon modes caused by phonon confinement. This effect leads to a reduction in the electron-LO phonon coupling as the dimensionality is decreased [192,193]. The temperature dependence of $\Gamma(T)$ is directly related to the strength of this coupling (see eqn. (26)), and hence can be used to probe it.

Qiang *et al.* have used PR in the range 10 K $< T <$ 500 K to study $\Gamma(T)$ of the 11H transition of four GaAs/GaAlAs SQWs with $80 \text{ \AA} < L_z < 200 \text{ \AA}$ in relation to the broadening parameter of E_0 of bulk GaAs [192]. Figure 52 shows the results of their investigation for E_0 of bulk GaAs and two SQWs with $L_z = 200 \text{ \AA}$ and 80 \AA . Clearly $\Gamma(T)$ becomes less sensitive to temperature as the dimensionality of the system is reduced. The solid lines are least-squares fits to eqn. (26), which yield Γ_{ep} , the exciton-LO phonon coupling coefficient, for these samples. This equation has also been successfully used to fit $\Gamma(T)$ for 11H of GaAs/GaAlAs MQWs [442] and an InGaAs/GaAs SQW [309,310]. It was found by Qiang *et al.* [192] and Pollak [193] that Γ_{ep} scales approximately linearly with L_z for the GaAs/GaAlAs SQWs of Fig. 52, in agreement with theory (for $L_z \geq 40 \text{ \AA}$). Shown in the inset are the experimental values of Γ_{ep} as a function of L_z . The dashed curve is a least-squares fit to a linear function drawn through the origin. These authors also present evidence for the size dependence of Γ_{ep} based on the results of other experiments [192,193].

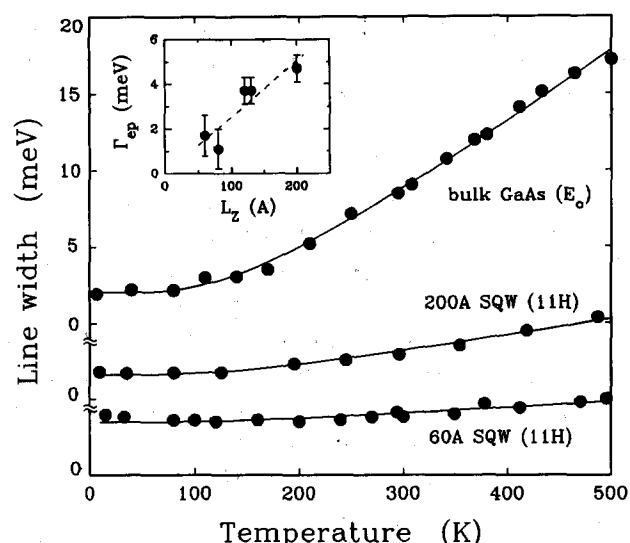


Fig. 52. The temperature dependence of the broadening parameter $\Gamma(T)$ for the direct gap of bulk GaAs and the 11H excitonic transitions in GaAs/GaAlAs SQWs with $L_z = 200 \text{ \AA}$ and 80 \AA . The solid lines are fits to eqn. (26) [192,193].

It is interesting to note that Nakazawa *et al.* [443] have observed that $\Gamma(T)$ is almost independent of temperature for $(\text{GaAs})_n/(\text{AlAs})_n$ SLs ($n=1-15$), probably due to the dimensionality effect discussed above.

8.8.3. Hydrostatic pressure

The quantized transitions in GaAs/GaAlAs, InGaAs/GaAs [356] and GaSb/AlSb quantum well structures have been studied using PR under high hydrostatic pressure (60 kbar). Most of these works are reviewed by Chandrasekhar and Chandrasekhar [444].

An important application of this perturbation has been to measure the valence band offset in the GaAs/GaAlAs system [445]. The hydrostatic pressure causes the conduction subband levels in the GaAs well to move up in energy until they interfere with the red-shifted X conduction minima of the GaAlAs barrier. Staggered transitions across the interface from the X conduction band of the GaAs valence band are seen in PR, signalling the formation of a type II heterostructure beyond these pressures. This crossover made it possible to deduce ΔE_v .

It has been found that the hydrostatic pressure coefficients of the energies of the subbands in these structures are not necessarily the same as that of the constituent bulk material, in contrast to the temperature variation (see Section 8.8.2). For deep wells and subbands close to the bottom of the well (wide wells) it is found that the pressure coefficient of the energies of the intersubband transitions is indeed close to that of the bulk well material. However, for higher subbands this is no longer true. The reasons for this behaviour in terms of the pressure dependence of the effective mass, well width, exciton binding energy and barrier heights have been discussed.

Strained layer GaSb/AlSb MQWs [446] and ZnSe/GaAs epilayer [447] systems displayed an additional influence of the pressure. If the substrate has a different elastic constant in relation to the epitaxial quantum structure, the latter may experience a different amount of strain from that of the applied pressure, which can also result in a uniaxial component along the growth direction. The former effect leads to a change in the pressure coefficient while the latter (uniaxial) strain will alter the separation between the HH and LH levels. Thus it is possible to pressure-tune the LH-HH splitting. These effects have been observed using PR in conjunction with a diamond anvil high-pressure cell.

8.8.4. Uniaxial stress

Although various optical methods, such as PL and PLE, have been used to investigate the effects of external uniaxial stress on the electronic states of quantum structures [194], to date relatively little work using modulation spectroscopy has been reported [196–198,432].

The effects of large, external uniaxial stress (S) along [100] and [110] on the quantum states of a strained layer (001) $\text{In}_{0.21}\text{Ga}_{0.79}\text{As}/\text{GaAs}$ SQW has been investigated using PR at 300 K [432]. For $S \parallel [100]$ (≈ 8 kbar), the stress-induced shifts of the various quantum transitions are in good agreement with a theoretical calculation based only on deformation potential theory, including the strain-induced coupling between LH and spin-orbit split valence bands. The heavy hole (out-plane) derived transitions are relatively insensitive to S because of the cancellation between the hydrostatic and shear components of the strain. At high stresses there is a small non-linear effect due to the coupling with the spin-orbit split band. However, for the light hole (out-plane) features the hydrostatic and shear terms add, resulting in a relatively large stress-induced shift. This effect is the reason for the

enhancement of LH versus HH transitions observed in PZR (see Section 8.3). Thus, static external stress could also be used to discriminate between HH and LH transitions. For $S \parallel [100]$ there was no significant change in the intensities of the various PR features.

The situation for $S \parallel [110]$ (≈ 18 kbar) was quite different. For this lower symmetry stress direction there was a dramatic increase in the intensities of the 12H and 13H "symmetry-forbidden" features relative to the "symmetry-allowed" 11H peak. Also, there was a significant red shift of 11H, 12H and 13H at high stresses. This phenomenon has been interpreted in terms of an electric field generated along the growth direction induced by the piezoelectric coupling for $S \parallel [110]$. The experimental energies of the various transitions are in good agreement with a theoretical calculation based not only on deformation potential effects, but also on a QCSE red shift due to the stress-induced piezoelectric field. The agreement between experiment and theory (including the piezoelectric effect) shows that the full piezoelectric field is being generated across the SQW.

A similar PR study, i.e. $S \parallel [100]$ and $S \parallel [110]$, has been performed on a (001) GaAs/GaAlAs SQW structure [196]. Again, for $S \parallel [100]$ the stress-induced shifts can be explained using only deformation potential theory while for $S \parallel [110]$ there are also effects due to the piezoelectric field generated along the growth direction. However, in contrast to the case of the InGaAs/GaAs SQW experiment discussed above, the magnitude of this piezoelectric field is considerably smaller than that predicted by theory. This phenomenon has been interpreted in terms of screening charges.

The effects of large external $S \parallel [100]$ on the interband transitions of two GaAs/GaAlAs SQWs grown on (001) Si have been observed using PR at 300 K [197,198] and 77 K [198]. The GaAs/Si structure is under an in-plane biaxial tensile stress arising during post-growth cooling from the differences in their expansion coefficients. The above external stress configuration makes it possible to externally alter the LH and HH splitting. In an SQW of width 200 Å, the ground state was continuously tuned from LH to HH.

8.8.5. Magnetic fields

Zhou *et al.* [417] have measured the effects of magnetic fields up to 15 T on the PR spectra of δ-doped GaAs samples. Parallel fields not only suppress the above-gap oscillatory structure (see Section 8.5) but cause a large increase in the PR signals near the GaAs energy gap. This enhancement is ascribed to the stabilization of the exciton in the magnetic field in the presence of the built-in electric fields. At 4.2 K, Landau-like spectral features are observed for fields applied perpendicular to the doping layer.

9. Device structures

Modulation spectroscopy, particularly contactless EM methods such as PR and CER, is also becoming an important tool for studying and characterizing actual device structures, such as heterojunction bipolar transistors (HBTs) (GaAs/GaAlAs [125,448], InP/InGaAs [449], InGaAs/GaAs [450]), high electron mobility transistors (HEMTs)(GaAlAs/InGaAs/GaAs [401,402] and possibly GaAs/GaAlAs [411,423,451]), GaAs/GaAlAs superlattice optical mirrors [452], GaAs/AlGaAs multiple quantum well infrared detectors [453] and GaAs/GaAlAs resonant tunnelling structures [81,82], as well as MIS configurations [454–456]. Electroreflectance and electrotransmission have been used to characterize InGaAs/InGaAP broad area quantum well lasers [377,457,458]. Since PR/CER are completely contactless,

in contrast to PZR and TR which require special mounting, they can readily be performed on production line, wafer-sized samples.

The PR characterization of GaAs/GaAlAs HBTs is of particular significance, since certain features in the spectra of samples before fabrication have been correlated with actual device performance after fabrication [125,448]. Thus PR has been shown to be an effective contactless and non-destructive means of screening wafers before they are made into actual devices. The work of ref. 125 was actually performed on wafer-sized samples. These HBT structures exhibited FKOs associated with the built-in electric fields in the n⁻ GaAs collector region and the wide gap Ga_{1-x}Al_xAs emitter portion. These measurements have made it possible to evaluate the built-in fields as well as the Al composition. The values of these fields are in good agreement with those deduced from computer-generated models of the device structure. The most significant aspect of these studies was the correlation of the fields deduced from the GaAlAs FKOs and the d.c. current gains in fabricated HBTs. Below electric field values of about 2×10^5 V cm⁻¹, high current gains were obtained, while for higher fields the gain dropped substantially. The explanation of this effect is the redistribution of the Be dopant in the p-region. When the redistribution moves the p-n junction into the emitter, there is an increase in the electric field in this region, i.e. the value of the field deduced from the GaAlAs FKO becomes greater [125].

Figure 53 shows the PR spectra at 300 K of HBT sample 1 (fabricated by MBE) and sample 2 (fabricated by MOCVD) [125]. There are a number of FKO in the vicinity of both the GaAs (collector) and GaAlAs (emitter) band gaps. The obtained values for the maximum d.c. electric fields ($F_{d.c.}$) in the n⁻-GaAs collector and GaAlAs emitter regions of sample 1 are 3.65 and 18.0 (in units of 10^4 V cm⁻¹), respectively, while for sample 2 the corresponding numbers are 3.24 and 22.9. These were typical of the MBE and MOCVD materials that were investigated. Note also that the Al composition can be determined from the band gap deduced from the GaAlAs FKOs.

The electric fields deduced from the GaAlAs FKO ($F_{d.c.}(\text{GaAlAs})$) were compared with fabricated HBT current gains in the MBE samples. Below $F_{d.c.}(\text{GaAlAs})$ of about

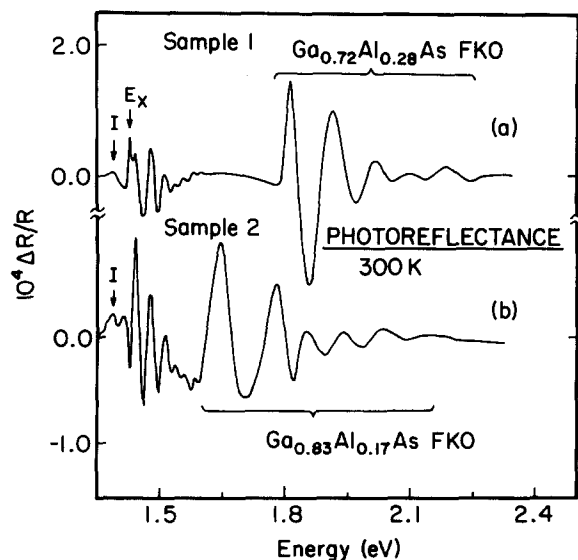


Fig. 53. Photoreflectance spectra at 300 K from GaAs/GaAlAs HBT samples 1 (grown by MBE) and 2 (grown by MOCVD) [125].

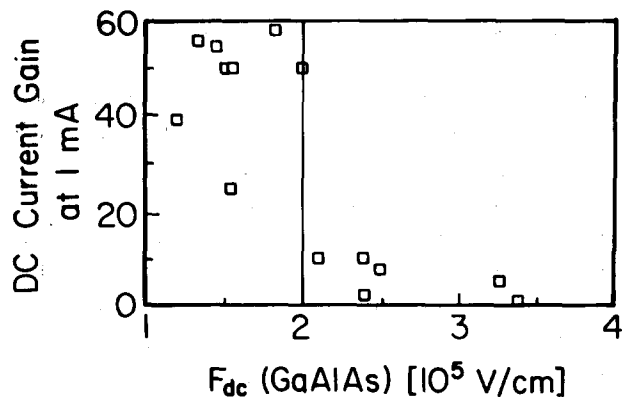


Fig. 54. Current gain at 1 mA as a function of $F_{dc}(\text{GaAlAs})$ for actual GaAs/GaAlAs HBT devices fabricated from MBE-grown samples such as those in Fig. 53 [125].

$2 \times 10^5 \text{ V cm}^{-1}$, high current gains were obtained. Figure 54 shows $F_{dc}(\text{GaAlAs})$ as a function of current gain at 1 mA. Note that there is a sudden drop when $F_{dc}(\text{GaAlAs}) \geq 2 \times 10^5 \text{ V cm}^{-1}$. The explanation of this effect was the redistribution of the Be dopant in the p-doped base region of these samples [125].

Photoreflectance has also been used to evaluate F_{dc} and associated doping profiles in the n-InGaAs collector and n-InP emitter regions of a lattice-matched InP/InGaAs HBT structure [449]. The obtained donor concentrations were about an order of magnitude smaller than the values intended from the growth conditions. Capacitance-voltage and secondary ion mass spectroscopy measurements were consistent with the PR determination. The origin of the discrepancy was the failure of the Si doping cell, which had occurred during the growth of the sample.

The results of refs. 401 and 402 have considerable implications for the evaluation of pseudomorphic GaAlAs/InGaAs/GaAs HEMTs. These works have demonstrated that PR/CER can be conveniently employed at 300 K to characterize many of the important parameters of these device structures. Analysis of the InGaAs trace yields the sheet density N_s , in addition to other properties of the channel, such as built-in field, In composition and width, L_z . Furthermore, the FKO's from GaAs and GaAlAs portions of the sample yield information about the built-in electric fields in these regions, due to Fermi level pinning at the relevant surfaces/interfaces, as well as the Al composition.

The situation for characterizing GaAs/GaAlAs HEMTs is less clear, since the observed GaAs signal could arise not only from the 2DEG portion, but also from different GaAs regions of the structure. This is not a problem for GaAlAs/InGaAs/GaAs HEMTs, since the InGaAs trace is spectrally isolated from GaAs and GaAlAs signals.

The results of ref. 423 on the correlation of the PR signal shaded from the pump laser beam and the 2DEG mobility are quite interesting and should be explored further.

10. *In situ* monitoring of growth/processing

Contactless modulation modes that require no special mounting of the sample, e.g. PR, EBER, DR and RDS, have considerable potential for the *in situ* monitoring/control of semiconductor fabrication conditions (a) at elevated temperatures during actual growth/processing and/or (b) post growth/processing before the sample is removed from the

preparation chamber. The capacitor configuration CER may be useful for the latter characterization.

Such monitoring methods could substantially reduce turn-round time. Also, they would be very useful in the case of all-vacuum processing, where the various growth/processing functions are interconnected. As mentioned in Section 2.1.2, RDS is already being utilized for the *in situ* characterization of epitaxial growth by MBE or OMCVD [41–45].

Photoreflectance can also be used for *in situ* work during growth [173–178]. For example, the direct gaps (E_0) of GaAs and $\text{Ga}_{1-x}\text{Al}_x\text{As}$ ($x \sim 0.17$) have been measured by PR as a function of temperature up to 690 °C, *in situ*, under actual OMCVD growth conditions, including a rotating substrate holder ($\approx 500 \text{ rev min}^{-1}$) and flowing gases [174–175]. The PR data for the position of E_0 of the GaAs sample made it possible to determine the near surface temperature directly. It was found that there was a systematic difference between this temperature and the reading of a thermocouple placed close to, but not in contact with, the rotating substrate. The measurement for the GaAlAs was used to determine the Al composition at these elevated temperatures. It has also been reported that the E_0 spectrum can be measured in about 30 s at 650 °C [176,178], thus offering the possibility the PR could be used for real-time monitoring.

It is clear from some of the discussions in previous sections that modulation methods can be used *in situ* post-growth/processing to evaluate many important materials parameters such as alloy composition, process-induced damage and annealing, strain, Fermi level pinning and metallization etc. For example, as recently stated by Murtagh *et al.* [217] “PR appears to have potential for on-line fabrication process control or wafer mapping of etch-induced semiconductor surface damage”.

In microstructures it is possible to measure well and barrier widths, barrier heights, strain (e.g. InGaAs/GaAs) and interface quality, in addition to actual device parameters.

11. Summary and future trends

This article has reviewed the experimental, theoretical and instrumentation advances that have occurred in modulation spectroscopy since the early 1980s. The emphasis in the first decade of this field was on the properties of bulk material, mainly in relation to the electronic band structure. Refined theories, particularly the low-field third derivative formulation of EM, enabled investigators to analyse modulation spectra quantitatively. The sharp, derivative-like features of modulated signals made it possible to study conveniently the band structure of a wide variety of semiconductors and to explore the influence of external perturbations. While a number of modulation methods were employed, EER was probably the most commonly used approach because of the ease of implementation.

During the past decade there has been a resurgence of this field. Experimental and theoretical work is being carried out on a wide variety of low-dimensional systems, such as compositional SQWs, MQWs and SLs, doping SLs, 2DEG, surface/interfaces etc. The large number of observed intersubband transitions in QWs and SLs, even at 300 K, offer the investigator an abundance of experimental data to compare to “band structure” effects, such as band offset, zone folding, coupling between wells, miniband dispersion, etc. There have been theoretical advances to account for the lineshape of these confined systems. As with bulk material, the rich modulated spectra of microstructures and the ability to fit lineshapes has enabled scientists to investigate the influence of electric fields (coupling and

decoupling effects including Wannier–Stark localization), temperature (high and low), large hydrostatic pressures, uniaxial stress etc.

While EM in the first decade concentrated largely on the low-field, third derivative regime in the past ten years there has been increasing interest in the intermediate-field situation where FKO_s are observed. Such FKO_s are extremely useful in evaluating the built-in d.c. fields that exist at surfaces/interfaces (due to Fermi level pinning) and p–n junctions (including devices such as HBTs).

General activity in the field has also prompted scientists to investigate further the properties of bulk materials, including the effects of high-temperature, process/growth-induced effects and the influence of annealing. New approaches to the lineshape of bulk materials, such as the GFF, have been proposed. Electrolyte electroreflectance is not only being used for various bulk and interface studies but, is also now a significant tool for electrochemists.

At present, the most widely used technique of modulation spectroscopy is PR. Although this method was developed in the early phases of modulation spectroscopy, it fell into obscurity because of experimental difficulties associated with spurious background signals and probably because EER was simpler. The work of Glemboki *et al.* [9,10] revived this important contactless EM approach. Photoreflectance is extremely useful, since it is not only contactless, but requires no special mounting of the sample. It can be utilized under a wide variety of conditions such as elevated temperatures, including *in situ* monitoring of growth, in the restrictive environment of a diamond anvil cell and for uniaxial stress studies. In contrast to PZR (or TR) this EM method exhibits FKO_s in relevant situations. Also, there is other information to be gain from pump frequency, amplitude and wavelength dependence. The problem of the spurious background signal has been reduced or eliminated by approaches such as the use of a VNDF for normalization, a double monochromator system, dye laser as probe beam, sweeping PR or DPR. The newly developed contactless EM method of CER offers an important complement to PR.

Older methods, such as PZR, TR, WMR, DR₁ and RDS are also being employed, sometimes in new ways, such as with RDS. In addition, investigators have developed new methods, particularly contactless approaches, such as EBER, DR₂ and CER.

There are a number of interesting new directions for modulation spectroscopy. To date, no work has been reported on low-dimensional structures, such as quantum wires, boxes or dots. While almost all of the reported work on compositional QWs and SLs has been on rectangular wells with (001) configuration, it would be extremely interesting to explore further different potential profiles, such as sawtooth and parabolic profiles. Also, different orientations, such as (111), should be investigated, particularly to determine the orientation dependence of the band offset. Strained layer (111) configurations with large piezoelectric fields offer new areas of study. The interpretation of the PR signal from GaAs/GaAlAs MDHJ structures that contain a 2DEG has not fully been resolved.

The use of FKO_s in special structures such as UN⁺(UP⁺) offers interesting new possibilities to study Fermi level pinning at surfaces/interfaces. Using PR, EBER or CER, such studies could be performed under a wide variety of conditions, including *in situ* measurements. To date, only work on GaAs and GaAlAs UN⁺(UP⁺) structures has been reported, but clearly other materials, such as InGaAs, InP and GaP should be explored.

More work on actual devices will probably be undertaken. The results on GaAs/GaAlAs and InP/InGaAs HBTs and GaAlAs/InGaAs/GaAs HEMTs has already demonstrated the utility of this method, particularly PR/CER.

Modulation spectroscopy, particularly PR, combined with other spectroscopic techniques, such as RDS and spectral ellipsometry, would be extremely useful for *in situ* monitoring during actual growth/processing conditions or post-growth before removal from the fabrication chamber. Advances in instrumentation to improve data acquisition times would be highly desirable.

Note added in proof

Modulation spectroscopy also has recently been used to study semiconductor nano-structures. Mei *et al.* [459] measured the electrotransmission spectra of $\text{CdS}_x\text{Se}_{1-x}$ nanocrystals imbedded in a glass matrix. Quantum dots of GaAs/GaAlAs fabricated by RIE have been investigated using PR at room temperature [460].

Acknowledgements

FHP acknowledges the partial support of NSF grant DMR-9120363, Army Research Office contract DAAL 03-92-G-0189, the Olympus Corporation and the New York State Science and Technology Foundation through its Centers for Advanced Technology program. We have benefitted greatly from conversations with D.E. Aspnes, J.W. Garland, O.J. Glembocki, M. Tomkiewicz and J.M. Woodall. Valuable assistance in the preparation of this article has been rendered by H. Qiang, X. Yin, Y. Yin, D. Yan and E. Wisloh.

References

- 1 F.H. Pollak, *Proc. Soc. Photo-Optical Instrum. Eng.*, 276 (1981) 142.
- 2 M. Cardona, *Modulation Spectroscopy*, Academic Press, New York, 1969, and references therein.
- 3 M. Cardona, *Festkörperprobleme X*, Pergamon, Oxford, 1970, p. 125.
- 4 Y. Hamakawa and T. Nishino, in B.O. Seraphin (ed.), *Optical Properties of Solids: New Developments*, North-Holland, Amsterdam, 1976, p. 255.
- 5 D.E. Aspnes, in M. Balkanski (ed.), *Handbook on Semiconductors*, Vol. 2, North-Holland, New York, 1980, p. 109; also *Surf. Sci.*, 37 (1973) 418.
- 6 E.E. Mendez, L.L. Chang, G. Landgren, R. Ludeke, L. Esaki and F.H. Pollak, *Phys. Rev. Lett.*, 46 (1981) 1230.
- 7 M. Erman, J.B. Teehan, P. Frijlink, S. Gaillard, F.J. Hia and C. Alibert, *J. Appl. Phys.*, 56 (1984) 3241.
- 8 C. Alibert, S. Gaillard, J.A. Brum, G. Bastard, P. Frijlink and M. Erman, *Solid State Commun.*, 53 (1985) 457.
- 9 O.J. Glembocki, B.V. Shanabrook, N. Bottka, W.T. Beard and J. Comas, *Proc. Soc. Photo-Optical Instrum. Eng.*, 524 (1985) 86.
- 10 O.J. Glembocki, B.V. Shanabrook, N. Bottka, W.T. Beard and J. Comas, *Appl. Phys. Lett.*, 46 (1985) 970.
- 11 F.H. Pollak, in M. Balkanski (ed.), *Handbook on Semiconductors*, North-Holland, New York, 1993 (in press).
- 12 O.J. Glembocki, *Mat. Res. Soc. Symp. Proc.*, 160 (1990) 631; *Proc. Soc. Photo-Optical Instrum. Eng.*, 1286 (1990) 2.
- 13 F.H. Pollak and O.J. Glembocki, *Proc. Soc. Photo-Optical Instrum. Eng.*, 946 (1988) 2.
- 14 O.J. Glembocki and B.V. Shanabrook, in D.G. Seiler and C.L. Littler (eds.), *Semiconductors and Semimetals*, Vol. 67, Academic Press, New York, 1992, p. 222.
- 15 F.H. Pollak, in C. Evans, R. Brundle and S. Wilson (eds.), *Encyclopedia of Materials Characterization: Surfaces, Interfaces and Thin Films*, Butterworth-Heinemann, Boston, 1992, p. 385; F.H. Pollak and H. Shen, *J. Electron. Mater.*, 19 (1990) 399.
- 16 X. Yin and F.H. Pollak, *Appl. Phys. Lett.*, 59 (1991) 2305.
- 17 X. Yin, X. Guo, F.H. Pollak, G.D. Pettit, J.M. Woodall, T.P. Chin and C.W. Tu, *Appl. Phys. Lett.*, 60 (1992) 1336.
- 18 X. Yin, X. Guo, F.H. Pollak, G.D. Pettit, J.M. Woodall and E-H. Cirlin, *Proc. Soc. Photo-Optical Instrum. Eng.*, 1678 (1992) 168.

- 19 S.L. Mioc, P.M. Raccah and J.W. Garland, *Proc. Soc. Photo-Optical Instrum. Eng.*, **1678** (1992) 296.
- 20 M.H. Herman, *Proc. Soc. Photo-Optical Instrum. Eng.*, **1286** (1990) 39.
- 21 H. Shen, P. Parayanthal, Y.F. Liu and F.H. Pollak, *Rev. Sci. Instrum.*, **58** (1987) 1429.
- 22 H. Shen, F.H. Pollak, J.M. Woodall and R.N. Sacks, *J. Electron. Mater.*, **19** (1990) 283.
- 23 M. Sydor, A. Badakhshan, J.R. Engholm and D.A. Dale, *Appl. Phys. Lett.*, **58** (1991) 948.
- 24 H. Shen, X.C. Shen, F.H. Pollak and R.N. Sacks, *Phys. Rev. B* **35** (1987) 3487.
- 25 E. Ehrenfreund, J. Oiknine-Schlesinger, D. Gershoni, D. Ritter, M.B. Panish and R.A. Hamm, *Surf. Sci.*, **267** (1992) 461.
- 26 Y. Garini, E. Cohen, E. Ehrenfreund, A. Ron, K.K. Law, J.L. Merz and A.C. Gossard, *Surf. Sci.*, **263** (1992) 561.
- 27 W.M. Theis, G.D. Sanders, C.E. Leak, K.K. Bajaj and H. Morkoç, *Phys. Rev. B* **37** (1988) 3042.
- 28 O.J. Glembotck and B.V. Shanabrook, *Proc. Soc. Photo-Optical Instrum. Eng.*, **794** (1987) 74.
- 29 H. Shen and M. Dutta, *Appl. Phys. Lett.*, **57** (1990) 587.
- 30 R.L. Tober, W.Q. Li and P.K. Bhattacharya, *J. Appl. Phys.*, submitted.
- 31 R.E. Hummel, W. Xi, P.H. Holloway and K.A. Jones, *J. Appl. Phys.*, **63** (1988) 2591.
- 32 R.E. Hummel, *Proc. Soc. Photo-Optical Instrum. Eng.*, **1286** (1990) 146.
- 33 R.E. Hummel, W. Xi and D.R. Hagmann, *J. Electrochem. Soc.*, **137** (1990) 3583.
- 34 C. Shwe and M. Gal, *Appl. Phys. Lett.*, **57** (1990) 1910.
- 35 C. Shwe, M. Gal and M. Gross, *J. Vac. Sci. Technol. A* **9** (1991) 2683; C. Shwe and M. Gal, *Australian J. Phys.*, **44** (1991) 705.
- 36 M. Gal, C. Shwe, J. Tann, P. McMillan, M. Gross and R. Shi, *Proc. Soc. Photo-Optical Instrum. Eng.*, **1286** (1990) 136.
- 37 M. Gal, C. Shwe and P. Kraisingdecha, *Proc. Soc. Photo-Optical Instrum. Eng.*, **1678** (1992) 276.
- 38 S.E. Acosta-Ortiz and A. Lastras-Martinez, *Solid State Commun.*, **64** (1987) 809.
- 39 S.E. Acosta-Ortiz and A. Lastras-Martinez, *Phys. Rev. B* **40** (1989) 1426.
- 40 S.E. Acosta-Ortiz and A. Lastras-Martinez, *Proc. Soc. Photo-Optical Instrum. Eng.*, **1286** (1990) 31.
- 41 D.E. Aspnes, R. Bhat, E. Colas, L.T. Florez, J.P. Harbison, M.K. Kelley, V.G. Karamidas, M.A. Koza and A.A. Studna, *Proc. Soc. Photo-Optical Instrum. Eng.*, **1037** (1988) 2.
- 42 D.E. Aspnes, J.P. Harbison, A.A. Studna and L.T. Florez, *J. Vac. Sci. Technol. A* **6** (1988) 1327.
- 43 D.E. Aspnes, *Proc. Soc. Photo-Optical Instrum. Eng.*, **1361** (1991) 551.
- 44 D. Drevillon, *Proc. Soc. Photo-Optical Instrum. Eng.*, **1186** (1989) 110.
- 45 D. Drevillon, *Proc. Soc. Photo-Optical Instrum. Eng.*, **1361** (1991) 551.
- 46 P.M. Raccah, J.W. Garland, Z. Zhang, U. Lee, D.Z. Xue, L.L. Abels, S. Ugur and W. Walinsky, *Phys. Rev. Lett.*, **53** (1984) 1958.
- 47 P.M. Raccah, U. Lee, S. Ugur, D.Z. Xue, L.L. Abels and J.W. Garland, *J. Vac. Sci. Technol. A* **3** (1985) 138.
- 48 J.W. Garland and P.M. Raccah, *Proc. Soc. Photo-Optical Instrum. Eng.*, **659** (1986) 32.
- 49 D.S. Kyser and V. Rehn, *Solid State Commun.*, **8** (1970) 1437.
- 50 J.W. Garland, H. Abad, M. Viccaro and P.M. Raccah, *Appl. Phys. Lett.*, **52** (1988) 1176.
- 51 A. Hamnett, J. Gilman and R.A. Batchelor, *Electrochim. Acta*, **37** (1992) 949.
- 52 D.E. Aspnes and A.A. Studna, *Phys. Rev. B* **7** (1973) 4605.
- 53 D.E. Aspnes, *Phys. Rev. B* **10** (1974) 4228.
- 54 H. Shen and F.H. Pollak, *Phys. Rev. B* **42** (1990) 7097.
- 55 R. Bhattacharya, H. Shen, P. Parayanthal, F.H. Pollak, T. Coutts and H. Aharoni, *Solar Cells*, **21** (1987) 371.
- 56 R. Bhattacharya, H. Shen, P. Parayanthal, F.H. Pollak, T. Coutts and H. Aharoni, *Proc. Soc. Photo-Optical Instrum. Eng.*, **794** (1987) 81.
- 57 R. Bhattacharya, H. Shen, P. Parayanthal, F.H. Pollak, T. Coutts and H. Aharoni, *Phys. Rev. B* **37** (1988) 4044.
- 58 R. Glosser and N. Bottka, *Proc. Soc. Photo-Optical Instrum. Eng.*, **794** (1987) 88.
- 59 N. Bottka, D.K. Gaskell, R.S. Sillmon, R. Henry and R. Glosser, *J. Electron. Mater.*, **17** (1988) 161.
- 60 R.A. Batchelor and A. Hamnett, *Proc. Soc. Photo-Optical Instrum. Eng.*, **1286** (1990) 175.
- 61 P.L. Jackson and E.G. Seebauer, *J. Appl. Phys.*, **69** (1991) 943.
- 62 U. Behn and H. Roppischer, *J. Phys. C: Solid State Phys.*, **21** (1988) 5507.
- 63 J.M.A. Gilman, A. Hamnett and R.A. Batchelor, *Phys. Rev. B* **46** (1992) 13363; R.A. Batchelor and A. Hamnett, *J. Appl. Phys.*, **71** (1992) 1376.
- 64 R.L. Tober, G.W. Bryant, W.Q. Li, J. Pamulapati and P.K. Bhattacharya, *Proc. Soc. Photo-Optical Instrum. Eng.*, **1675** (1992) 67.
- 65 C. Van Hoof, K. Denef, J. DeBoeck, D.J. Arent and G. Borghs, *Appl. Phys. Lett.*, **54** (1989) 608.
- 66 X. Yin, H.-M. Chen, F.H. Pollak, Y. Chan, P.A. Montano, P.D. Kirchner, G.D. Pettit and J.M. Woodall, *Appl. Phys. Lett.*, **58** (1991) 260.
- 67 X. Yin, H.-M. Chen, Z. Hang, F.H. Pollak, A.C. Warren, P.D. Kirchner, G.D. Pettit and J.M. Woodall, in E.M. Anastassakis and J. D. Joannopoulos (eds.), *Proc. 20th Int. Conf. Phys. Semicond.*, Thessaloniki, World Scientific, Singapore, 1990, p. 277.

- 68 X. Yin, H.-M. Chen, F.H. Pollak, Y. Cao, P.A. Montano, P.D. Kirchner, G.D. Pettit and J.M. Woodall, *J. Vac. Sci. Technol.*, **A10** (1992) 131.
- 69 H. Shen, M. Dutta, L. Fotiadis, P.G. Newman, R.P. Moerkirk, W.H. Chang and R.N. Sacks, *Appl. Phys. Lett.*, **57** (1990) 2118.
- 70 B.V. Shanabrook and O.J. Glembocki, in O. Engstrom (ed.), *Proc. 18th Int. Conf. Phys. Semicond.*, Stockholm, World Scientific, Singapore, 1987 p. 565.
- 71 B.V. Shanabrook, O.J. Glembocki and W.T. Beard, *J. Phys. Rev.*, **B35** (1987) 2540.
- 72 R. Enderlein, *Proc. Soc. Photo-Optical Instrum. Eng.*, **1286** (1990) 188; R. Enderlein, D.-S. Jiang and Y.S. Tang, *Phys. Stat. Solidi*, **145(b)** (1988) 167.
- 73 O.J. Glembocki and B.V. Shanabrook, *Superlattices and Microstructures*, **5** (1989) 603.
- 74 D.-S. Jiang, Y.S. Tang, J.-B. Xia and R. Enderlein, *Superlattices and Microstructures*, **6** (1989) 387.
- 75 Y.S. Tang, *J. Appl. Phys.*, **69** (1991) 8298.
- 76 Y.S. Huang, H. Qiang, F.H. Pollak, J. Lee and B. Elman, *J. Appl. Phys.*, **70** (1991) 3808.
- 77 X.L. Zheng, D. Heiman, B. Lax, F.A. Chambers and K.A. Stair, *Appl. Phys. Lett.*, **52** (1988) 984.
- 78 O.J. Glembocki and B.V. Shanabrook, *Superlattices and Microstructures*, **3** (1987) 235.
- 79 J. Camassel, D. Auvergne, H. Mathieu and B. Pistoulet, *Phys. Stat. Sol.*, **42** (1970) 147.
- 80 Y. Yin, D. Yan, F.H. Pollak, G.D. Pettit and J.M. Woodall, *Phys. Rev.*, **B43** (1991) 12138.
- 81 R.L. Tober, J. Pamulapati, J.E. Oh and P.K. Bhattacharya, *Appl. Phys. Lett.*, **53** (1988) 883.
- 82 R.L. Tober, J. Pamulapati, J.E. Oh and P.K. Bhattacharya, *J. Electron. Mater.*, **18** (1989) 379.
- 83 D.L. Smith and C. Mailhiot, *Rev. Mod. Phys.*, **62** (1990) 173.
- 84 M. Gal and C. Shwe, *Appl. Phys. Lett.*, **56** (1990) 545.
- 85 P.C. Klipstein and N. Apsley, *J. Phys. C: Solid State Phys.*, **19** (1986) 6461.
- 86 P.C. Klipstein, P.R. Tapster, N. Apsley, D.A. Anderson, M.S. Skolnick, T.M. Kerr and K. Woodbridge, *J. Phys. C: Solid State Phys.*, **19** (1986) 857.
- 87 A.P. Thorn, A.J. Shields, P.C. Klipstein, N. Apsley and T.M. Kerr, *J. Phys. C: Solid State Phys.*, **20** (1987) 4229.
- 88 X.L. Zheng, D. Heiman, B. Lax and F.A. Chambers, *Appl. Phys. Lett.*, **52** (1988) 287; *Proc. Soc. Photo-Optical Eng.*, **946** (1988) 43.
- 89 D. Huang, M. Mui and M. Morkoç, *J. Appl. Phys.*, **66** (1989) 358.
- 90 A.J. Shields, P.C. Klipstein and N. Apsley, *Semicond. Sci. Technol.*, **4** (1989) 476.
- 91 A.J. Shields and P.C. Klipstein, *Phys. Rev.*, **B43** (1991) 9118.
- 92 Y.S. Tang, *Phys. Stat. Solidi*, **129(a)** (1992) 285.
- 93 R.A. Batchelor and A. Hamnett, *J. Appl. Phys.*, **71** (1992) 2414.
- 94 D. Huang, G. Ji, U.K. Reddy, H. Morkoç, F. Xiong and T.A. Tombrello, *J. Appl. Phys.*, **63** (1988) 5447.
- 95 M. Kallergi, B. Roughani, J. Aubel and S. Sundaram, *J. Appl. Phys.*, **68** (1990) 4656.
- 96 M. Nakayama, I. Tanaka, T. Doguchi and H. Nishimura, *Jpn. J. Appl. Phys.*, **29** (1990) L1760.
- 97 A. Frova and P. Handler, *Phys. Rev.*, **137** (1965) A1857.
- 98 P. Handler, *Phys. Rev.*, **137** (1965) A1862.
- 99 D.E. Aspnes, *Phys. Rev.*, **B12** (1975) 2297.
- 100 Z.Q. Shi and W.A. Anderson, *J. Appl. Phys.*, **70** (1991) 3137.
- 101 R.A. Batchelor, A.C. Brown and A. Hamnett, *Phys. Rev.*, **B41** (1990) 1401.
- 102 R.P. Silberstein and F.H. Pollak, *Solid State Commun.*, **33** (1980) 1131.
- 103 L.P. Bicelli, *J. Appl. Phys.*, **62** (1987) 4523.
- 104 A. Berry, D.K. Gaskill and N. Bottka, *Proc. Soc. Photo-Optical Instrum. Eng.*, **1286** (1990) 85.
- 105 R. Goldhahn and H. Roppischer, *Phys. Stat. Solidi*, **154(b)** (1989) 769.
- 106 H. Poras, G.J. Goldsmith and N. Pan, *J. Appl. Phys.*, **22** (1992) 5484.
- 107 M. Zass, R. Sizmann and F. Koch, in E.M. Anastassakis and J.D. Joannopoulos (eds.), *Proc. 20th Int. Conf. Phys. Semicond.*, Thessaloniki, World Scientific, Singapore, 1990, p. 1186.
- 108 M. Sydor, J. Angelo, W. Mitchel, T.W. Haas and M.-Y. Yen, *J. Appl. Phys.*, **66** (1989) 1989.
- 109 N. Bottka, D.K. Gaskill, R.J.M. Griffiths, R.R. Bradley, T.B. Joyce, C. Ito and D. McIntyre, *J. Cryst. Growth*, **93** (1988) 481.
- 110 M. Sydor, J. Angelo, J.J. Wilson, J.C. Mitchel and M.Y. Yen, *Phys. Rev.*, **B40** (1989) 8473.
- 111 M. Sydor, N. Jahren, W.C. Mitchel, W.V. Lampert, T.W. Haas, M.Y. Yen, S.M. Mudare and D.H. Tomich, *J. Appl. Phys.*, **62** (1990) 7423.
- 112 T. Dittrich, *Phys. Stat. Solidi*, **119(a)** (1990) 479.
- 113 M. Kallergi, B. Roughani, J. Aubel and S. Sundaram, T. Chu, S. Chu and R. Green, *J. Vac. Sci. Technol.*, **A8** (1990) 1907.
- 114 A. Badakhshan, R. Glosser and S. Lambert, *J. Appl. Phys.*, **69** (1991) 2575; *Proc. Soc. Photo-Optical Instrum. Eng.*, **1286** (1990) 382.
- 115 A. Badakhshan, R. Glosser, S. Lambert, M. Anthony, R.S. Sillmon, P.E. Thompson and K. Alavi, *Appl. Phys. Lett.*, **59** (1991) 1218.

- 116 A. Badakhshan, C. Durbin, R. Glosser, K. Alavi, S. Nicholas, D. Dale and K. Capuder, *Proc. Soc. Photo-Optical Instrum. Eng.*, 1678 (1992) 194; A. Badakhshan, C. Durbin, R. Glosser, K. Alavi, R.S. Sillmon, P.E. Thompson and K. Capuder, *Inst. Phys. Conf. Ser.*, 120 (1992) 635.
- 117 L. Peters, L. Phaneuf, L.W. Kapitan and W.M. Theis, *J. Appl. Phys.*, 62 (1987) 4558.
- 118 H. Tanaka, E. Colas, I. Kamiya, D.E. Aspnes and R. Bhat, *Appl. Phys. Lett.*, 59 (1991) 3443.
- 119 H.H. Farrell, M.C. Tamargo, T.J. Gmitter, A.L. Weaver and D.E. Aspnes, *J. Appl. Phys.*, 70 (1991) 1033.
- 120 O.J. Glembocki, N. Bottka and J.E. Furneaux, *J. Appl. Phys.*, 57 (1985) 432.
- 121 R.L. Tober and J.D. Bruno, *J. Appl. Phys.*, 68 (1990) 6388.
- 122 H. Shen, Z. Hang, S.H. Pan, F.H. Pollak and J.M. Woodall, *Appl. Phys. Lett.*, 52 (1988) 2058.
- 123 A.N. Pikhtin, V.-M. Airaksinen, H. Lipsanen and T. Tuomi, *J. Appl. Phys.*, 65 (1989) 2556.
- 124 S.K. Brierley and D.S. Lehr, *J. Appl. Phys.*, 67 (1990) 3878.
- 125 X. Yin, F.H. Pollak, L. Pawlowicz, T.J. O'Neill and M. Hafizi, *Appl. Phys. Lett.*, 56 (1990) 1278; *Proc. Soc. Photo-Optical Instrum. Eng.*, 1286 (1990) 404.
- 126 M.H. Herman, P.J. Pearah, K. Elcess and I.D. Ward, *Proc. Mat. Res. Soc.*, 163 (1990) 197.
- 127 U. Behn and H. Roppischer, *Phys. Stat. Solidi*, 141(b) (1987) 325.
- 128 P.M. Raccah, J.W. Garland, Z. Zhang, A.H.M. Chu, J. Reno, I.K. Sou, M. Boukerche and J.P. Faurie, *J. Vac. Sci. Technol.*, A4 (1986) 2077.
- 129 P.M. Raccah, J.W. Garland, Z. Zhang, S. Mioc, Y. De, A.H.M. Chu, S. McGirgan and R.N. Thomas, *Proc. Soc. Photo-Optical Instrum. Eng.*, 623 (1986) 40.
- 130 Y.R. Lee, A.K. Ramdas and R.L. Aggarwal, *Phys. Rev.*, B38 (1988) 10600.
- 131 P.M. Amirtharaj, J.H. Dinan, J.J. Kennedy, J.R. Boyd and O.J. Glembocki, *J. Vac. Sci. Technol.*, A4 (1986) 2028.
- 132 A. Ksendzov, F.H. Pollak, P.M. Amirtharaj and J.A. Wilson, *J. Cryst. Growth*, 86 (1988) 586.
- 133 H. Shen, S.H. Pan, Z. Hang, J. Leng, F.H. Pollak, J.M. Woodall and R.N. Sacks, *Appl. Phys. Lett.*, 53 (1988) 1080.
- 134 H. Shen, F.H. Pollak, J.M. Woodall and R.N. Sacks, *J. Vac. Sci. Technol.*, B7 (1989) 804.
- 135 T. Kanata, M. Matsunaga, H. Takakawa, Y. Hamakawa and T. Nishino, *J. Appl. Phys.*, 69 (1991) 3691.
- 136 C. Durbin, J.P. Estrera, R. Glosser, W. Duncan, R.L. Henry, P. Nordquist, N. Bottka and D.K. Gaskill, *Appl. Phys. Lett.*, 61 (1992) 1549.
- 137 J.S. Kline, F.H. Pollak and M. Cardona, *Helv. Phys. Acta*, 41 (1968) 968.
- 138 O. Berolo and J.C. Woolley, *Can. J. Phys.*, 49 (1971) 1335.
- 139 J.L. Aubel, U.K. Reddy, S. Sundaram, W.T. Beard and J. Comas, *J. Appl. Phys.*, 58 (1985) 495.
- 140 C. Alibert, A.M. Joullie and C. Ance, *Phys. Rev.*, B27 (1983) 4946.
- 141 S. Tachi, A. Moritani and J. Nakai, *J. Electrochem. Soc.*, 124 (1977) 1948.
- 142 D.P. Bour, J.R. Shealy, A. Ksendzov and F.H. Pollak, *J. Appl. Phys.*, 64 (1988) 6456.
- 143 C. Alibert, G. Bordure, A. Langier and J. Chevallier, *Phys. Rev.*, B6 (1972) 1301.
- 144 P. Merle, D. Auvergne, H. Mathieu and J. Chevallier, *Phys. Rev.*, B15 (1977) 2032.
- 145 A. Irzikevicius, J. Kavalaiskas and A.Yu. Shileika, *Phys. Stat. Solidi*, 49(b) (1972) K87.
- 146 E.W. Williams and V. Rehn, *Phys. Rev.*, 172 (1968) 798.
- 147 S.S. Vishnabhatla, B. Eyglunent and J.C. Woolley, *Can. J. Phys.*, 47 (1969) 1661.
- 148 J.M. Wrobel, J.L. Aubel, U.K. Reddy, S. Sundaram, J.P. Salerno and J.W. Gormley, *J. Appl. Phys.*, 59 (1986) 266.
- 149 S. Ravipati, P.W. Yu, B.E. Taylor and W.C. Mitchel, *Proc. Soc. Photo-Optical Instrum. Eng.*, 1286 (1990) 66.
- 150 D. Auvergne, J. Camassel, H. Mathieu and A. Joullie, *J. Phys. Chem. Solids*, 35 (1974) 133.
- 151 A. Moritani, K. Taniguchi, J. Hamaguchi and J. Nakai, *J. Phys. Soc. Jpn.*, 34 (1973) 79.
- 152 P.M. Raccah and U. Lee, *J. Vac. Sci. Technol.*, A1 (1983) 1587.
- 153 C. Nguyen Van Huong, C. Hinnen, R. Triboulet and P. Lemasson, *J. Cryst. Growth*, 72 (1985) 419.
- 154 P.M. Amirtharaj, F.H. Pollak and J.K. Furdyna, *Solid State Commun.*, 39 (1981) 35.
- 155 J.M. Wrobel, L.C. Barrett, J.L. Aubel, S. Sundaram and P. Becha, *J. Appl. Phys.*, 60 (1986) 1135.
- 156 J. Stankiewicz, N. Bottka and W. Giriat, *J. Phys. Soc. Jpn., Suppl.* A49 (1980) 827.
- 157 N. Bottka, J. Stankiewicz and W. Giriat, *J. Appl. Phys.*, 52 (1981) 4189.
- 158 J. Stankiewicz and J.R. Fermin, *J. Appl. Phys.*, 63 (1988) 3300.
- 159 Y. Yin, F.H. Pollak, P. Auvray, D. Dutartre, R. Pantel and J.A. Chroboczek, *Thin Solid Films*, 222 (1992) 85.
- 160 P.M. Laufer, F.H. Pollak, R.E. Nahory and M.A. Pollack, *Solid State Commun.*, 36 (1980) 419.
- 161 J.A. Lahtinen and T. Tuomi, *Phys. Stat. Solidi*, 130(b) (1985) 637.
- 162 J.R. Flemish, H. Shen, K.A. Jones, M. Dutta and V.S. Ban, *J. Appl. Phys.*, 70 (1991) 2152.
- 163 P. Parayanthal, C.S. Ro, F.H. Pollak, C.R. Stanley, G.W. Wicks and L.F. Eastman, *Appl. Phys. Lett.*, 43 (1983) 109.
- 164 J.A. Lott, L.R. Dawson, E.D. Jones, I.J. Fritz, J.S. Nelson and S.R. Kurtz, *J. Electron. Mater.*, 19 (1990) 989.
- 165 K. Asami, H. Asahi, S.-I. Gonda, Y. Kamamura and H. Tanaka, *Solid State Commun.*, 70 (1989) 33.
- 166 Y.P. Varshni, *Physica (Utrecht)*, 34 (1967) 149.

- 167 P. Lautenschlager, M. Garriga and M. Cardona, *Phys. Rev.*, **B35** (1987) 9174; P. Lautenschlager, M. Garriga and M. Cardona, *Phys. Rev.*, **B36** (1987) 4813.
- 168 P.B. Allen and M. Cardona, *Phys. Rev.*, **27** (1983) 4760.
- 169 C.K. Kim, C.P. Lautenschlager and M. Cardona, *Solid State Commun.*, **59** (1986) 797.
- 170 S. Gopalan, P. Lautenschlager and M. Cardona, *Phys. Rev.*, **B35** (1987) 2163.
- 171 S. Zollner, S. Gopalan and M. Cardona, *Solid State Commun.*, **77** (1991) 485.
- 172 K.P. O'Donnell and X. Chen, *Appl. Phys. Lett.*, **58** (1991) 2924.
- 173 F.H. Pollak and H. Shen, *J. Crystal Growth*, **98** (1989) 53.
- 174 H. Shen, Z. Hang, F.H. Pollak, K. Capuder and P.E. Norris, *Proc. Soc. Photo-Optical Instrum. Eng.*, **1186** (1989) 27.
- 175 K. Capuder, P.E. Norris, H. Shen, Z. Hang and F.H. Pollak, *J. Electron. Mater.*, **19** (1990) 295.
- 176 Z. Hang, F.H. Pollak and H. Shen, *Proc. Soc. Photo-Optical Instrum. Eng.*, **1285** (1990) 14.
- 177 H. Shen, *Proc. Soc. Photo-Optical Instrum. Eng.*, **1286** (1990) 125.
- 178 F.H. Pollak, *Proc. Soc. Photo-Optical Instrum. Eng.*, **1361** (1991) 109.
- 179 Z. Hang, H. Shen and F.H. Pollak, *Solid State Commun.*, **73** (1990) 15.
- 180 Z. Hang, F.H. Pollak, G.D. Pettit and J.M. Woodall, *Phys. Rev.*, **B44** (1991) 10546.
- 181 P.A. Dafesh and K.L. Wang, *Phys. Rev.*, **B45** (1992) 1712.
- 182 A. Manoogian and J.C. Woolley, *Can. J. Phys.*, **62** (1984) 285.
- 183 D.K. Gaskell, N. Bottka, L. Aina and M. Mattingly, *Appl. Phys. Lett.*, **56** (1990) 1269.
- 184 J.S. Hwang, S.L. Tyan, M.J. Lin and Y.K. Su, *Solid State Commun.*, **80** (1991) 891.
- 185 A. Ksendzov, F.H. Pollak and O.K. Wu, *Solid State Commun.*, **70** (1989) 963.
- 186 P. Koppel, *J. Appl. Phys.*, **57** (1985) 1705.
- 187 L.E.A. Berlouis, L.M. Peter, M.G. Astles and R.G. Humphreys, *Appl. Phys. Lett.*, **51** (1987) 502.
- 188 A. Ksendzov, F.H. Pollak, J.A. Wilson and V.A. Cotton, *J. Appl. Phys.*, **66** (1989) 5528.
- 189 Y.R. Lee, A.K. Ramdas, L.A. Kolodzesjki and R.L. Gunshor, *Phys. Rev.*, **B38** (1988) 13143.
- 190 T.M. Hsu and J.H. Lin, *Phys. Rev.*, **B37** (1988) 4106.
- 191 T.M. Hsu, *J. Appl. Phys.*, **69** (1991) 3772.
- 192 H. Qiang, F.H. Pollak, C.M. Sotomayor Torres, W. Leitch, A.H. Kean, M.A. Stroscio, G.J. Iafrate and K.W. Kim, *Appl. Phys. Lett.*, **61** (1992) 1411.
- 193 F.H. Pollak, in J.-P. LeBurton, J. Pasqual and C. Sotomayor Torres (eds.), *Phonons in Semiconductor Nanostructures*, Kluwer, Dordrecht, 1993, p. 341.
- 194 F.H. Pollak, in T.P. Pearsall (ed.), *Semiconductors and Semimetals*, Vol. 32, Academic Press, New York, 1990, p. 17.
- 195 H. Qiang, F.H. Pollak and G. Hickman, *Solid State Commun.*, **76** (1990) 1087.
- 196 H. Qiang, F.H. Pollak and R.N. Sacks, *Solid State Commun.*, **84** (1992) 51.
- 197 H. Qiang, F.H. Pollak, K. Shum, Y. Takiguchi, R.R. Alfano, S.F. Fang and H. Morkoç, *Appl. Phys. Lett.*, **60** (1992) 2651.
- 198 F.H. Pollak and H. Qiang, *Jpn. J. Appl. Phys.*, **32** (suppl. 32-1) (1990) 101.
- 199 V.-S. Pahk, S. Chongsawangvirod and E.A. Irene, *J. Electrochem. Soc.*, **138** (1991) 308.
- 200 S. Chongsawangvirod and E.A. Irene, *J. Electrochem. Soc.*, **138** (1991) 1748.
- 201 T.M. Burns, S. Chongsawangvirod, J.W. Andrews, E.A. Irene, G. McGuire and S. Chevacharoekul, *J. Vac. Sci. Technol.*, **B9** (1991) 41.
- 202 T.M. Burns, E.A. Irene, S. Chevacharoekul and G. McGuire, *J. Vac. Sci. Technol.*, **B11** (1993) 78.
- 203 W.-M. Shen, M.C.A. Fantini, F.H. Pollak, M. Tomkiewicz, J.J. Leary and J.P. Gambino, *J. Appl. Phys.*, **66** (1989) 1765.
- 204 F.H. Pollak, R. Tsu and E.E. Mendez, in C.W. White and P.S. Peercy (eds.), *Laser and Electron Beam Processing of Materials*, Academic Press, New York, 1980, p. 195.
- 205 V.I. Gavrilenko, A.M. Evstigneev, V.A. Zuev, V.G. Litovchenko, O.V. Snitko and V.A. Tyagai, *Sov. Phys. Semicond.*, **10** (1976) 640.
- 206 L.A. Alimazov, V.I. Gavrilenko, V.A. Zuev and V.G. Litovchenko, *Sov. Phys. Semicond.*, **12** (1978) 913.
- 207 J.T. Fitch, C.H. Bjorkman, G. Lucovsky, F.H. Pollak and X. Yin, *J. Vac. Sci. Technol.*, **B7** (1989) 775.
- 208 X. Yin, F.H. Pollak, J.T. Fitch, C.H. Bjorkman and G. Lucovsky, *Proc. Soc. Photo-Optical Instrum. Eng.*, **1186** (1989) 122.
- 209 P. Yongwattansoontorn, H. Kubo, M. Morifushi, K. Taniguchi, C. Hamaguchi and K. Imai, 1991, in *Proc. 1991 International Conference on Solid State Devices and Materials*, Yokohama, p. 35.
- 210 R.C. Bowman, Jr., D.N. Jamieson, P.M. Adams and R.L. Alt, *Proc. Soc. Photo-Optical Instrum. Eng.*, **946** (1988) 65; R.C. Bowman, Jr., P.M. Adams, J.F. Knudsen, S.C. Mass, P.A. Dafesh, D.D. Smith, M.H. Herman and I.D. Ward, *Mat. Res. Soc. Symp.*, **147** (1989) 303.
- 211 M.V. Rao, R.S. Babu, A.K. Berry, H.B. Deitrich and N. Bottka, *J. Electron. Mater.*, **19** (1990) 789.
- 212 L. He and W. Anderson, *J. Electron. Mater.*, **20** (1991) 359.
- 213 W.M. Duncan and A.F. Schreiner, *Solid State Commun.*, **31** (1979) 457.

- 214 V.I. Gavrilenko and V.A. Zuev, *Sov. Phys. Semicond.*, **12** (1978) 570.
- 215 L. He and W. Anderson, *Solid State Electron.*, **35** (1992) 151.
- 216 P.A.F. Herbert, M. Murtagh, P.V. Kelly, G.M. Crean and W.M. Kelly, *Microelectron. Eng.*, in press.
- 217 M. Murtagh, P.V. Kelly, P.A.F. Herbert, M. O'Connor, G. Duffy and G.M. Crean, *Appl. Surf. Sci.*, **63** (1993) 158; M. Murtagh, S. Lynch, P.V. Kelly, P.A.F. Herbert and G.M. Crean, in *Proc. Irish Materials Forum*, in press.
- 218 L. He and W. Anderson, *J. Electron. Mater.*, **21** (1992) 39.
- 219 C. Shwe and M. Gal, *Appl. Phys. Lett.*, in press.
- 220 H. Roppischer, R. Goldhahn, J.A. Bumai and D.S. Domanevskii, *Phys. Stat. Solidi*, **103(a)** (1987) 161.
- 221 X. Yin, H.-M. Chen, F.H. Pollak, Y. Chan, P.A. Montano, P.D. Kirchner, G.D. Pettit and J.M. Woodall, *J. Vac. Sci. Technol.*, **B9** (1991) 2114.
- 222 X. Yin, X. Guo, F.H. Pollak, G.D. Pettit, D.T. McInturff, J.M. Woodall and E.-H. Cirlin, *Appl. Surf. Sci.*, **63** (1993) 163.
- 223 O.J. Glembotck, J.A. Dagata, E.S. Snow and D.S. Katzer, *Appl. Surf. Sci.*, **63** (1993) 143.
- 224 L. He and W. Anderson, *J. Electron. Mater.*, **21** (1992) 937.
- 225 Z.Q. Shi and W.A. Anderson, *Solid State Electron.*, **35** (1992) 1427.
- 226 D.K. Gaskill, N. Bottka and A.K. Berry, in A.G. Milnes and C.J. Miner (eds.), *Proc. 6th Int. Conf. on Semi-Insulating III-V Materials*, Toronto, Adam Hilger, Bristol, 1990, p. 329.
- 227 A.K. Berry, D.K. Gaskill, G.T. Stauf and N. Bottka, *Appl. Phys. Lett.*, **58** (1991) 2824.
- 228 P.M. Amirtharaj, R.C. Bowman, Jr and R.L. Alt, *Proc. Soc. Photo-Optical Instrum. Eng.*, **946** (1988) 57.
- 229 A. Lastras-Martinez, U. Lee, J. Zehnder and P.M. Raccah, *J. Vac. Sci. Technol.*, **21** (1982) 157.
- 230 P.M. Raccah, U. Lee, J.A. Silberman, W.E. Spicer and J.A. Wilson, *Appl. Phys. Lett.*, **42** (1983) 374.
- 231 P.M. Raccah, U. Lee, S. Ugur, D.Z. Xue, L.L. Abels and J.W. Garland, *J. Vac. Sci. Technol.*, **A3** (1985) 138.
- 232 P.M. Raccah, J.W. Garland, Z. Zhang, D. Yang, L.O. Bubuloc and W.E. Tenant, *J. Vac. Sci. Technol.*, **A5** (1987) 3180.
- 233 S.-C. Chao, K.-T. Hsu, G.-J. Jan, F.-Y. Juang, T.-F. Chang and J.-S. Wu, *Jpn. J. Appl. Phys.*, **31** (1992) 1436.
- 234 P.M. Raccah, J.W. Garland, S.E. Buttrill, Jr, L. Francke and J. Jackson, *Appl. Phys. Lett.*, **52** (1988) 1584.
- 235 P.M. Raccah, J.W. Garland, Z. Zhang, U. Lee, S. Ugur, S. Mioc, S. K. Ghandi and R. Bhatt, *J. Appl. Phys.*, **57** (1985) 2014.
- 236 P.M. Raccah, Z. Zhang, J.W. Garland, A.H.M. Chu, M.J. Bevan, J. Thompson and K.J. Woodhouse, *J. Vac. Sci. Technol.*, **A4** (1986) 2226.
- 237 T.M. Hsu, J.S. Lee and H.L. Hwang, *J. Appl. Phys.*, **68** (1990) 283.
- 238 T.M. Hsu, *J. Appl. Phys.*, **59** (1986) 2538.
- 239 Y. Hamakawa, in J.I. Pankove (ed.), *Semiconductors and Semimetals*, Vol. 21B, Academic Press, New York, 1984, p. 141.
- 240 V.I. Gavrilenko, J. Humlcek, N.I. Klyui and V.G. Litovchenko, *Phys. Stat. Solidi*, **155(b)** (1989) 723.
- 241 V.I. Gavrilenko, J. Humlcek, N.I. Klyui, V.G. Litovchenko and V.E. Strelntskii, *Phys. Stat. Solidi*, **145(b)** (1988) 209.
- 242 V.I. Gavrilenko, V.A. Zuev and V.G. Litovchenko, *Sov. Phys. Solid State*, **19** (1977) 333.
- 243 R. Bhattacharya, C.Y. Lee, F.H. Pollak and D.M. Schleich, *J. Non-Crystalline Solids*, **91** (1987) 235.
- 244 M. Hecht, *Phys. Rev.*, **B41** (1990) 7918.
- 245 M. Hecht, *J. Vac. Sci. Technol.*, **B8** (1990) 1018.
- 246 K. Jacobi, U. Myler and P. Althainz, *Phys. Rev.*, **B41** (1990) 10721.
- 247 S. Chang, I.M. Vitomirov, L.J. Brillson, Y.J. Kime, D.S. Rioux, P.D. Kirchner, G.D. Pettit, J.M. Woodall and M. Hecht, *Phys. Rev.*, **B41** (1990) 12299.
- 248 V. Airaksinen and H.K. Lipsanen, *Appl. Phys. Lett.*, **60** (1992) 2110.
- 249 H. Shen, J. Pamulapati, R. Lux, M. Dutta, F.C. Rong, M. Taysing-Lara, L. Fotiadis, L. Calderon and Y. Lu, *Proc. Soc. Photo-Optical Instrum. Eng.*, **1678** (1992) 211.
- 250 H. Shen, F.C. Rong, R. Lux, J. Pamulapati, M. Dutta, M. Taysing-Lara, E.H. Poindexter, L. Calderon and Y. Lu, *Appl. Phys. Lett.*, **61** (1992) 1585.
- 251 A.C. Warren, J.M. Woodall, P.D. Kirchner, X. Yin, F. Pollak, M.R. Melloch, N. Otsuka and K. Mahalingam, *Phys. Rev.*, **B46** (1992) 4617.
- 252 A.C. Warren, J.M. Woodall, P.D. Kirchner, X. Yin, X. Guo, F. Pollak and M.R. Melloch, *J. Vac. Sci. Technol.*, **B10** (1992) 1904.
- 253 A.C. Warren, J.M. Woodall, J.H. Burroughes, P.D. Kirchner, H.K. Heinrich, G. Arjavalingam, N. Katzenellenbogen, D. Grischkowsky, M.R. Melloch, N. Otsuka, K. Mahalingam, F.H. Pollak and X. Yin, *Mat. Rec. Soc. Symp. Proc.*, **241** (1992) 15.
- 254 H. Shen, M. Dutta, W. Chang, R. Moerkirk, D.M. Kim, K.W. Chung, P.P. Ruden, M.I. Nathan and M.A. Stroscio, *Appl. Phys. Lett.*, **60** (1992) 2400.
- 255 H. Shen, M. Dutta, J. Pamulapati, W. Chang, M.A. Stroscio and X. Zhang, *Proc. Soc. Photo-Optical Instrum. Eng.*, **1678** (1992) 203.
- 256 H. Shen, M. Dutta, R. Lux, W. Buchwald, L. Fotiadis and R.N. Sacks, *Appl. Phys. Lett.*, **59** (1991) 321.

- 257 D.K. Gaskill, N. Bottka and R.S. Sillmon, *J. Vac. Sci. Technol.*, **B6** (1988) 1497.
- 258 H. Shen, F.H. Pollak and J.M. Woodall, *J. Vac. Sci. Technol.*, **B8** (1990) 413.
- 259 V.L. Berkovits, V.N. Bessolov, T.N. L'vova, E.B. Novikov, V.I. Safarov, R.V. Khasieva and B.V. Tsarenkov, *J. Appl. Phys.*, **70** (1991) 3707.
- 260 S. Hildebrandt, J. Schreiber, W. Kircher and R. Kuzmenko, *Appl. Surf. Sci.*, **63** (1993) 153.
- 261 E.G. Seebauer, *J. Appl. Phys.*, **66** (1989) 4963.
- 262 T. Kanata, M. Matsunaga, H. Takakura, Y. Hamakawa and T. Nishino, *Proc. Soc. Photo-Optical Instrum. Eng.*, **1286** (1990) 56.
- 263 J.S. Hwang and Z. Hang, in *Proc. Fourth Int. Conf. Indium Phosphide and Related Materials*, Newport, RI, IEEE, New York, 1992, p.518.
- 264 P.M. Raccah, J.W. Garland, Z. Zhang, L.L. Abels, S. Ugur, S. Mioc and M. Brown, *Phys. Rev. Lett.*, **55** (1985) 1323.
- 265 L. Kassel, H. Abad, J.W. Garland, P.M. Raccah, J.E. Potts, M.A. Haase and H. Cheng, *Appl. Phys. Lett.*, **56** (1990) 42.
- 266 L. Kassel, T.W. Garland, P.M. Raccah, M.C. Tamargo and H.H. Farrell, *Semicond. Sci. Technol.*, **6** (1991) A152.
- 267 L. Kassel, J.W. Garland, P.M. Raccah, M.A. Haase and H. Cheng, *Semicond. Sci. Technol.*, **6** (1991) A146.
- 268 C.R. Lu, J.R. Anderson, D.R. Stone, W.T. Beard, R.A. Wilson, T.F. Kuech and S.L. Wright, *Phys. Rev. B43* (1991) 11791.
- 269 R. Goldhahn, H. Roppischer, M. Gericke and C.-E. Richter, *Phys. Stat. Solidi*, **119(a)** (1990) 183.
- 270 D.S. Mui, A. Salvador, S. Strite and H. Morkoç, *Appl. Phys. Lett.*, **57** (1990) 572.
- 271 M. Capizzi, C. Coluzza, P. Frankl, A. Frova, X. Yin, F.H. Pollak and R.N. Sacks, *Proc. Soc. Photo-Optical Instrum. Eng.*, **1286** (1990) 50.
- 272 D. Yang, J.W. Garland, P.M. Raccah, C. Coluzza, P. Frankl, M. Cappizzi, F. Chambers and G. Devane, *Appl. Phys. Lett.*, **57** (1990) 2829.
- 273 D. Yang, J.W. Garland, P.M. Raccah, C. Coluzza, P. Frankl, M. Cappizzi, F. Chambers and G. Devane, *Physica*, **B170** (1991) 557.
- 274 R.P. Silberstein, J.K. Lyden, M. Tomkiewicz and F.H. Pollak, *J. Vac. Sci. Technol.*, **19** (1981) 406.
- 275 F.H. Pollak, in W.L. Wallace, A.J. Nozik, S.K. Deb and R.H. Wilson (eds.), *Photochemistry: Fundamental Processes and Measurement Techniques*, Electrochemical Society, Pennington NJ, 1982, p. 608.
- 276 M. Tomkiewicz, W. Siripala and R. Tenne, *J. Electrochem. Soc.*, **131** (1984) 736.
- 277 G.A. Scholz and H. Gerischer, *J. Electrochem. Soc.*, **132** (1985) 1643.
- 278 P. Lemasson, *J. Crystal Growth*, **72** (1985) 405; P. Lemasson and C. Nguyen Van Huong, *J. Electrochem. Soc.*, **135** (1988) 2080.
- 279 C. Levy-Clement, D. Sedaries, W.-M. Shen and M. Tomkiewicz, in D.S. Ginley, A. Nozik, N. Armstrong, K. Honda, A. Fujishima and T. Sokata (eds.), *Proc. Symp. Photoelectrochemistry Materials*, Electrochemical Society, Pennington NJ, 1988, p. 250.
- 280 P. Salvador, M. Pujadas and G. Campet, *Phys. Rev. B38* (1988) 9881.
- 281 M. Tomkiewicz and W.-M. Shen, in D.S. Ginley, A. Nozik, N. Armstrong, K. Honda, A. Fujishima and T. Sokata (eds.), *Proc. Symp. Photoelectrochemistry and Electrosynthesis on Semiconducting Materials*, Electrochemical Society, Pennington NJ, 1988, p. 250.
- 282 A.E. Willner, O.J. Glembocki, D.V. Podlesnik, E.D. Palik and R.M. Osgood, Jr, *Proc. Soc. Photo-Optical Instrum. Eng.*, **946** (1988) 48.
- 283 M.C.A. Fantini, W.M. Shen, M. Tomkiewicz and J.P. Gambino, *J. Appl. Phys.*, **65** (1989) 4884.
- 284 W.-M. Shen, M.C.A. Fantini, M. Tomkiewicz and J.P. Gambino, *J. Appl. Phys.*, **66** (1989) 1759.
- 285 W.-M. Shen, M. Tomkiewicz, D. Sedaries and C. Levy-Clement, *J. Electrochem. Soc.*, **137** (1990) 2656.
- 286 R.A. Batchelor, A. Hamnett, R. Peat and L.M. Peter, *J. Appl. Phys.*, **70** (1991) 266.
- 287 M. Kallergi, J. Aubel and S. Sundaram, *J. Appl. Phys.*, **66** (1989) 4862.
- 288 T. Kanata, H. Suzawa, M. Matsunaga, T. Takakura, Y. Hamakawa, H. Kato, T. Nishino, *Phys. Rev. B41* (1990) 2936.
- 289 M. Dutta, H. Shen, S.M. Vernon and T.M. Dixon, *Appl. Phys. Lett.*, **57** (1990) 1775.
- 290 A. Dimoulas, P. Tzanetakis, A. Georgakias, O.J. Glembocki and A. Christou, *J. Appl. Phys.*, **67** (1990) 4389.
- 291 J.P. Estrera, W.M. Duncan, Y.C. Kao, H.Y. Liu, P.D. Stevens and E.A. Beam III, *Proc. Soc. Photo-Optical Instrum. Eng.*, **1678** (1992) 120.
- 292 G. Weiser, R. Weihofin and G.G. Baumann, *Proc. Soc. Photo-Optical Instrum. Eng.*, **1286** (1990) 329.
- 293 M.-E. Pistol, M. Gerling, A. Gustafsson, G. Paulsson, L. Samuelson and H. Titze, *Mat. Res. Symp. Proc.*, **160** (1990) 673.
- 294 S. Minagawa and M. Kondow, *Proc. Soc. Photo-Optical Instrum. Eng.*, **1286** (1990) 74.
- 295 Y.R. Lee, R.G. Alonso, E.-K. Suh, A.K. Ramdas, L.-X. Li and J.K. Furdyna, *J. Appl. Phys.*, **68** (1990) 1023.
- 296 H. Mathieu, J. Allegre and B. Gil, *Phys. Rev. B43* (1991) 2218.

- 297 A. Giordana, R. Glosser, J.G. Pellegrino, S. Qadri and E.D. Richmond, *Mater. Lett.*, **8** (1989) 64; A. Giordana, R. Glosser, J.G. Pellegrino, S. Qadri, M.E. Twigg, E.D. Richmond, K. Joyner and G. Pollack, *Proc. Mat. Res. Soc.*, **188** (1990) 349.
- 298 A. Giordana and R. Glosser, *J. Appl. Phys.*, **69** (1991) 3303.
- 299 T. Nishino, Y. Inoue, Y. Hamakawa, M. Kondow and S. Minagawa, *Appl. Phys. Lett.*, **53** (1988) 583.
- 300 Y. Inoue, T. Nishino, Y. Hamakawa, M. Kondow and S. Minagawa, *Optoelectron.—Devices and Technol.*, **3** (1988) 61.
- 301 M. Kondow, H. Kakibayashi, S. Minagawa, Y. Inoue, T. Nishino and Y. Hamakawa, *Appl. Phys. Lett.*, **53** (1988) 2053.
- 302 T. Nishino, *J. Crystal Growth*, **98** (1989) 44.
- 303 D.C. Look, J.E. Hoelscher, J.T. Grant, C.E. Stutz, K.R. Evans and M. Numan, *Mat. Res. Soc. Symp. Proc.*, **241** (1991) 87.
- 304 J. Allegre, J. Calayud, B. Gil, H. Mathieu, H. Tuffigo, G. Lentz, N. Magnea and H. Mariette, *Phys. Rev.*, **B41** (1990) 8195.
- 305 H. Shen and F.H. Pollak, in S. Mahajan and L.C. Kimmerling (eds.), *Concise Encyclopedia of Semiconducting Materials and Related Technologies*, Pergamon Press, Oxford, 1992, p.386.
- 306 F.H. Pollak and H. Shen, in S. Mahajan and L.C. Kimmerling (eds.), *Concise Encyclopedia of Semiconducting Materials and Related Technologies*, Pergamon Press, Oxford, 1992 p. 388.
- 307 Z.M. Fang, A. Persson and R.M. Cohen, *Phys. Rev.*, **B37** (1988) 4071.
- 308 H. Shen, P. Parayanthal, F.H. Pollak, M. Tomkiewicz, T.J. Drummond and J.N. Schulman, *Appl. Phys. Lett.*, **48** (1986) 653.
- 309 Y.S. Huang, H. Qiang, F.H. Pollak, G.D. Pettit, P.K. Kirchner, J.M. Woodall, H. Stragier and L.B. Sorenson, *J. Appl. Phys.*, **70** (1992) 7537.
- 310 H. Qiang, Y.S. Huang, F.H. Pollak, G.D. Pettit and J.M. Woodall, *Proc. Soc. Photo-Optical Instrum. Eng.*, **1678** (1992) 177.
- 311 H. Shen, S.H. Pan, F.H. Pollak and R.N. Sacks, *Phys. Rev.*, **B37** (1988) 10919; *Proc. Soc. Photo-Optical Instrum. Eng.*, **946** (1988) 36.
- 312 H. Shen, S.H. Pan, F.H. Pollak, M. Dutta and T. AuCoin, *Phys. Rev.*, **B36** (1987) 9384.
- 313 F. Cerdeira, C. Vazquez-Lopez, E. Ribeiro, P.A.M. Rodrigues, V. Lemos, M.A. Sacilotti and A.P. Roth, *Phys. Rev.*, **B42** (1990) 9480.
- 314 S. Niki, A.L. Kellner, S.C. Lin, A. Chen, A.R. Williams, W.S.C. Chang and H.H. Wieder, *Appl. Phys. Lett.*, **56** (1990) 475.
- 315 C. Coriasso, D. Campi, C. Cacciatore, C. Alibert, S. Gaillard, B. Lambert and A. Regreny, *Europhys. Lett.*, **16** (1991) 591; D. Campi, C. Cacciatore, C. Coriasso, C. Alibert and A. Regreny, in H. Schlotterer (ed.), *Proc. Symp. A: Materials for Optoelectronic Devices, OEICs and Photonics*, European Materials Research Society Fall Meeting, 1990, Strasbourg, North-Holland, Amsterdam, 1991, p. 289.
- 316 H. Xu, X. Zhou, G. Xu, Q. Du, E. Wang, L. Zhang and C. Chen, *Appl. Phys. Lett.*, **61** (1992) 2193.
- 317 Y.S. Tang, *Phys. Stat. Solidi*, **154(b)** (1989) K187.
- 318 W.M. Theis, G.D. Sanders, K.R. Evans, L.L. Liou, C.E. Leak, K.K. Bajaj, C.E. Stutz, R.I. Jones and Y.-C. Chang, *Phys. Rev.*, **B39** (1989) 11038.
- 319 E.L. Ivchenko, V.P. Kochereshko, I.N. Ural'tsev and D.R. Yakovlev, *Phys. Stat. Solidi*, **161(b)** (1990) 217.
- 320 G. Jan, K. Hsu, P. Tseng, C. Lin and I.-F. Chang, *Proc. Soc. Photo-Optical Instrum. Eng.*, **1286** (1990) 200.
- 321 A. Ksendzov, H. Shen, F.H. Pollak and D.P. Bour, *Solid State Commun.*, **73** (1990) 11; *Surf. Sci.*, **228** (1990) 326; *Proc. Soc. Photo-Optical Eng.*, **1283** (1990) 241.
- 322 G. Armelles, M.I. Alonso, P. Castrillo and P.S. Dominguez, *Appl. Phys. Lett.*, **60** (1992) 3277.
- 323 P. Parayanthal, H. Shen, F.H. Pollak, O.J. Glembocki, B.V. Shanabrook and W.T. Beard, *Appl. Phys. Lett.*, **48** (1986) 1261.
- 324 F.H. Pollak and H. Shen, *Superlattices and Microstructures*, **6** (1989) 203.
- 325 A.K. Ramdas, *Superlattices and Microstructures*, **4** (1988) 69.
- 326 F.H. Pollak, *Superlattices and Microstructures*, **10** (1991) 333.
- 327 R.L. Tober, A.L. Smirl, T.F. Boggess and J.M. Schulman, *J. Appl. Phys.*, **64** (1988) 4678.
- 328 D. Elbert, E. Ehrenfreund, J. Bajaj, G.J. Sullivan and C. Lind, *J. Appl. Phys.*, in press.
- 329 B.V. Shanabrook, O.J. Glembocki, D.A. Broido, L. Vina and W.I. Wang, *J. de Physique*, **48** (1987) C5-235.
- 330 Y. El Khalifi, P. Lefebvre, J. Allegre, B. Gil and H. Mathieu, *Solid State Commun.*, **75** (1990) 677.
- 331 P. Castrillo, G. Armelles, M.I. Alonso, P.S. Dominguez and F. Briones, in *Proc. 21st Int. Conf. Physics Semicond.*, Beijing, 1992, in press.
- 332 Y.R. Lee, A.K. Ramdas, A.L. Moretti, F.A. Chambers, G.P. Devane and L.P. Ram-Mohan, *Phys. Rev.*, **B41** (1990) 8380.
- 333 R.F. Kopf, M.H. Herman, M.L. Schnoes, A.P. Perley, G. Livescu and M. Ohring, *J. Appl. Phys.*, **71** (1992) 5004.
- 334 H. Shen, S.H. Pan, Z. Hang, F.H. Pollak and R.N. Sacks, *Solid State Commun.*, **65** (1988) 929.

- 335 W.M. Theis, G.D. Sanders, C.E. Leak, D.C. Reynolds, Y.-C. Chang, K. Alavi, C. Colvard and I. Shidlovsky, *Phys. Rev.*, **B39** (1989) 1442.
- 336 E. Finkman, M.D. Sturge, M.H. Meynadier, R.E. Nahory, M.C. Tomargo, D.M. Hwang and C.C. Chang, *J. Luminescence*, **39** (1987) 57.
- 337 T. Nakazawa, H. Fujimoto, K. Imanishi, K. Taniguchi, C. Hamaguchi, S. Hiyamizu and S. Sasa, *J. Phys. Soc. Jpn.*, **58** (1989) 2192.
- 338 H. Fujimoto, C. Hamaguchi, T. Nakazawa, K. Taniguchi, K. Imanishi, H. Kato and Y. Watanabe, *Phys. Rev.*, **B41** (1990) 7593; *Surf. Sci.*, **228** (1990) 206.
- 339 C. Hamaguchi, T. Nakazawa, T. Matsuoka, H. Kato and Y. Watanabe, *Proc. Soc. Photo-Optical Instrum. Eng.*, **1286** (1990) 280.
- 340 T. Matsuoka, T. Nakazawa, T. Ohya, K. Taniguchi, C. Hamaguchi, H. Kato and Y. Watanabe, *Phys. Rev.*, **B43** (1991) 11798.
- 341 D. Dossa, L.C.L.Y. Voon, L.R. Ram-Mohan, C. Parks, R.G. Alonso, A.K. Ramdas, M.R. Melloch, *Appl. Phys. Lett.*, **59** (1991) 2706.
- 342 C. Parks, R.G. Alonso, A.K. Ramdas, L.R. Ram-Mohan, D. Dossa and M.R. Melloch, *Phys. Rev.*, **B45** (1992) 14215.
- 343 S. Fafard, E. Fortin and A.P. Roth, *Phys. Rev.*, **B45** (1992) 13769.
- 344 S. Fafard, *Phys. Rev.*, **B46** (1991) 4659.
- 345 A. Tai, G. Goldsmith and T. Moustakas, personal communication (1993).
- 346 H. Shen, F.H. Pollak and R. Tsu, *Appl. Phys. Rev.*, **57** (1990) 13.
- 347 U.K. Reddy, G. Ji, R. Houdre, H. Unlu, D. Huang and H. Morkoç, *Proc. Soc. Photo-Optical Instrum. Eng.*, **794** (1987) 116.
- 348 G. Ji, U.K. Reddy, D. Huang, T.S. Henderson and H. Morkoç, *Superlattices and Microstructures*, **3** (1987) 539.
- 349 S.H. Pan, H. Shen, Z. Hang, F.H. Pollak, W. Zhuang, Q. Xu, A.P. Roth, R.A. Masut, C. Lacelle and D. Morris, *Phys. Rev.*, **B38** (1988) 3375.
- 350 G. Ji, W. Dobbelaere, D. Huang and H. Morkoç, *Phys. Rev.*, **B39** (1989) 3216.
- 351 D.J. Arent, K. Denefne, C. Van Hoof, J. DeBoeck and G. Borghs, *J. Appl. Phys.*, **66** (1989) 1739.
- 352 Y.S. Tang, *Semicond. Sci. Technol.*, **4** (1989) 871.
- 353 U.K. Reddy, G. Ji, T. Henderson, R. Houdre, H. Morkoç and C.W. Litton, *J. Vac. Sci. Technol.*, **B7** (1989) 1106.
- 354 O. Brandt, L. Tapfer, R. Cingolani, K. Ploog, M. Hohenstein and F. Phillip, *Phys. Rev.*, **B41** (1990) 12599.
- 355 R. Cingolani, O. Brandt, L. Tapfer, G. Scamarcio, G.C. LaRocca and K. Ploog, *Phys. Rev.*, **B42** (1990) 3209.
- 356 S.C. Shen, W. Shan, X.M. Fang, Z. Hang and F.H. Pollak, *Proc. Soc. Photo-Optical Instrum. Eng.*, **1286** (1990) 221.
- 357 A. Ksendzov, T. George, F.J. Grunthaner, J.K. Liu, D.H. Rich, R.W. Terhune, B.A. Wilson, F.H. Pollak and Y.-S. Huang, *Proc. Mat. Res. Soc.*, **221** (1991) 459.
- 358 C. Vazquez-Lopez, E. Ribiera, F. Cerdeira, P. Motisuke, M.A. Sociolotti and A.P. Roth, *J. Appl. Phys.*, **69** (1991) 7836.
- 359 O. Brandt, R. Cingolani, L. Tapfer, G. Scamarcio and K. Ploog, *Superlattices and Microstructures*, **9** (1991) 147.
- 360 M. Nakayama, T. Doguchi and H. Nishimura, *J. Appl. Phys.*, **72** (1992) 2372.
- 361 M.H. Herman, A. Dodabalapur, I.D. Ward and B.G. Streetman, *Proc. Mat. Res. Soc.*, **160** (1990) 655.
- 362 A. Dodabalapur, V.P. Kesan, D.P. Neikirk, B.G. Streetman, M.H. Herman and I.D. Ward, *J. Electron. Mater.*, **19** (1990) 265.
- 363 M.J. Joyce, M.J. Johnson, M. Gal and B.F. Usher, *Phys. Rev.*, **B38** (1988) 10978.
- 364 B. Jogai, *Appl. Phys. Lett.*, **59** (1991) 1329.
- 365 P. Castrillo, G. Armelles, A. Ruiz and F. Briones, *Jpn. J. Appl. Phys.*, **30** (1992) PL1784.
- 366 I.J. Fritz, T.M. Brennan and D.S. Ginley, *Solid State Commun.*, **75** (1990) 289.
- 367 B. Gil, L.K. Howard, D.J. Dunstan, P. Boring and P. Lefebvre, *Phys. Rev.*, **B45** (1992) 3906.
- 368 J.M. Rodriguez, G. Armelles, J.P. Silveira, M. Vasquez and F. Briones, *Phys. Rev.*, **B40** (1989) 8570.
- 369 C. Raisin, L. Lassabatere, C. Alibert, B. Girault, G. Abdel-Fattah and V. Voisin, *Solid State Commun.*, **61** (1987) 17.
- 370 H. Shen, Z. Hang, L. Leng, F.H. Pollak, L.L. Chang, W.I. Wang and L. Esaki, *Superlattices and Microstructures*, **5** (1989) 591.
- 371 V. Airaksinen, H.K. Lipsanen, P. Ravila, T. Tuomi and P.A. Claxton, *Proc. Soc. Photo-Optical Instrum. Eng.*, **1286** (1990) 238.
- 372 H.K. Lipsanen, V. Airaksinen, T. Tuomi and P.A. Claxton, *Proc. Soc. Photo-Optical Instrum. Eng.*, **1286** (1990) 300.
- 373 X. Yin, F.H. Pollak, B.T. McDermott, K.G. Reid and S.M. Bedair, *Mat. Res. Soc. Symp. Proc.*, **160** (1990) 679.
- 374 M. Razeghi, D. Yang, J.W. Garland, Z. Zhang and D. Xue, *Proc. SPIE*, **1676** (1992) 130.
- 375 M.I. Alonso, M.C. Munoz, G. Armelles, A. Ruiz, A. Mazuelas, P. Castrillo and F. Briones, in *Proc. 21st Int. Conf. Physics Semicond.*, Beijing, 1992, in press.
- 376 K. Satzke, G. Weiser, R. Hoger and W. Thulke, *J. Appl. Phys.*, **63** (1988) 5485.

- 377 S.J. Hwang, W. Shan, J.J. Song, H.Q. Hou and C.W. Tu, *J. Appl. Phys.*, **72** (1992) 1645.
- 378 K. Satzke, W. Stoltz and G. Weiser, *Proc. Soc. Photo-Opt. Instrum. Eng.*, **1286** (1990) 265.
- 379 J.F. Klem, D. Huang, H. Morkoç, Y.E. Ihm and N. Otsuka, *Proc. Soc. Photo-Optical Instrum. Eng.*, **877** (1988) 28.
- 380 T.P. Pearsall, J. Bevk, L.C. Feldman, J.M. Bonar, J.P. Mannaerts and A. Ourmazd, *Phys. Rev. Lett.*, **58** (1987) 729.
- 381 T.P. Pearsall, J. Bevk, J.C. Bean, J. Bonar, J.P. Mannaerts and A. Ourmazd, *Phys. Rev.*, **B39** (1989) 3741.
- 382 K. Asami, K. Miki, K. Sakamoto, T. Sakamoto and S.-I. Gonda, *Jpn. J. Appl. Phys.*, **29** (1990) L381.
- 383 T.P. Pearsall, J.M. Vandenberg, R. Hull and J.M. Bonar, *Phys. Rev. Lett.*, **63** (1989) 2104.
- 384 M.A. Gell, M.H. Herman, K. Elcess, I.D. Ward, C.J. Gibbings and C.G. Tuppen, *Proc. Soc. Photo-Optical Instrum. Eng.*, **1286** (1990) 320.
- 385 Y. Yin, D. Yan, F.H. Pollak, M.S. Hybersten, J.M. Vandenberg and J.C. Bean, *Phys. Rev.*, **B44** (1991) 5955.
- 386 V. Menczigar, M. Dahman, R. Zachai, K. Eberl and G. Abstreiter, *Proc. Soc. Photo-Optical Instrum. Eng.*, **1361** (1991) 282.
- 387 Y. Yin, D. Yan, F.H. Pollak, M.S. Hybersten, J.M. Vandenberg and J.C. Bean, *Surf. Sci.*, **267** (1992) 99.
- 388 P.A. Dafesh, V. Arbet and K.L. Wang, *Appl. Phys. Lett.*, **56** (1990) 1498.
- 389 P.A. Dafesh, V. Arbet and K.L. Wang, *Proc. Soc. Photo-Optical Instrum. Eng.*, **1286** (1990) 308.
- 390 T.P. Pearsall, F.H. Pollak, J.C. Bean and R. Hull, *Phys. Rev.*, **B33** (1986) 6821.
- 391 T.P. Pearsall, *CRC Critical Reviews in Solid State and Materials Science*, **15** (1989) 551.
- 392 T.P. Pearsall, *Proc. Soc. Photo-Optical Instrum. Eng.*, **1286** (1990) 256.
- 393 M. Gal, J.S. Yuan, J.M. Viner, P.C. Taylor and G.B. Stringfellow, *Phys. Rev.*, **B33** (1986) 4410.
- 394 X.C. Shen, H. Shen, P. Parayanthal, F.H. Pollak, J.N. Schulman, A.L. Smirl, R.A. McFarlane and I. D'Haenans, *Superlattices and Microstructures*, **2** (1986) 513.
- 395 Y. Tang, B. Wang, D.-S. Jiang, W. Zhuang and J. Liang, *Solid State Commun.*, **63** (1987) 793.
- 396 N. Linder, W. El-Banna, U.D. Keil, K. Schmidt, G.H. Dohler, J.N. Miller and K.J. Ebeling, *Proc. Soc. Photo-Optical Instrum. Eng.*, **1286** (1990) 359.
- 397 V.L. Alperovich, A.S. Jaroshevich, D.I. Lubyshev, V.P. Migal, V.V. Preobrazhenski and B.R. Semjagin, *Superlattices and Microstructures*, **10** (1991) 131.
- 398 V.L. Alperovich, A.S. Jaroshevich, D.I. Lubyshev and V.P. Migal, *Physica*, **B175** (1991) 153.
- 399 Y. Tang, D.-S. Jiang and K. Ploog, *Solid State Commun.*, **64** (1987) 655.
- 400 U.D. Keil, M. Forkel, N. Linder, K. Schmidt, G.H. Dohler and J.N. Miller, *Proc. Soc. Photo-Optical Instrum. Eng.*, **1286** (1990) 339.
- 401 Y. Yin, H. Qiang, F.H. Pollak, D.C. Streit and M. Wojtowicz, *Appl. Phys. Lett.*, **61** (1992) 1579; *Proc. Soc. Photo-Optical Instrum. Eng.*, **1675** (1992) 498.
- 402 Y. Yin, H. Qiang, D. Yan, F.H. Pollak and T.F. Noble, *Semicond. Sci. Technol.*, in press.
- 403 E.S. Snow, O.J. Glembocci and B.V. Shanabrook, *Phys. Rev.*, **B38** (1988) 12483.
- 404 Y.S. Tang, *J. Appl. Phys.*, **71** (1992) 2392.
- 405 Y. Tang and J. Desheng, *Chinese Phys. Lett.*, **4** (1987) 283.
- 406 Y.S. Tang, Y.W. Xu, D.-S. Jiang, W.H. Zhuang and M.Y. Kong, *Superlattices and Microstructures*, **6** (1989) 391.
- 407 A.A. Bernussi, C.A.C. Mendonca, P. Motisuki, E.A. Meneses, F. Cerdeira, F.H. Pollak, P. Basmaji and I.F.L. Dias, in E.M. Anastassakis and J.D. Joannopoulos (eds.), *Proc. 20th Int. Conf. Phys. Semicond.*, Thessaloniki, World Scientific, Singapore, 1990, p. 1065.
- 408 C.H. Mendonca, L.M. Scolfaro, E.A. Meneses, J.M. Martins and J.R. Leite, *Proc. Soc. Photo-Optical Instrum. Eng.*, **1286** (1990) 370.
- 409 N. Pan, X.L. Zheng, H. Hendriks and J. Carter, *J. Appl. Phys.*, **68** (1990) 2355.
- 410 J.M.V. Martins, L.M.R. Scolfaro, C.A.C. Mendonca, E.A. Meneses and J.R. Leite, *Superlattices and Microstructures*, **10** (1991) 239.
- 411 M. Sydor and A. Badakhshan, *J. Appl. Phys.*, **70** (1991) 2322.
- 412 R.A. Novellino, C. Vazquez-Lopez, A.A. Bernussi, C. Schmidt, F. Cerdeira, P. Motisuke, F.H. Pollak, F. Meseguer and K. Ploog, *J. Appl. Phys.*, **70** (1991) 5577.
- 413 B.L. Weiss, A.G. Choo and H.E. Jackson, *Proc. Soc. Photo-Optical Instrum. Eng.*, **1678** (1992) 189.
- 414 A.A. Bernussi, F. Iikawa, P. Motisuke, P. Basmaji, M. Siu Li and O. Hipolito, *J. Appl. Phys.*, **67** (1990) 4149.
- 415 A.A. Bernussi, F. Iikawa, P. Motisuke, P. Basmaji, M. Siu Li and O. Hipolito, *Proc. Soc. Photo-Optical Instrum. Eng.*, **1286** (1990) 348.
- 416 M. Sydor, A. Badakhshan and J.R. Engholm, *Appl. Phys. Lett.*, **59** (1991) 677.
- 417 W. Zhou, C.H. Perry, L. Ma, K.-S. Lee, J.M. Worlock, A. Zrenner, F. Koch and K. Ploog, *J. Appl. Phys.*, **69** (1991) 4075.
- 418 T.M. Hsu, Y.C. Tien, N.H. Lu, S.P. Tsai, D.G. Liu and C.P. Lee, *J. Appl. Phys.*, **72** (1992) 1065.
- 419 D.G. Liu, K.H. Chang, C.P. Lee, T.M. Hsu and Y.C. Tien, *J. Appl. Phys.*, **72** (1992) 1468.
- 420 A. Badakhshan, M. Sydor and W.C. Mitchel, *J. Vac. Sci. Technol.*, **A10** (1992) 1842.

- 421 A. Badakhshan, M. Sydor, K. Alavi, N. Teraguchi and H. Morkoç, *Proc. Soc. Photo-Optical Instrum. Eng.*, 1678 (1992) 159.
- 422 A. Badakhshan and M. Sydor, *Inst. Phys. Conf. Ser.*, 120 (1992) 231.
- 423 M. Sydor, J.R. Engholm, M.O. Manasreh, K.R. Evans, C.E. Stutz and W.C. Mitchel, *Phys. Rev.*, B45 (1992) 13796.
- 424 C. Cacciatore, D. Campi, C. Coriasso and C. Rigo, *Phys. Rev.*, B40 (1989) 6446.
- 425 D. Campi, C. Cacciatore, C. Coriasso, C. Villavecchia and C. Alibert, *Proc. Soc. Photo-Optical Instrum. Eng.*, 1280 (1990) 115.
- 426 O.J. Glembocki, E.S. Snow, R.W. Little and R.P. Leavitt, *Superlattices and Microstructures*, 10 (1991) 77.
- 427 P. Voisin, J. Bleuse, C. Bouche, S. Gaillard, C. Alibert and A. Regreny, *Phys. Rev. Lett.*, 61 (1988) 1639.
- 428 A.J. Shields, P.C. Klipstein, M.S. Skolnick, G.W. Smith and C.R. Whitehouse, *Phys. Rev.*, B42 (1990) 5879.
- 429 M. Nakayama, I. Tanaka, T. Doguchi, H. Nishimura, K. Kawashima and K. Fujiwara, *Solid State Commun.*, 77 (1991) 303.
- 430 M. Nakayama, I. Tanaka, H. Nishimura, K. Kawashima and K. Fujiwara, *Phys. Rev.*, B44 (1991) 5935.
- 431 A.J. Shields, P.C. Klipstein, J.S. Roberts and C. Button, *Phys. Rev.*, B42 (1990) 3599.
- 432 H. Qiang, F.H. Pollak, C. Mailhiot, G.D. Pettit and J.M. Woodall, *Phys. Rev.*, B44 (1991) 9126; *Surf. Sci.*, 267 (1992) 103.
- 433 K. Satzke, G. Weiser, W. Stoltz and K. Ploog, *Phys. Rev.*, B43 (1991) 2263.
- 434 A. Dimoulas, K.P. Giapis, J. Leng, G. Halkias, K. Zekentes and A. Christou, *J. Appl. Phys.*, 72 (1992) 1912.
- 435 G. Weiser, K. Satzke, B. Schlichtherle, L. Goldstein and A. Perales, *Phys. Rev.*, B45 (1992) 14376.
- 436 U. Behn, H.T. Grahn, H. Schneider and K. Ploog, *Proc. Soc. Photo-Optical Instrum. Eng.*, 1675 (1992) 298.
- 437 I. Tanaka, M. Nakayama, H. Nishimura, K. Kawashima and K. Fujiwara, *Phys. Rev.*, B46 (1992) 7656.
- 438 H. Schneider, A. Fischer and K. Ploog, *Proc. Soc. Photo-Optical Instrum. Eng.*, 1675 (1992) 433.
- 439 E. Riberio, F. Cerdeira and A.P. Roth, *Phys. Rev.*, B46 (1992) 12542.
- 440 A. Kangarlu, H.R. Chandrasekhar, M. Chandrasekhar, Y.M. Kapoor, F.A. Chambers, B.A. Vojak and J.M. Meese, *Phys. Rev.*, B37 (1988) 1035.
- 441 Y. Baltagi, S. Moneger, A. Tabata, T. Benyattou, C. Bru, A. Georgakilas, K. Zekentes and G. Halkias, *Appl. Surf. Sci.*, 63 (1993) 172.
- 442 O.J. Glembocki, B.V. Shanabrook and W.T. Beard, *Surf. Sci.*, 174 (1986) 206.
- 443 T. Nakazawa, T. Matsuaka, T. Ohya, K. Taniguchi, C. Hamaguchi, H. Kato and Y. Watanabe, *Proc. Soc. Photo-Optical Instrum. Eng.*, 1286 (1990) 244.
- 444 H.R. Chandrasekhar and M. Chandrasekhar, *Proc. Soc. Photo-Optical Instrum. Eng.*, 1286 (1990) 207.
- 445 A. Kangarlu, H.R. Chandrasekhar, M. Chandrasekhar, F.A. Chambers, B.A. Vojak and J.M. Meese, in O. Engstrom (ed.) *Proc. 18th Int. Conf. Phys. Semicond.*, Stockholm, World Scientific, Singapore, 1987, p. 569.
- 446 B. Rockwell, H.R. Chandrasekhar, M. Chandrasekhar, F.H. Pollak, H. Shen, L.L. Chang, W.I. Wang and L. Esaki, *Mat. Res. Soc. Symp. Proc.*, 160 (1990) 751; and in E.M. Anastassakis and J.D. Joannopoulos (eds.) *Proc. 20th Int. Conf. Physics Semicond.*, Thessaloniki, World Scientific, Singapore, 1990, p. 929.
- 447 B. Rockwell, H.R. Chandrasekhar, M. Chandrasekhar, A.K. Ramdas, M. Kobayashi and R.L. Gunshor, *Phys. Rev.*, B44 (1991) 11307.
- 448 N. Bottka, D.K. Gaskill, P.D. Wright, R.W. Kaliski and D.A. Williams, *J. Cryst. Growth*, 107 (1991) 893.
- 449 D. Yan, F.H. Pollak, V.T. Boccio, C.L. Lin, P.D. Kirchner, J.M. Woodall, R.C. Gee and P.M. Asbeck, *Appl. Phys. Lett.*, 61 (1992) 206.
- 450 A. Badakhshan, C. Durbin, A. Giordona, R. Glosser, S.A. Lambert and J. Liu, in M.A. Reed and W.P. Kirk (eds.), *Nanostructure Physics and Fabrication*, Academic Press, New York, 1989, p. 485.
- 451 R.A. Hopfel, J. Shah, A.C. Gossard and W. Wiegmann, *Appl. Phys. Lett.*, 47 (1985) 163.
- 452 I.J. Fritz, P.L. Gourley and T.J. Drummond, *App. Phys. Lett.*, 55 (1989) 1324.
- 453 P.A. Dafesh, *J. Appl. Phys.*, 71 (1992) 5154.
- 454 K. Misawa, A. Moritani and J. Nakai, *Jpn. J. Appl. Phys.*, 15 (1976) 1309.
- 455 A. Ksendzov, F.H. Pollak, J.A. Wilson and V.A. Cotton, *Appl. Phys. Lett.*, 49 (1986) 648.
- 456 P.M. Raccah, J.W. Garland, D. Yang, H. Abad, R.L. Strong and M.C. McNeill, *J. Vac. Sci. Technol.*, A7 (1989) 509.
- 457 K. Satzke, H.G. Vestner, G. Weiser, L. Goldstein and A. Perales, *J. Appl. Phys.*, 69 (1991) 7703.
- 458 G. Weiser, K. Satzke, H.G. Vestner, L. Goldstein and A. Perales, *Proc. Soc. Photo-Opt. Instrum. Eng.*, 1286 (1990) 393.
- 459 G. Mei, S. Carpenter, L. E. Felton and P.D. Persans, *J. Opt. Soc. Am.*, B9 (1992) 1394.
- 460 H. Qiang, F.H. Pollak, Y.-S. Tang, P.D. Wang and C.M. Sotomayor Torres, paper presented at the *Materials Research Society Symposium on Diagnostic Techniques for Semiconductor Materials Processing*, Boston, MA, November 1993 and to be published in the proceedings; also, submitted to *Appl. Phys. Lett.*

Appendix A: Acronyms

ASCDW	asymmetrically coupled double quantum well
BSR	back-surface reflection effect
BZ	Brillouin zone
CER	contactless electroreflectance
CT	confined transition
DLTS	deep level transient spectroscopy
DR	differential reflectivity
EBER	electron-beam electroreflectance
EER	electrolyte electroreflectance
EM	electromodulation
ER	electric-field modulated reflectance (electroreflectance)
FDLL	first-derivative of Lorentzian profiles lineshape
FDGL	first-derivative of Gaussian profiles lineshape
FKOs	Franz-Keldysh oscillations
GFF	generalized functional form of electromodulation
HBT	heterojunction bipolar transistor
HEMT	high electron mobility transistor
HH	heavy-hole valence band(subband)
HJ	heterojunction
LH	light-hole valence band(subband)
LPE	liquid phase epitaxy
LT-GaAs	low temperature MBE GaAs
MBE	molecular beam epitaxy
MDHJ	modulation-doped heterojunction
MIS	semiconductor-insulator-metal
MQW	multiple quantum wells
OMCVD	organo-metallic chemical vapor deposition
OMVPE	organo-metallic vapor phase epitaxy
PL	photoluminescence
PLE	photoluminescence excitation spectroscopy
PR	photoreflectance
PRE	photoreflectance excitation spectroscopy
PZR	piezoreflectance
QCSE	quantum confinement Stark effect
QW	quantum well
RA	reflectance anisotropy
RD	reflection difference (spectroscopy)
RDS	reflection difference spectroscopy
RIE	reactive-ion etching
RTA	rapid thermal annealing
SCC	space charge correction
SCR	space charge region
SCDW	symmetric coupled double quantum well
SL	superlattice
SQW	single quantum well

TDFF	third-derivative functional form of electromodulation
TEM	transmission electron microscopy
TIR	total internal reflection
TR	thermoreflectance
UN ⁺ (SIN ⁺)	undoped-N ⁺ structure
UP ⁺ (SIP ⁺)	undoped-P ⁺ structure
UHV	ultra high vacuum
UT	unconfined transition
VNDF	variable neutral density filter
WMR	wavelength modulated reflectivity
2D	two-dimensional
2DEG	two-dimensional electron gas

Symbols

A	amplitude
A_o	effective area which contributes to dark current mechanism
A_{pc}	effective area which contributes to photocurrent (illuminated area)
A^{**}	modified Richardson constant
a	hydrostatic deformation potential
a_B	strength of the electron-average phonon interaction
a_o	lattice constant
$a(\epsilon_1, \epsilon_2)$	Seraphin coefficient
$b(\epsilon_1, \epsilon_2)$	Seraphin coefficient
C_h	capacitance of the Helmholtz layer
D_s	density of surface states
E	photon energy
E_p	LO phonon energy
E_{ap}	average phonon energy
E_g	band gap
F	electric field
F_{dc}	dc field
F_{ac}	ac modulated field
f_e	Fermi function
$\hbar\theta$	electro-optic energy
$I_0(\lambda)$	incident light intensity
$I_0(T)$	saturation(dark) current
I_{pc}	photo-induced current
$J_0(T)$	saturation(dark) current density
J_{pc}	photo-induced current density
L_B	barrier width
L_z	well width
$L(E - E_g, T)$	line-shape factor
N	carrier concentration
N_s	two-dimensional electron gas density
N_{ss}	density of surface states

P	light intensity
P_{ac}	power density of the ac pump beam
P_b	power density of dc bias beam
P_{pr}	power density of the probe beam
q	electronic charge
Q_c	conduction band offset parameter
R	reflectivity
$R(\lambda)$	dc reflectance
\tilde{S}	uniaxial stress
S_{ac}	ac modulated stress
T	transmission
T_{ac}	ac modulated temperature
V_{ac}	applied ac modulating voltage
V_B	built-in potential barrier
V_F	Fermi level pinning position
V_p	photovoltage
α, β	Varshni coefficients
α_{th}	linear expansion coefficient
ΔE_c	conduction band offset
ΔE_v	valence band offset
ΔE_v^{HH}	heavy-hole valence band offset
$\Delta R(\lambda)$	change in reflectance
$\Delta\epsilon$	change in complex dielectric constant
$\Delta\epsilon_1$	change in real part of complex dielectric function
$\Delta\epsilon_2$	change in imaginary part of complex dielectric function
Γ	broadening parameter
Γ_{ep}	electron (exciton)-phonon coupling coefficient
γ	quantum efficiency
ϵ	complex dielectric function
ϵ_1	real part of complex dielectric function
ϵ_2	imaginary part of complex dielectric function
ϵ_0	permittivity of free space
η	ideality factor
θ_D	Debye temperature
κ	static dielectric constant
$K(E)$	complex propagation vector of light in the medium
λ	wavelength
ϕ	phase angle
$\mu_{ }$	reduced interband effective mass
Ω_m	modulation frequency

5. Surfaces and interfaces.....	312
5.1. Surfaces.....	312
5.2. Interfaces.....	317
6. Electrochemistry.....	319
7. Epitaxial layers.....	321
8. Semiconductor microstructures	323
8.1. Lineshape analysis and modulation mechanisms	325
8.2. Interference effects.....	328
8.3. Identification of heavy and light hole transitions.....	328
8.4. Topographical scans	329
8.5. Composition SQWs, MQWs and SLs	329
8.5.1. GaAs/Ga _{1-x} Al _x As system	329
8.5.2. In _x Ga _{1-x} As/Ga _{1-y} Al _y As system	334
8.5.3. GaSb/Ga _{1-x} Al _x Sb system.....	339
8.5.4. Other III-V systems	340
8.5.5. II-VI systems	340
8.5.6. GeSi/Si and GeSi/Ge systems	340
8.6. Doping superlattices	342
8.7. Two-dimensional electron gas (2DEG)	343
8.8. External perturbations	349
8.8.1. Electric fields	349
8.8.2. Temperature.....	353
8.8.2.1. Temperature dependence of intersubband transitions	353
8.8.2.2. Temperature dependence of the linewidth	354
8.8.3. Hydrostatic pressure	355
8.8.4. Uniaxial stress	355
8.8.5. Magnetic fields.....	356
9. Device structures	356
10. <i>In situ</i> monitoring of growth/processing	358
11. Summary and future trends	359
Note added in proof	361
Acknowledgements	361
References	361
Appendix A	372

Elsevier Science Publishers encourages the submission of articles and reviews in electronic form. A leaflet describing our very straightforward requirements, and the ways in which we can accept the output of most wordprocessing programs for subsequent direct entry into our typesetting system — thus saving time and avoiding rekeying errors — is available from the Publishers upon request.